Development of a two-photon excitation STED microscope and its application to neuroscience

Philipp Bethge

To cite this version:

Philipp Bethge. Development of a two-photon excitation STED microscope and its application to neuroscience. Neurons and Cognition [q-bio.NC]. Université de Bordeaux, 2014. English. <NNT : 2014BORD0018>. <tel-01138959>

HAL Id: tel-01138959
https://tel.archives-ouvertes.fr/tel-01138959

Submitted on 3 Apr 2015

THÈSE PRÉSENTÉE

POUR OBTENIR LE GRADE DE

DOCTEUR DE

L'UNIVERSITÉ DE BORDEAUX

ÉCOLE DOCTORALE

Sciences de la Vie et de la Santé

Philipp BETHGE

Développement d'un microscope STED à excitation deux photons et son application aux neurosciences

Sous la direction de : Prof. U. Valentin NÄGERL

Soutenue le 27.03.2014

Membres du jury :

MULLE, Christophe, Directeur de recherche (CE), CNRS UMR 5297 Bordeaux	Président
HOFER, Sonja, Professor, Universität Basel	Rapporteur
EMILIANI, Valentina, Directeur de recherche (DR2), CNRS UMR 8250 Paris	Rapporteur
MARSICANO, Giovanni, Directeur de recherche (DR2), INSERM U862 Bordeaux	invité

Développement d'un microscope STED à excitation deux photons et son application aux neurosciences

L’avènement de la microscopie STED (Stimulated Emission Depletion) a bouleversé le domaine des neurosciences du au fait que beaucoup de structures neuronale, tels que les épines dendritiques, les axones ou les processus astrocytaires, ne peuvent pas être correctement résolu en microscopie photonique classique.

La microscopie 2-photon est une technique d’imagerie photonique très largement utilisée dans le domaine des neurosciences car elle permet d’imager les événements dynamique en profondeur dans le tissu cérébral, offrant un excellent sectionnement optique et une meilleure profondeur de pénétration. Cependant, la résolution spatiale de cette approche est limitée autour de 0.5 µm, la rendant inappropriée pour étudier les détails morphologiques des neurones et synapses.

Le but de mon travail de thèse était à A) développer un microscope qui permet d'améliorer l'imagerie 2-photon en la combinant avec la microscopie STED et B) démontrer son potentiel pour l'imagerie à l'échelle nanométrique de processus neuronaux dynamiques dans des tranches de cerveau aigus et *in vivo*.

Le nouveau microscope permet d'obtenir une résolution spatiale latérale de ~ 50 nm à des profondeurs d'imagerie de ~ 50 µm dans du tissu cérébral vivant. Il fonctionne avec des fluorophores verts, y compris les protéines fluorescentes communes telles que la GFP et YFP, offrant le contraste de deux couleurs basé sur la détection spectrale et linéaire ‘unmixing’. S’agissant d’un microscope droit, utilisant un objectif à immersion ayant une grande distance de travail, nous avons pu incorporer des techniques électrophysiologiques comme patch-clamp et ajouter une plateforme pour l'imagerie *in vivo*.

J’ai utilise ce nouveau microscope pour imager des processus neuronaux fins et leur dynamique à l’échelle nanométrique dans différent types de préparations et des régions différentes du cerveau. J’ai pu révéler des nouvelles caractéristiques morphologique des dendrites et épines. En outre, j'ai exploré différentes stratégies de marquage pour pouvoir utiliser la microscopie STED pour imager le trafic des protéines et de leur dynamique à l'échelle nanométrique dans des tranches de cerveau.

Mots clés :

Microscope deux-photon, STED, GFP

Development of a two-photon excitation STED microscope and its application to neuroscience

The advent of STED microscopy has created a lot of excitement in the field of neuroscience because many important neuronal structures, such as dendritic spines, axonal shafts or astroglial processes, cannot be properly resolved by regular light microscopy techniques.

Two-photon fluorescence microscopy is a widely used imaging technique in neuroscience because it permits imaging dynamic events deep inside light-scattering brain tissue, providing high optical sectioning and depth penetration. However, the spatial resolution of this approach is limited to around half a micron, and hence is inadequate for revealing many morphological details of neurons and synapses.

The aim of my PhD work was to A) develop a microscope that improves on two-photon imaging by combining it with STED microscopy and to B) demonstrate its potential for nanoscale imaging of dynamic neural processes in acute brain slices and *in vivo*.

The new microscope achieves a lateral spatial resolution of ~50 nm at imaging depths of ~50 µm in living brain slices. It works with green fluorophores, including common fluorescent proteins like GFP and YFP, offering two-color contrast based on spectral detection and linear unmixing. Because of its upright design using a long working distance water-immersion objective, it was possible to incorporate electrophysiological techniques like patch-clamping or to add a stage for *in vivo* imaging.

I have used the new microscope to image fine neural processes and their nanoscale dynamics in different experimental preparations and brain regions, revealing new and interesting morphological features of dendrites and spines. In addition, I have explored different labeling strategies to be able to use STED microscopy for visualizing protein trafficking and dynamics at the nanoscale in brain slices.

Keywords :

Two-photon microscopy, STED, GFP

Unité de recherche

Institut Interdisciplinaire de NeuroSciences

UMR 5297 CNRS / Université Bordeaux Segalen

146, rue Léo Saignat, 33077 Bordeaux

"...can the human soul be glimpsed through a microscope?

Maybe, but you'd definitely need one of those very good ones with two eyepieces."

Woody Allen

in Palevitz et al. Protoplasma 109:23-55 (1981)

Acknowledgements

This work was conducted at the Interdisciplinary Institute for NeuroScience Bordeaux, UMR 5297 CNRS in the Group of Prof. Dr. U. Valentin Nägerl from October 2010 to March 2014.

I wish to thank my supervisor Valentin Nägerl for placing the trust in me to deal with the challenges associated for a psychologist-turned-neurobiologist to design, construct and operate a complex optical instrument. His fascination for this field has helped me pass dark times along the way.

I wish to express my gratitude to Giovanni Mariscano for his patience and his continuous support and trust.

I want to thank Ronan Chereau, fellow PhD student in the lab, for joining me on our endeavor for an academic degree and countless off-hours in the town of Bordeaux and my roommate Vera Pinhero for being such a great person.

Furthermore, present and former members of the team that have helped me accomplish this work include, Drs. Martin Lenz, Jan Tonnesen, Julie Angibaud, Elena Avignone, Aude Panatier, Misa Arizono and Fabien Nadrigny. Current PhD students in the lab that have supported me and surely will have a successful PhD defense at some point include Thomas Pfeiffer and Mirelle ter Veer.

I wish to thank the European Union for financing this PhD project under the ITN “SyMBaD” as well as the LABEX Brain initiative.

My parents Ingrid and Klaus as well as Johanna, Hans and Paul for continuous support.

Index

List of Figures

Abstract

Stimulated emission depletion (STED) microscopy is a recently developed "superresolution" or "nanoscopy" fluorescence microscopy technique that greatly improves the spatial resolution of light microscopy, which has classically been limited by the diffraction of light.

The advent of STED microscopy has created a lot of excitement in the field of neuroscience because many important neuronal structures, such as dendritic spines, axonal shafts or astroglial processes, cannot be properly resolved by regular light microscopy techniques.

Two-photon fluorescence microscopy is a widely used imaging technique in neuroscience because it permits imaging dynamic events deep inside light-scattering brain tissue, providing high optical sectioning and depth penetration. However, the spatial resolution of this approach is limited to around half a micron, and hence is inadequate for revealing many morphological details of neurons and synapses.

The aim of my PhD work was to A) develop a microscope that improves on two-photon imaging by combining it with STED microscopy and to B) demonstrate its potential for nanoscale imaging of dynamic neural processes in acute brain slices and *in vivo*.

The new microscope achieves a lateral spatial resolution of ~50 nm at imaging depths of ~50 µm in living brain slices. It works with green fluorophores, including common fluorescent proteins like GFP and YFP, offering two-color contrast based on spectral detection and linear unmixing. Because of its upright design using a long working distance water-immersion objective, it was possible to incorporate electrophysiological techniques like patch-clamping or to add a stage for *in vivo* imaging.

I have used the new microscope to image fine neural processes and their nanoscale dynamics in different experimental preparations and brain regions, revealing new and interesting morphological features of dendrites and spines. In addition, I have explored different labeling strategies to be able to use STED microscopy for visualizing protein trafficking and dynamics at the nanoscale in brain slices.

Résumé

Le cerveau humain se composent de quelque $8*10^{10}$ neurones et à peu près le même nombre de cellules non-neuronales et chaque neurone fait plusieurs milliers de synapses. Ces cellules sont très denses, formant la structure la plus complexe chez les vertébrés (et certains disent dans l'univers). Comme ces cellules individuelles sont capables de communiquer les unes avec les autres, ils forment la base de l'activité du réseau neuronal qui permet l'apparition de toutes les fonctions de base et supérieure du cerveau.

Par conséquent, la compréhension des principes d'action au niveau de la cellule unique est une condition préalable pour décrire, expliquer et prédire l'activité du réseau de groupes de cellules et pour, à terme, l'ensemble du cerveau.

La structure fine du système nerveux pose des défis considérables pour l'observation microscopique. Le tissu nerveux est dense et les structures d'intérêt de l’ordre du centimètre pour les différentes régions du cerveau et du nanomètre pour les contacts synaptiques et des molécules. Dans ces dimensions, les chercheurs en neurosciences tentent d'enregistrer simultanément les propriétés fonctionnelles et structurelles du tissu nerveux. Par conséquent, une technologie particulière a été développé pour répondre à ces exigences.

Dans cette thèse, je décris la construction d'un nouveau type microscope super-résolution qui utilise des fluorophores génétiquement encodés pour visualiser les structures neuronales sub-cellulaires jugées essentielles pour l'apprentissage et les mécanismes de mémorisation. Le microscope est capable d'améliorer la résolution d'un microscope photonique classique à deux photons d'un facteur de 6.4 en profondeur à l'intérieur du tissu cérébral.

J'ai défini les objectifs suivants auquel l'instrument doit répondre:

- Excitation par un laser accordable à deux photons

- Nature pulsé du laser de déplétion STED

- Microscope droit

- Objectif à immersion à eau

- GFP et YFP comme principaux fluorophores utilisés / possibilité d’obtenir un contraste double couleur

- Imagerie super résolution en profondeur dans le tissu vivant

- Compatibilité avec les techniques d’électrophysiologie

Le but de ce travail était donc de développer un microscope STED qui est difficilement compatible avec différent types d’échantillons de tissu cérébral couramment utilisés en neurosciences. Ce microscope permet l’imagerie à l’échelle nanométrique des cellules vivantes en utilisant des molécules et proteines fluorescentes classiquement utilisées en profondeur à l'intérieur des tissus de diffusion. Ce microscope devrait ouvrir un nouveau champ de possibilité et favoriser l’application de la microscopie STED en neurosciences.

La section des résultats comprend un chapitre du livre “Nanoscale Imaging of Synapses”, livre publié dans la série *Springer Neuromethods* Volume 84, Editors U. Valentin Nägerl et Antoine Triller. Ce chapitre se concentre principalement sur les aspects pratiques de la conception et de la construction d’un microscope STED à excitation deux photons.

La deuxième partie de la section des résultats comprend un article de recherche original publiée dans *Biophysical Journal* qui décrit le microscope et sa capacité à produire des images de super-résolution de structures neurales dans des tranches aigues de cerveau.

La dernière partie des résultats comprend diverses applications du microscope, démontrant l'imagerie à l'échelle nanométrique dans les préparations de tissus communs, tels que des cultures de cellules dissociées, cultures organotypique, des tranches aigues de cerveau et dans le cerveau intact d’un animal vivant. L'amélioration de la résolution du microscope a permis la description des fines structures dendritiques des cellules granulaires du gyrus denté et de micro-varicosités sur le cou des épines dendritiques ; ces caractéristiques structurelles des cellules neuronales ne pouvant pas être résolus par microscopie traditionnelle à deux photons. En outre, le microscope a été utilisé pour étudier si les niveaux de protéines endogènes de la souris transgénique VGLUT1-Venus ainsi que le cytosquelette d’actine marqué par des *nanobodies* dirigés étaient des modèles appropriés pour la microscopie STED.

Les résultats de cette thèse montrent que ces objectifs ont été atteints en utilisant un schéma d'excitation à deux photons combinée avec un laser pulsé STED sur un microscope droit avec un objectif à immersion à eau. En particulier l'utilisation du laser STED pulsé permet l’imagerie de cellules vivantes au cours du temps avec une résolution supérieure à celle régulièrement observée en microscopie à deux photons mais aussi en microscopie deux photons à déplétion STED continu. La difficulté associée avec des lasers à impulsions est la nécessité synchroniser les pulsations des deux sources de façon optimale et de pouvoir moduler les délais de phase des lasers. Comme les lasers accordables à deux photons possèdent une cavité de résonateur, où la lumière émise par le milieu de gain intervient pour former des ondes stationnaires (ou modes), la synchronisation à une fréquence de répétition d'impulsions externe exige une stabilisation précise de la longueur de la cavité. Contrairement aux rapports précédents qui utilisaient un oscillateur paramétrique optique construit sur mesure, le système décrit ici utilise une option commerciale pour les chercheurs qui n'ont pas les bases théoriques pour construire leurs propres lasers. En raison de la nature de la lumière pulsée STED, une puissance moyenne faible (~ 30 mW par rapport à ~ 200 mW pour les lasers CW dans le BFP) peut être utilisé, ce qui est important pour l’imagerie répétée de tissu vivantes. La précision du délai de l'impulsion STED par rapport à l'impulsion d'excitation permettent également la mesure de la durée du pulse de déplétion dans l’ordre de la picoseconde qui nécessiterait autrement des équipements sophistiqués tels qu’un autocorrélateur. En outre, ce système est également capable de sonder la durée de vie de fluorescence (FLIM) des molécules qui doivent permettre des mesures en profoncdeur sur des échantillons biologique épais.

1 Introduction

Although the history of microscopes is as old as the use of lenses and can be traced back to the 13th century, Zacharias Janssen is often acknowledged to be the first to build an optical microscope around 1590. With Antonie van Leeuwenhoek (1632-1723) being the first to observe bacteria and protozoa[1], and Galileo Galilei (1564 – 1642) becoming the father of the compound microscope, the success of optical microscopy has since been immense[2].

Much later, thanks to the staining method of Camillo Golgi[3] a major obstacle in the observation of nervous tissue was overcome: that is the contrast enhancement of a few stained cells versus the densely packed non-stained brain tissue. It was Santiago Ramón y Cajals[4] work on the microscope who optimized and used this staining technique to demonstrate that also the brain consist of individual cells and is not a syncytium as proposed by Gerlach[5] and Golgi[6].

The cell theory’s success in identifying the cell as the basic fundamental unit of all living things, laid the ground for modern neuroscience. It has since thriven to become one of the fastest growing disciplines within life science. This was only possible because a novel labelling technique (Golgi’s staining) and excellent microscopic observation (Santiago Ramón y Cajal) were brought together to unravel the dominating problem of the time, the make-up of the brain’s tissue.

In our times, cellular neuroscience is facing a very similar problem:

> How can we explain the workings of sub-cellular compartments that are too small to be observed with traditional microscopes?

And again, both a novel labelling technique (genetic encoded fluorophores) and a novel microscopic technique (superresolution STED microscopy) have been developed around the same time. These technological advances allow formerly blurred structures to be visualised with unprecedented sharpness in real time inside living tissue.

In this thesis, I describe the construction of a novel superresolution microscope that uses genetically encoded fluorophores to visualise sub-cellular neuronal structures believed to be essential for learning and memory. The microscope is able to improve upon the later resolution of a regular two-photon microscopy by a factor of 4-6 deep inside brain tissue.

1.1 A cellular view on the nervous system

The human brain consist of an estimated $8 * 10^{10}$ neurons and roughly the same number of non-neuronal cells [7] and each neuron forms several thousands of synapses. These cells are densely packed, forming the most complex structure in vertebrates (and some say in the universe). As these single cells are capable of communicating with each other, they form the basis of neuronal network activity that allows the emergence of all basic and higher brain function. But the network would not function without its core components.

Therefore, understanding the principles of action on the single cell level is a prerequisite for describing, explaining and predicting the network activity from clusters of cells to, eventually, the whole brain.

The smallest components of the brain are neurons and glia cells. While neurons receive, compute and transmit information, glia cells have had traditionally only a supportive role. This view has recently been challenged by evidence that suggests glia cell contribute to network activity via modulation of synaptic transmission[8].

While a vast diversity of neuronal morphologies have been reported, the classic view describes neurons as an polarized cell that receive its input via synapses located on dendrites or the cell body and an axon that transmits the information via action potentials to the next cell. Membrane depolarisation due to synaptic inputs on the dendrite is conveyed to the somatic region via electrotonic spread of the membrane potential. If the action potential firing threshold at the soma is reached, an action potential is generated in the axon initial segment which travels along the axon by a regenerative process via voltage-gated sodium and potassium channels. The action potential then triggers vesicle release on axonal boutons that convey information to the next cell.

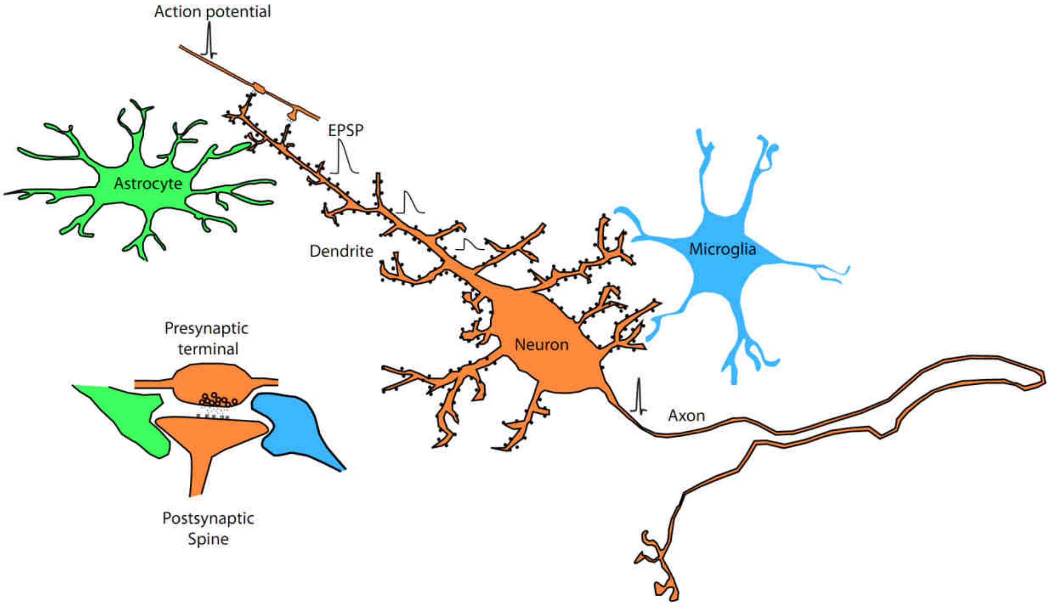

Figure 1: Key cellular members of the nervous system

The neuron together with astrocytes and microglia (and other glia) make up the cells of the nervous system. While the neuron sends and receives information via the synapse depicted on the left, the glia have supportive role and are now to believed to be able to modulate the neuronal information transfer. The classic view of the excitatory neuron describes elongated dendrites stubbed with postsynaptic spines, a somatic region and a long, thin axon that sends action potentials to its presynaptic terminals that release synaptic vesicles filled with neurotransmitter.

Synapses are highly specialised cell-cell junctions that consist of a presynaptic and a postsynaptic component. The digital nature of an action potential arrival at a presynaptic terminal is encoded into synaptic vesicle fusion to the membrane which leads to a release of neurotransmitter into the synaptic cleft. These neurotransmitters can bind to postsynaptic receptors which lead to a change in the postsynaptic membrane potential via the influx of ions. The synapse is therefore both a digital-to-analog converter and encodes electrical to chemical activity. This unique feature allows for an efficient and fast information transfer via action potentials, a broad range of modulatory action on both the side of vesicle release, neurotransmitter action and postsynaptic response, and analog integration of membrane potential changes induced by the activity of several synapses on the dendrite.

For example, a short delay between the arrival times of two action potentials can modulate the vesicle fusion probability; neurotransmitter concentration in the synaptic cleft over time can be modulated via re-uptake into the presynaptic cell or degradation; and the function of postsynaptic neurotransmitter receptors can be modulated by post-translational phosphorylation or membrane potential alteration.

The highly modulatory nature of synaptic function is believed to be a core mechanism for the functions of the brain, as the strength of a synaptic connection can be altered by synaptic activity alone. This ability renders the synapse the smallest independent computational unit in the nervous system as it can function both as a detector as well as an executive unit.

This phenomenon is known as synaptic plasticity and refers to a long lasting change of synaptic strength as a response to a change in synaptic activity. It defines one of the most fundamental learning rules of neuronal network theory, that is the famous quote from Donald O. Hebb’s book in 1949:

> “When an axon of cell A is near enough to excite cell B and repeatedly or persistently takes part in firing it, some growth process or metabolic change takes place in one or both cells such that A's efficiency, as one of the cells firing B, is increased." [9]

The mentioned “growth process or metabolic change” is also termed morpho-functional plasticity and refers to the fact that postsynaptic specialisations of excitatory synapses (dendritic spines) can undergo a morphological change that is correlated with a change in the transmission strength of the associated synapse. This link between morphology and functionality is a current dogma in the field of neurobiology. It states that by observation of a change in neuronal structure one can infer upon a change in neuronal function.

The density, the complex cellular architecture and the lack of contrast between cells of the nervous tissue poses a considerable challenge for direct observation of structure. A contrast enhancement of single cells was first made possible by the Golgi staining method[3]. Here, for unknown reason, only very few cells are intensely stained while the majority of cells remain unstained. The microscopic observation of this staining technique allowed Santiago Ramón y Cajal, in addition to applying the cell theory to the nervous tissue, to identify most subtypes of neuronal cells and reconstruct the fundamental connectivity pattern within various regions of the brain.

Among those regions, two have received special attention from neurobiologists.

The cerebral cortex is, phylogenetically speaking, the youngest part of the brain and constitutes most of the surface area of the brain in higher mammals. It is considered as the integrative center of the brain and its development during evolution has allowed the emergence of higher brain functions.

The hippocampus is a part of the cortex and located in primates in the temporal lobe of the telencephalon. The highly organised and well characterised cellular architecture of the hippocampus, in addition to its role in memory consolidation and spatial navigation, has rendered it a valuable structure for neuroscience. For example, dendrites of the Cornu ammonis 1 (CA1) area extend into the Stratum radiatum where they are innervated by axons from CA3 cells. This allows electrophysiologists to place recording and stimulation electrodes in defined regions to record synchronized neuronal activity, greatly enhancing the signal-to-noise ratio.

This classic recording paradigm has proven to be a valuable tool for the identification of cellular mechanism of learning and memory[10].

Located below the surface of the brain, the hippocampus is most commonly accessed by cutting the brain of rats or mice to harvest acute brain slices, culturing the whole hippocampus as organotypic slice cultures or dissociate and culture individual hippocampal cells on glass coverslips as dispersed hippocampal cell cultures.

As optical accessibility is highest for dissociated neurons but the cellular architecture of the hippocampus is most conserved in acute brain slices, different experimental preparations are used depending on the scientific question. This poses the problem that oftentimes cell culture results are hard to replicate in more intact systems. The most intact system is, of course, the brain itself. For *in vivo* preparations, the skull of the animal is opened to gain access to the surface of the brain, commonly restricting access to superficial cortical areas such as somatosensory, motor and visual cortex.

Independently on the preparation used, the contrast problem in living brain tissue still prevails as the Golgi staining is incompatible with live cells. Fortunately, the discovery of the green fluorescent protein (GFP) allowed the final break-through. With this tool, sufficient contrast could be obtained that allowed the observation of single cells within living tissue.

GFP originates from *Aequorea Victoria*, is 238 amino acid longs and spontaneously matures within living cells. Its expression does not interefere with normal cell function and several tens of mutations have been introduced to create a library of fluorescent proteins with optimised brightness and photo stability, different excitation and emission spectra and sensitivity for pH and intracellular calcium levels[11]. Once cloned, GFP could be introduced to cells by means of gene delivery and mouse lines that express GFP in a subset of neurons are now routinely used.

Once the GFP molecule is excited, it emits green light that can be recorded through appropriate spectral filters, allowing the observation of a small number of fluorescent cells against a non-fluorescent background. It is fluorescence microscopy that allows the use of this contrast for the observation of living cells in intact tissue. Now, the structure-function relationship of synaptic plasticity can be observed in a non-invasive way. Fluorescence microscopy is also the basis for all recently developed superresolution microscopy techniques.

1.2 Fluorescence microscopy

Fluorescence can occur in fluorophores after absorption of light. A fluorescent molecule is usually excited to a higher electronic state from its lowest energy state (S0) by the energy delivered by a photon. This process can only occur if the energy delivered by the photon is equal to or slightly higher than the energy gap between the ground state and an excited state (i.e. S1) resulting in a continuum of photon energy to excite the molecule (excitation spectrum).

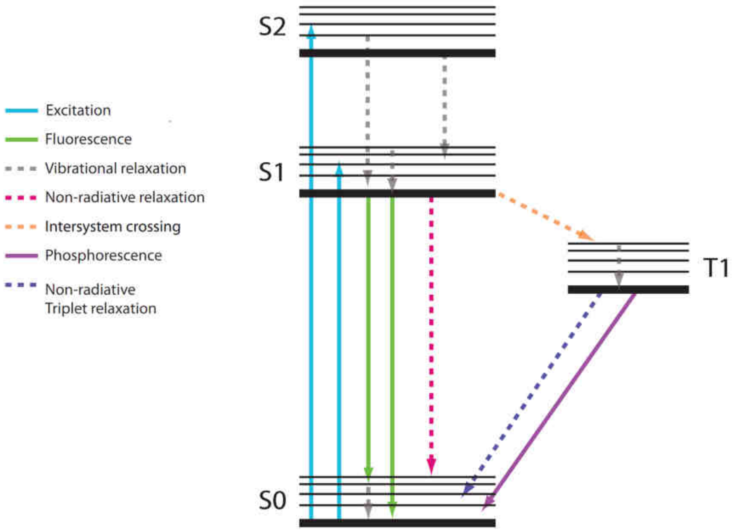

Figure 2: Jablonski diagram of the energy levels of a fluorophore

Main molecular pathways upon absorption of a single photon. Singlet states (S0, S1, S2) and triplet state (T1) are shown as well as radiative (solid arrows) and non-radiative (dashed) transitions between the energy states[12].

The excitation process typically takes within 10^{-15} seconds. Once excited, the electron relaxes via vibrational relaxation (between 10^{-12} to 10^{-15}seconds) to the lowest vibrational level of the excited state. The molecule remains in the excited state for typically 10^{-9} seconds (fluorescence lifetime) before it relaxes back to its ground state. This radiative relaxation process is called fluorescence and takes place by the emission of a photon of less energy than the excitation photon due to non-radiative vibrational relaxation. The difference in energy between the excitation and the emission photon is termed Stokes shift and is usually in the range of 20-100 nm. The reason for the relatively broad emission spectra of most fluorophores is the different closely spaced vibrational levels to which the molecule can relax.

A molecule can also relax non-radiatively via dissipation of heat or collision with another molecule. In addition, an intersystem crossing can occur where the molecule relaxes from the lowest vibrational level of S1 to the lowest excited triplet state T1. From here the molecule can relax to the lowest vibrational level of T1 via vibrational relaxation and further relaxation to S0 via phosphorescence or non-radiative Triplet relaxation. The transition from excited T1 to S0 is spin forbidden which results in long lifetimes in the triplet state[13]. Molecules in T1 readily react with molecular oxygen that destroys the molecule and is therefore considered a major pathway of fluorophore bleaching. The fraction of molecules that relax to the ground state via fluorescence over the ones that do not relax via fluorescence define the quantum yield of a molecule.

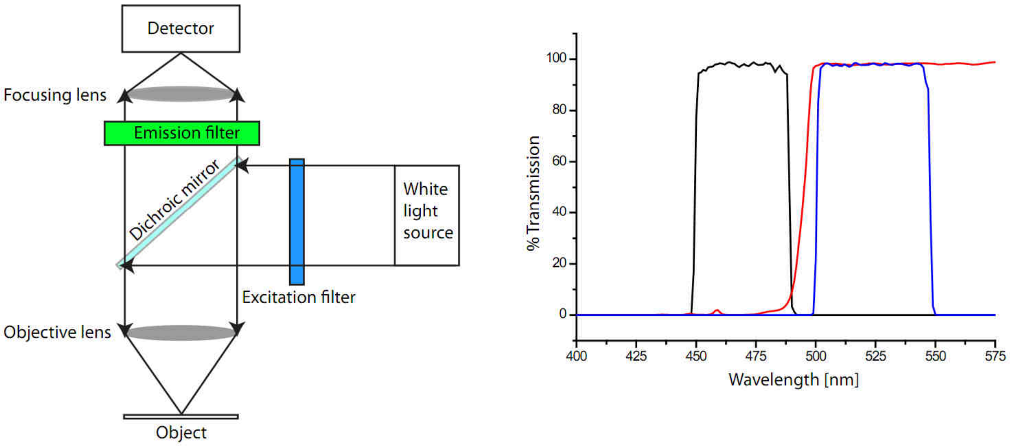

Figure 3: **Schematic principle of fluorescence microscopy**

The light from a white light source passes an excitation filter and gets reflected towards the objective by a dichroic filter. The signal light of the object passes the dichroic mirror and an emission filter on its way to the detector. Example spectral data of a FITC/EGFP filter cube (49002) from Chroma Technology.

In fluorescence wide-field microscopy, suitable optical filters allow the excitation light to enter the sample but prevent excitation light reaching the detectors so that only the emission light of the molecule is detected. The strength of fluorescent microscopy lies in its compatibility with live-cell imaging due to the non-invasive image formation, contrast of labelled to non-labelled targets, high flexibility of labelling strategies (genetic encoded fluorophores, fluorescent antibody labelling, patch-clamp loading and more) and specificity of targets through the use of genetic strategies such as cell-type sensitive expression patterns or antibody mediated labelling.

The above shown schema demonstrates the functionality of a classic widefield fluorescence microscope. The wavelength for excitation of the fluorophore is isolated from a white light source (such as a mercury or xenon arc lamp) by the excitation filter. The dichroic mirror (which has low transmission and high reflection) for the excitation light directs the light towards the objective. The signal light is transmitted by the dichroic mirror, spectrally cleaned by the emission filter and visualised via an eyepiece or a camera. As a consequence, an image is formed simultaneously and parallel by a magnifying lens for all objects in a given plane.

This stands in contrast to confocal microscopy [14, 15] where the image is formed sequentially by raster-scanning a diffraction limited spot (excitation PSF) across the sample. For each point the signal is recorded to allow the post-hoc assembly of an image. Image formation speed depends on pixel size and pixel dwell time. The term ‘confocal’ is defined as having a same focus, and refers to the fact that for any scan angle, the signal light is focused on the same detector area. This is either realised by moving the object plane with a motorised stage or by scanning the beam with galvanometric mirrors through a lens system that allows angular deflection of the excitation beam in the back focal plane (BFP) of the objective. There are several ways to design a scan system to accomplish a stable illumination of the BFP but is often realised via a telescope of two lenses whose focal points are matched to the BFP and to each other. As the signal light is transmitted back via the same scan mirrors (de-scanned), the scan angle deflections are compensated and create a stationary beam towards the detectors. As the detection pathway incorporates a pinhole that is precisely located in the conjugate plane to the object plane, it effectively blocks out-of-focus light to reach the detector light which permits the detector to record signals from only one spot in the sample (detection PSF). As a consequence the recorded image is a product of both the excitation and the detection

PSF which allows for optical sectioning and improved resolution. Three dimensional volumes are recorded by recording two-dimensional images of different planes along the z-axis that can later be reconstructed.

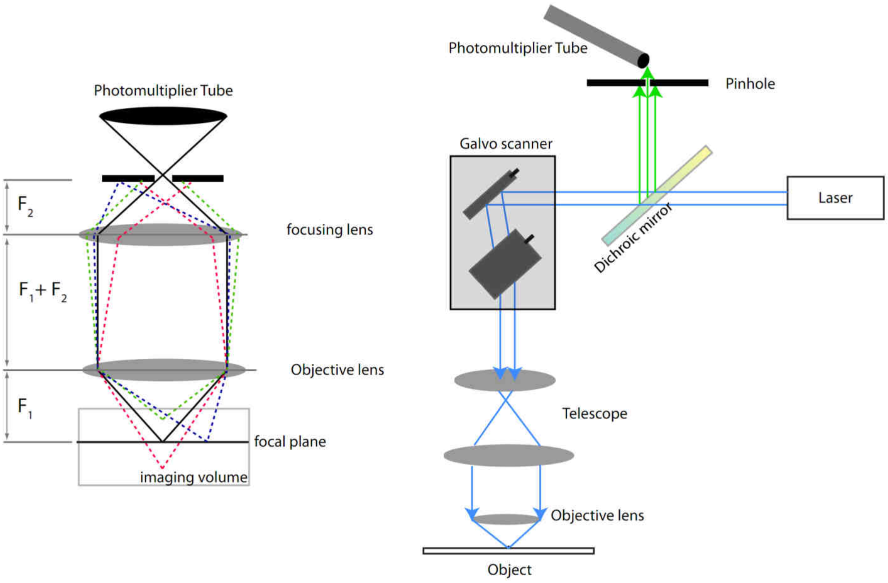

Figure 4: Schematics of confocal microscopy

The basic principle and advantage of confocal microscopy is out-of-focus light rejection through the use of a confocal pinhole before the detector. On the right, the beam path of a typical confocal microscope is shown. A coherent laser beam is scanner across the sample via mirrors mounted on galvanometers. The emission light is separated from the excitation light via a dichroic mirror and sent through the confocal pinhole towards the point-detector (usually PMTs).

Because of the inertia of the scan mirrors, the fast axis of the scanner is moved continuously. As a consequence the pixel size refers to the sampling frequency of the detector in time (over the amplitude of the scanner deflection) while the pixel dwell time refers to the speed of the movement of the fast axis (over the sampling frequency). These parameters should be set according to the sample quality but need to adhere to the Nyquist-Shannon sampling theorem to be able to record the maximum spatial resolution. In the case of fluorescent microscopy the sample should not be oversampled to minimize sample illumination and bleaching.

As the confocal pinhole blocks a majority of the light sent to the detectors and signal intensity is a major concern in optical microscopy, the pinhole diameter has a direct effect on signal strength and resolution. A good trade-off between resolution and signal strength is a diameter of the pinhole that is equal to one airy unit (AU) which corresponds to the diameter of the first minimum ring of the excitation PSF. This allows approx. 80% of the signal to pass the pinhole.

Decreasing the pinhole size beyond further will only decrease signal levels without increasing resolution as the resolution of the confocal microscope is defined by the product of the excitation PSF and the emission PSF and the excitation PSF is unaltered by the decreased pinhole size.

The above implementations (wide-field and confocal) of fluorescence microscope both rely on a single-photon excitation process. In addition, molecules can also be excited by a two-photon process which is utilized in two-photon excitation microscopy.

First predicted in the doctoral dissertation of Maria Göppert-Mayer in 1930[16, 17] (but see [18]), atoms can also be excited to higher energy states by the quasi-simultaneous absorption of two photons of approx. half the energy as compared to single-photon excitation. More exactly, she could show that the energy needed to excite an atom can be expressed as the sum of the necessary excitation energy. For practical reasons, this is usually achieved by two photons of the same energy but can also be realised with the two photons of different energy as long as their sum is equal, or slightly larger, then the excitation energy[19-22].

Experimental demonstration of two-photon excitation fluorescence was achieved only 30 years later in 1961 when ruby optical masers became available to laboratories[23]. Kaiser and Garret were able to excite $CaF_2:Eu^{2+}$ crystals with red light of 694 nm and record blue light of 425 nm. In their paper the efficiency of two-photon excitation was calculated to be on the order of 10^{-7} which indicates the extremely low probability of two photon excitation. Higher-order multi-photon processes such as three-photon excitation, were later also demonstrated[24].

The extremely low probability of the two-photon excitation process is compensated by compressing the excitation volume in space via an objective and in time by using ultrafast pulsed lasers.

The number n_a of photons absorbed per fluorophore per pulse, given the paraxial approximation, depends on

$$n_a \approx \frac{p_0^2\sigma}{\tau_p f_p^2}\left(\frac{(NA)^2}{2\hbar c\lambda}\right)^2 \tag{1.1}$$

With p_0 as the average laser intensity, σ the fluorophore's two-photon absorption cross section at wavelength λ, τ_p the pulse duration, f_p the lasers pulse repetition frequency, *NA* the numerical aperture of the objective and $\hbar$ the Planck's constant and c the speed of light[25, 26].

From this formula it becomes apparent that the two-photon excitation probability is proportional to the square of the laser power, to the 4th power on the NA and inverse proportional to the pulse duration.

These parameters have several important consequences for two-photon excitation fluorescence microscopy.

The quadratic dependency of two-photon absorption probability on excitation intensity and the roughly quadratic dependency of the excitation PSF intensity on distance from the focal plane results in a fourth power dependency of the two-photon excitation probability on distance [27, 28]. Therefore, two-photon excitation microscopy has intrinsic optical sectioning capability which allows the collection of all photons as signal photons, making a pinhole in front of the detector obsolete. This, in turn, means that a much greater proportion of photons can be detected, especially in scattering medium, resulting in a better signal-to-noise ratio.

As two-photon excitation occurs only in the focal plane, out-of-focus bleaching is greatly reduced, allowing time-lapse imaging of three-dimensional structures.

The use of near-IR light dramatically increases the penetration depth of the excitation light in biological samples as scattering is proportional to the inverse fourth power ($\propto \lambda^{-4}$) of the wavelength used (for particles smaller than the wavelength of light –

Rayleigh scattering)[28] and for particles larger than the wavelength of light to the inverse third power($\propto \lambda^{-3}$)[12].

The numerical apperature $NA = n(\sin \alpha)$ of the objective is ultimately limited (theoretical max. $\alpha = 90°$ current max. $73°$)[29] by the refractive index of the immersion medium and cannot increased beyond that of the lens material[30]. For two-photon microscopy water-immersion objectives are usually used which have a lower NA then oil-immersion objectives.

The pulse duration of the pulses is limited by the fact that shorter pulses are stretched in time more than longer pulses. For a given optical system with fixed amounts of glass, a Gaussian pulse is temporal broadened more if the incoming pulse is shorter and broadened less if the incoming pulse is longer. This typically results in pulse durations for two-photon excitation microscopy on the order of 200 fs.

1.3 Nanoscopy with focused light

As shown by Ernst Abbe, light can be focused by an objective lens to finite spot. Because in fluorescent microscopy, this finite spot samples the spatial frequency of the observed structure, its size defines the resolution of an optical microscope.

The size of the finite spot is characterised in the lateral dimension by the full-width-at-half-maximum (FWHM) and is known as the diffraction limit of light by

$$\Delta r \approx \frac{\lambda}{2n\ \sin\alpha} = \frac{\lambda}{2NA} \tag{1.2}$$

where λ denotes the wavelength, *n* the refractive index of the immersion media and α the semiaperture angle of the objective lens and NA the numerical aperture of the objective.

The diffraction limit of light is a direct consequence of the wave nature of light and related to Heisenberg's uncertainty principle.

Since

$$\Delta E \Delta t > h \tag{1.3}$$

with h = Planck' constant and $\nu =$ frequency of the light, a uncertainty in the arrival times of the photons due to different path lengths emerges

$$\Delta t = t_2 - t_1 > \frac{1}{\nu} \tag{1.4}$$

As a result of the different arrival times, the focused photons show a phase difference that gives rise to the intensity distribution at the focal spot (excitation PSF)[31].

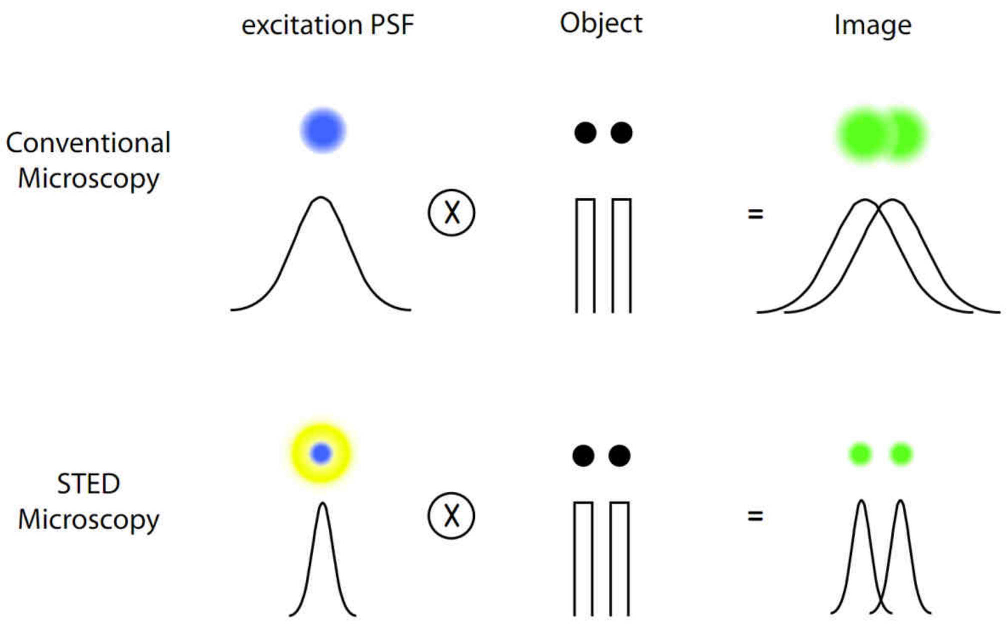

Figure 5: Image formation by convolution of PSF with object

In confocal scanning microscopy, the excitation PSF is scanned across the field of view. The image is then a function of the convolution of the excitation PSF with an object and recorded by the imaging system yielding the effective PSF (image). If two closely spaced objects cannot be discriminated from each other, the resolution limit of the imaging system has been reached. This is described by the Rayleigh criterion and states that these two objects can be resolved if the minimum of first object PSF coincides with the maximum of the second object's PSF. Effectively, this corresponds to a drop in the intensity between two equally bright objects of 26%. In STED microscopy, the effective excitation PSF is reduced and hence yields a smaller effective PSF which allows the separation of closely spaced objects.

Ernst Abbe's description of the resolution limit of far-field optical microscope by his famous formula illustrates that by reducing the wavelength of light, higher spatial resolution can be achieved. For living biological samples, however, the high photon energy of light below approx. 400 nm is detrimental and because of the linear relationship between resolution and wavelength, achieving sub-100 nm resolution would force the use of light < 280 nm. This ultra-violet regime is also called germicidal because it kills microorganisms and is hence not suitable with live cell microscopy. Also, the NA of the objective can only be increased to a certain limit.

Far-field fluorescence microscopy resolution was hence limited by the diffraction limit of light until 1994 when Hell, S.W. and colleagues have developed the theoretical foundations of stimulated emission depletion (STED) microscopy that allows the image formation with theoretically unlimited resolution[32]. While the resolution limit of far-field optical microscopy, as described by Ernst Abbe still stands, several ways around this hard limit have been demonstrated.

In contrast to later developed localisation-based superresolution techniques such as photoactivated localisation microscopy (PALM)[33, 34], stochastic optical localisation microscopy (STORM)[35] and structured illumination microscopy (SIM)[36] which work on the principle of single molecule observation and localisation, or patterned illumination and measuring of the fringes in the Moiré pattern in case of SIM, STED operates on the principle of modulation of the excitation point-spread function by a second, doughnut-shaped depletion laser.

As the work presented in this thesis is about the construction of a two-photon STED microscope, I refer for review articles on PALM, STORM and SIM to the literature [37-40]. It shall be noted however, that localisation based techniques are almost exclusively operated in total-internal-reflection (TIRF) mode which restricts their use to monolayer cultures, while the STED approach is readily suitable with thick biological preparations.

Stimulated emission depletion microscopy is theoretically able to achieve unlimited resolution due to a concept known as RESOLFT (for reversible saturable optical fluorescence transition).

The RESOLFT formalism[41] can be described by assuming transitions of a fluorescent molecule between two distinct states A → B that can be optically driven at a rate $k_{AB} = \sigma I$ where σ is the transition cross-section and I the light intensity. In turn, the transition between $B \rightarrow A = k_{BA}$ can be driven by light, heat, others or spontaneous. The kinetics between these states are described by

$$\frac{dN_A}{dt} = -\frac{dN_B}{dt} = k_{BA}N_B - k_{AB}N_A \tag{1.5}$$

with $N_{A,B}$ denoting the normalized population probability of each state. After time $t \gg (k_{AB}+k_{BA})^{-1}$ i.e. $t \approx 5(k_{AB} + k_{BA})^{-1}$ the populations have reached a dynamic equilibrium at $N_A^{\infty} = k_{BA}/(k_{AB} + k_{BA})$. Now the probability of a molecule to be in either A or B depends on k_{AB} and therefore on I.

At the saturation intensity $I_{sat} = k_{BA}/\sigma$ an equal probability $N_A^{\infty} = 1/2$. Increasing $I \gg I_{sat}$ renders $k_{AB} \gg k_{BA}$ so that the molecule is shifted to B with $N_A^{\infty} \rightarrow 0$.

This relationship can be utilised for creating arbitrarily sharp regions of A. The spatial intensity distribution $I = I(x)$ can be made zero for point x: $I(x_i) = 0$ by a standing wave $I = I_0 \cos^2(2\pi n x/\lambda)$ for one dimension. For $I_0 \gg I_{sat}$ all molecules would be in state B, except for the ones close to $x = x_i$. The larger the ratio of $I/I_{sat} \gg 1$ the smaller the region of state A.

The FWHM of the resulting spot that remains in A is then

$$\Delta x = \frac{\lambda}{\pi n \sqrt{I/I_{sat}}} \tag{1.6}$$

and for focusing light through the finite aperture of a microscope objective it follows

$$\Delta x = \frac{\lambda}{2n \sin\alpha \sqrt{1 + I/I_{sat}}} \tag{1.7}$$

Now Δx is also dependent on I which results for I/I_{sat} = 100 in an improvement of Abbe's law by the factor of 10[29].

For two- or three dimensional $I(x_i = 0)$ the spatial intensity distribution would be described by a 2D or 3D doughnut mode.

In STED microscopy, the first implementation of RESOLFT microscopy, the state A refers to the fluorescent form of a fluorescent molecule and state B to the ground state (non-fluorescent). The transition $A \rightarrow B$ is realised via the principle of stimulated emission, a process with a cross-section σ = 10^{-16} - 10^{-18} cm^2. As STED competes with spontaneous fluorescent decay $f_{fl} \approx (1\ ns)^{-1}$, I_{sat} can be estimated by k_{fl}/σ to approx. 10-100 MW/cm^2[41].

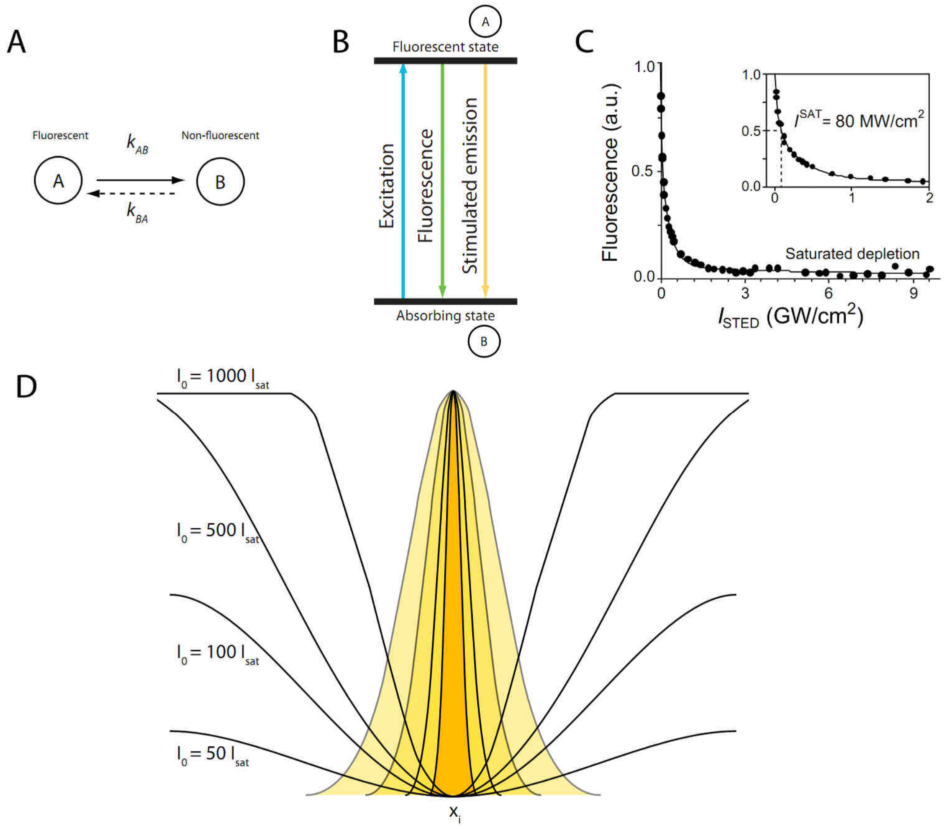

Figure 6: Principle of STED microscopy by the RESOLFT approach

The principle of STED using the RESOLFT concept can be illustrated utilizing a fluorescent state A and a non-fluorescent state B. In STED, the transition from A to B is achieved via intense light illumination that depletes the excited states of the molecule before it can relax via the fluorescent process B. C) Saturated depletion of the S1 with increasing STED pulse intensity I_{STED}, as measured by the remaining fluorescence of an organic fluorophore. Depletion of the S1 saturates with increasing I_{STED} and therefore establishes a nonlinear relationship between the fluorescence and the intensity applied for STED. The saturation is the essential element for the breaking of the diffraction barrier. Figure and text from[41]. D) The yellow shaded profiles illustrate the spatial region in which the molecule is allowed to reside in state A. Increasing I_0 results in an ever decreasing space and hence increase spatial resolution of a microscope which utilizes this process by scanning it across a fluorescent sample. Figure is motivated from Figure 31.1 in [29].

The RESOLFT concept can also realised with different molecular states, such as the triplet state or different emission spectra of photo-switchable proteins.

In ground-state-depletion (GSD) microscopy State A is the ground state S0 while state B refers to the triplet state. Conversion between A and B occurs as a by-product of regular excitation because with every excitation cycle the molecule crosses the triplet state with a probability of $p \approx 0.05$ to 0.2 [42, 43].

Photo-convertible fluorophores have also been utilized in the RESOLFT concept. Here, both states (A and B) are fluorescent but with different emission wavelengths that can be separated by appropriate filters. Only low light intensities are need for the cis-trans isomerisation of fluorophores such as asFP95[29], Dronpa-M159T-GE[44] rsEGFP(N205S)[45]. While initially these photoswitchable proteins suffered from low fluorescence yield and slow switching kinetics, further protein engineering should allow much faster image recording times.

A simple way of realizing saturated optical transition is via intense excitation that depletes the ground state of a fluorescent molecule and is expected to reside in the fluorescent state. Here, state B is fluorescent and state A is non-fluorescent and hence creates a negative image[29, 46].

Within this thesis I describe STED microscopy of the fluorescent proteins GFP and YFP that uses pulsed light at a wavelength of 600 nm for the state transition $A \rightarrow B$ while excitation is realized by a two-photon process using femtosecond pulses with a center wavelength around $\lambda = 910$ nm.

1.4 Motivation

The fine structure of the nervous system poses considerable challenges for microscopic observation. The nervous tissue is densely packed and structures of interest range from millimetres (brain areas) to nanometres (synaptic cleft) and single molecules. Within these dimensions, neuroscience researchers try to record both structural as well as functional properties of the tissue. Therefore, specialised technology has been developed to meet these demands.

As described above, the resolution limit of light microscopy has posed a hard limit for the recording of fine details. With the advent of superresolution technology, these techniques are being applied to neuroscience. With the necessary equipment being expensive and require a high level of expertise on the user side, the applications of STED microscopy for neuroscience questions are few but noteworthy.

The synaptic vesicle protein synaptotagmin-1 was studied in fixed hippocampal neurons and STED imaging revealed prolonged synaptotagmin-1 clusters after the fission of the vesicle with the membrane, indicating that at least some vesicles are recycled in an intact fashion[47].

In living cultured neurons, a video-rate STED microscope was used to study the dynamics of single vesicles in axonal boutons. It was found that vesicles move quicker inside then outside the boutons[48]. The presynaptic protein bruchpilot was observed to be organised in a doughnut-shaped fashion, centered at the active zone of the neuromuscular junction. This protein is essential for development of the electron-dense projections (T-bars) and crucial for the Ca^{2+} channel organisation and therefore also for synaptic vesicle release [49, 50].

In recent years, our group has pioneered STED imaging of neuronal structures in organotypic slice cultures. A first report in 2008 showed the feasibility of STED microscopy in living cultured hippocampal slices, which is a more intact culture preparation then dispersed hippocampal neuron cultures. This work also demonstrated extended time-lapse imaging of dendritic spines expressing YFP in a paradigm of chemical LTP induction and subsequent morphological reorganisation of the spine head and neck[51, 52]. Subsequent work extended the choice of fluorophores to life-act YFP expressing neurons (a marker for actin) for live-cell, time-lapse imaging and demonstrated the advantage of using a glycerol immersion objective to increase penetration depth of STED microscopy[53]. Lately, the simultaneous superresolution imaging of two genetic encoded fluorophores (GFP and YFP) was demonstrated in our group. In contrast to previous approaches, this paper reports on the feasibility of using only two laser beams (one for excitation and one for depletion) for the two fluorophores. As the two fluorophores are excited, quenched and recorded simultaneously by two detectors, they are inherently co-aligned and detected at the same time.

Work from the group of Stephan Hell has recently demonstrated that is possible to use STED microscopy *in vivo* to image dendritic segments and spines in mouse cortex[54].

Localisation based superresolution imaging approaches such as PALM and STORM have also made tremendous contributions to the nanoscale organisation of neuronal structures. As an example, the periodic organisation of the actin cytoskeleton in the axon was revealed using STORM imaging in cultured rat hippocampal cells [55]. Here it was also shown how spectrin, adducin and voltage-gated sodium channels are arranged within the actin organisation. Another landmark paper from the same group reports on the molecular architecture of chemical synapses in the brain using multi-color, three-dimensional STORM. Labelling the presynaptic protein Basson and the postsynaptic protein Homer1 among ten others, they were able to measure the synaptic cleft and the organisation of the proteins within (and with respect to their C- and N- termii) the synapse[56].

STED microscopes classically excite the fluorophore via a one-photon process and the signal is detected after a pinhole. It can therefore be accurately described as a confocal microscope with an increased resolution. The objectives used are typically high NA oil or glycerol objectives and the microscope is constructed as an inverted design for mechanical stability. This is unfortunately largely incompatible with thick tissue preparations because single-photon excitation is subject to strong absorption and scattering and the inverted design impedes concurrent electrophysiological recordings. An upright microscope design and two-photon excitation would therefore greatly facilitate depth penetration and compatibility with electrophysiology.

The proof-of-principle demonstration of two-photon excitation STED microscopy was achieved by Moneron et al. in 2009[57] who used a non-tunable two-photon laser (λ=1060 nm, 117 MHz pulse repetition rate) for excitation of Nile Red and ATTO 565 fluorophores. A continuous-wave (CW) krypton laser (λ= 676 nm) was used for the STED doughnut with about 200 mW in the back-focal plane. The microscope was constructed around an inverted design and a 1.4 NA oil-immersion objective. The sample was scanned by a 3D piezo stage which facilitates the design of the excitation and detection optics but is relatively slow in terms of pixel dwell times and largely incompatible with live-cell imaging and electrophysiology due to motion effects. The resolution obtained was reported to be FWHM of 50 nm with is 4-5 times better than what would be expected from the two-photon excitation beam alone. The samples used were fluorescent beads for the demonstration of the resolution enhancement and the transcription regulator NFκB in the cell nucleus of PtK2 cells by primary and secondary antibodies labelling with ATTO 565. A clear resolution enhancement was observable in the NFκB staining.

The first report of using two-photon excitation STED microscopy for imaging acute brain slices was shown by Ding et al. [58]. A tunable pulsed Ti:sapphire laser (λ=840 nm) and a Ti:sapphire laser operating in continuous-wave mode at λ=760 nm were used to image neurons (patch-filled with Alexa 594) and Crimson Red fluorescent beads. The microscope featured an upright design and employed a 1.1 NA, water-immersion objective. In contrast to the first report, the laser beams were scanned across the field of view by a custom scanner that featured a converging silver mirror and two galvanometrically driven mirrors. The group shows a resolution enhancement in Crimson Red beads of FWHM of 280 nm which is reported as a two-fold increase and a resolution enhancement in spines of CA1 pyramidal cell dendrites with a reported 280 nm spine neck width. A strength of this study lies in the optical design because both wavelengths used are within the near-IR regime. As a consequence, only red dyes can be used for this microscope which have to be patch-filled into cells.

The previous reports featured femtosecond pulsed lasers for excitation but the STED power was delivered by a continuous-wave laser. Although this is technically easier to realise, the extended illumination of the sample during periods where the fluorophore is not excited (and can hence not be quenched) is likely to be prohibitive for extended time-lapse imaging of living cells. A STED microscope that also features pulsed STED depletion would be advantageous and has been reported by Li et al. [59]. Here, an inverted microscope, featuring an oil-immersion objective, was used to excite GFP molecules by a two-photon laser (λ=850 nm) while the pulsed STED laser (λ=580 nm, pulse duration = 200 ps) originated from a synchronised, custom-built optical parametric oscillator. Because of the 580 nm STED light, they were able to resolve EGFP tagged Caveolin-1 in CHO cells and reported a single caveolar vesicle with a FWHM of 68 nm. The design and selection of the lasers were carried out for superresolution imaging of GFP and other green fluorophores but the sample was scanned with a 3D piezo-scanning stage, which is largely incompatible with live-cell imaging and electrophysiology.

Recently, the group of B. Sabatini recently published a paper where they present an upgraded version of their 2PE-STED microscope, from a system based on a continuous-wave STED[60] to a pulsed STED laser[61]. Here, two Ti:sapphire lasers operating in pulsed mode (λ=810 nm for excitation and λ= 736 nm for STED) were synchronised to excite and quench Alexa 594. This allows a resolution of 60 nm at a depth of around 30 µm in acute brain slices. As both beams operate in the near-IR and a spectrally close, chromatic aberration is minimised but the choice of fluorophores is limited to red dyes.

A novel approach using only a single laser was reported by Bianchini et al.[62]. Here microtubules were immunolabelled with ATTO647N and a resolution of FWHM = 80 nm was reported. The novelty of this approach is the demonstration that the same wavelength can be used for two-photon excitation and STED microscopy. The output of the laser was split so that one part of the laser power could be used for classic femtosecond pulsed two-photon excitation while the other part of the power was directed through glass rods and a polarisation-maintaining single-mode fiber so that the pulses were stretched to ~ 250 ps. These longer pulses were ineffective for two-photon excitation but could be used for regular STED quenching of the fluorophore via single-photon absorption. The strength of the design lies in its intrinsic synchronicity but the choice of fluorophores was limited to the selected ATTO 647 and both two-photon excitation and the STED depletion wavelength are sub-optimal if compared to a system with two independent wavelengths.

Finally, another interesting approach was recently demonstrated by Qifeng et al. [63], using a single Ti:sapphire laser. A fraction of the 532 nm continuous-wave pump laser was separated before entering the Ti:sapphire oscillator so it could be used for quenching of the fluorophore ATTO425. The remaining power of the 532 nm laser enters the Ti:sapphire laser to produce femtosecond pulses of λ=860 nm. By combining both beams before passing an acousto-optic Bragg cell to reduce the repetition rate from 80 MHz to 0.25 MHz, this approach allows femtosecond excitation of the fluorophore and 10 ns long STED pulses. As a consequence, the pulse separation time is on the same order of magnitude as the lifetime of the dark states (typical triplet-state of GFP = 4-25 µs[64]) which promises reduced photobleaching as the illumination of molecules in the triplet state increases the likelihood of photobleaching. In addition, the STED light is not illuminating the sample between the excitation pulses, although the 10 ns long STED pulses are only marginally shorter than the inter-pulse interval in traditional 80 MHz two-photon excitation (12.5 ns) and still 4-5 times longer than the typical lifetime of fluorophores (2.5 ns for GFP).

While the above mentioned reports about two-photon STED microscopy introduced the feasibility of such an instrument, one crucial point was still missing:

A microscope that combines the strengths of the previous reports in one single instrument.

I therefore defined the following objectives for the instrument to meet:

- Excitation via a tunable two-photon laser

A tunable laser allows the optimization of the excitation wavelength for the desired fluorophores. This is in contrast to the Bianchini et al. report where a compromise between the excitation and the depletion wavelength had to be made. As the signal levels of STED microscopy are, by nature of the STED process, reduced, a suboptimal excitation wavelength could be detrimental for deep tissue imaging.

- Pulsed nature of the STED laser

A pulsed STED laser dramatically reduces the average photon load on the sample. The high peak power of a laser pulse, compared to a continuous-wave laser, is sufficient to saturate the depletion of the excited state. The probability of a molecule to be in the excited state is defined by the function of the average lifetime of the molecule. For GFP, this is about 4-5 times faster than the repetition cycle of the pulsed two-photon laser. A continuous wave laser would illuminate the sample at times when the molecules have already relaxed to the ground state. Accordingly, the average power of a continuous-wave STED laser has to be increased to fulfill the saturation condition of STED at times of excitation.

The high average power of a continuous-wave laser, as utilized in the Moneron et al. and Ding et al. reports, are likely to be prohibitive for non-invasive two-photon STED microscopy.

- Upright microscope design

Living brain tissue has to be kept in a physiological solution. To prevent the solution from leaking down on the inverted microscope, the use of a coverslip is necessary. As the coverslip always creates a refractive index mismatch to brain, the objectives used on inverted designs are almost exclusively oil immersion objectives. On one hand, this has the advantage of achieving a higher numerical aperture which, in turn, comes with a very limited working distance. For thicker preparations, such as acute brain slices, the objective can then not be moved closer to the coverslip to focus through the specimen to position electrodes precisely.

An upright microscope also has the advantage over an inverted design that the choice of preparation is not limited to thin specimens that are close to a cover slip. An upright design was realised in the Ding et al. report, although they used a continuous-wave STED laser.

- Water-dipping objective

For an upright design where no coverslip is needed, a water dipping objective can be utilized. This has the advantage, over oil immersion objectives, of a reduced refractive index mismatch between the immersion medium and the tissue and hence, reduced spherical aberrations. A water dipping objective is hence the objective of choice for deep tissue imaging.

- GFP and YFP as major fluorophores/ dual color contrast capability

GFP is the oldest, and most common, genetic encoded fluorophore. Together with the yellow-shifted variant YFP, it has been introduced to a variety of mouse lines that stably express GFP in a subset of neurons. Compared to most fluorophores outside the green emission spectrum, it is also exceptionally photostable and bright. In addition, designing the system for GFP and YFP has the additional benefit of being compatible with fluorophores such as Alexa 488 that have, again, better optical properties when compared to the red-shifted organic fluorophores. Also, most calcium indicators emit efficiently in the green spectrum so that they too, at some point, could be used for STED imaging.

As both the excitation and the emission spectrum of GFP and YFP are overlapping, a single excitation and a single STED laser can be used for simultaneous excitation, quenching and detection of these fluorophores. The signal is therefore intrinsically co-aligned.

The drawback of STED microscopy in the green emission spectrum is the complexity of the STED laser.

- Live superresolution imaging deep inside acute brain slices

Acute brain slices are a very popular brain tissue preparation for measurements on cellular mechanism of learning and memory. As a consequence of the cutting procedure, the cells on the surface are damaged, which introduces the need to be able to image deeper than a few tens of microns. As the structures of interest, such as synapses, spines and axons, are often times smaller than the diffraction limit of light, fine morphological correlates of established synaptic plasticity protocols have not been able to be observed. Although far-field superresolution fluorescence microscopy does not have the resolution of electron microscopy it is compatible with live-cell imaging. In addition electron microscopy suffers from low contrast and lacks the specificity of genetic encoded fluorophore labelling. A fluorescent approach also simplifies the reconstruction of neuronal structures, which is a slow and labour intensive process in electron microscopy.

- Compatibility with electrophysiology

The use of a water-dipping objective with a long working distance gives the user greater flexibility in terms of combined imaging and electrophysiological approaches. This way, experiments addressing the nanoscale relationship between morphology and functionality can performed.

2 Results

The results section of includes a book chapter of the book “Nanoscale Imaging of Synapses” published within the Springer Neuromethods series Volume 84, Editors U. Valentin Nägerl and Antoine Triller. This chapter focuses primarily on the practical aspects of the design and construction of the two-photon excitation STED microscope.

The second part of the results section includes an original research article published in the Biophysical Journal that describes the microscope and its ability to produce superresolution images of neural structures in acute brain slices.

The last part of the results includes various applications of the microscope, demonstrating nanoscale imaging in common tissue preparations, such as dispersed cell cultures, organotypic slice cultures, acute brain slices and intact brains *in vivo*. The enhanced resolution of the microscope allowed the description of thin segments on dendrites of granule cells in the dentate gyrus and micro-varicosities on dendritic spine necks, structural features of neuronal cells that cannot be resolved by traditional two-photon microscopy. In addition, the microscope was used to investigate if the endogenous protein levels of a VGLUT1-Venus mouse and nanobodies raised against the actin cytoskeleton are suitable markers for STED.

2.1 Book chapter: Nanoscale Imaging of Synapses

Springer, 2013

Chapter 11: Two-photon STED microscopy for imaging synapses and glia in acute brain slices

Philipp Bethge and U. Valentin Nägerl

Interdisciplinary Institute for Neuroscience (IINS)
University of Bordeaux & CNRS UMR 5297, Bordeaux, France

Chapter 11

Two-Photon Excitation STED Microscopy for Imaging Synapses and Glia in Acute Brain Slices

Philipp Bethge and U. Valentin Nägerl

Abstract

STED (stimulated emission depletion) microscopy is a novel fluorescence microscopy technique that provides unprecedented access to dynamic processes of living cells with a spatial resolution well below 100 nm, even down to a few nanometers. By breaking the classical diffraction barrier of optical microscopy, it offers the chance to close the gap in spatial resolution between electron microscopy and conventional light microscopy and is attracting attention as a potential game-changing imaging technology.

The first-generation STED microscopes typically suffered from significant disadvantages over confocal or two-photon microscopy, regarding labeling, live-cell compatibility, color contrast, and depth penetration. However, due to several recent technical developments, these teething problems have been largely overcome. Similar to confocal microscopy, STED microscopy can be readily combined with a powerful array of complementary techniques, such as photo-uncaging, fluorescence recovery after photobleaching (FRAP), and patch-clamp electrophysiology, giving experimental access to a rich set of molecular, structural, and functional data.

Here, we present a primer on two-photon excitation STED microscopy, its basic principles and instrumentation requirements, providing a detailed how-to guide for the construction and operation of a STED microscope for two-color nanoscale imaging of neural morphology deep inside living brain slices.

Key words STED microscopy, Two-photon excitation microscopy, Live-cell superresolution imaging, Nanoscale morphology of neurons and glia, Acute brain slices

1 Introduction

1.1 Development of STED Microscopy

Fluorescence microscopy has become one of the dominant experimental techniques in the biosciences, because it can capture dynamic events inside living cells with exquisite sensitivity and specificity. However, the spatial resolution of conventional optical microscopy is limited by the diffraction of light to around half the wavelength of the light used in the microscope [1], which makes it difficult to investigate many subcellular compartments such as synapses or glial processes, because they can be considerably smaller than the diffraction limit (<200 nm).

U. Valentin Nägerl and Antoine Triller (eds.), *Nanoscale Imaging of Synapses: New Concepts and Opportunities*, Neuromethods, vol. 84, DOI 10.1007/978-1-4614-9179-8_11,

Fortunately, recent advances in optical microscopy techniques have broken the diffraction limit, starting the new era of superresolution fluorescence microscopy. Stimulated emission depletion (STED) microscopy was the first viable concept in this respect [2, 3], but other powerful techniques based on single-molecule imaging (PALM/STORM) were developed soon afterward [4–6].

As a result, it is now possible to perform sub-diffraction cellular imaging with a spatial resolution well below 100 nm, opening up exciting research avenues for neuroscience and synapse research in particular.

Initially, STED microscopy was used for studying the distribution of immunolabeled synaptic proteins in fixed neuronal cultures [7–9]. Subsequently, it became possible to also use it for live-cell imaging applications, e.g., revealing synaptic vesicle dynamics in nerve terminals [10] or imaging the morphology of dendritic spines in organotypic brain slices [11].

Since then, many aspects of STED microscopy have been improved, regarding setup complexity and robustness, labeling and multicolor imaging, and sample preparation and handling, substantially expanding the scope and usefulness of this novel technique for neurobiologists.

Like most other superresolution techniques, STED microscopy was initially limited to monolayers of dissociated cells or cells right on the surface of the sample. But it has now been successfully extended to thick tissue preparations, including brain slices [12] and intact brain in vivo [13], through the use of glycerol objectives equipped with a correction collar, which reduces spherical aberrations as compared with oil objectives. In addition, STED microscopy has recently been combined with two-photon excitation using long-working distance water objectives and an upright microscope design [14, 15].

These were important steps because many biological preparations, such as the popular acute brain slice preparation, require deep optical access, i.e., beyond the layer of dead cells and debris on the surface, and there needs to be enough space for inserting pipettes for electrophysiological recordings or local perfusion.

In this chapter, we will describe how STED microscopy can be used for live-cell imaging in two colors with a lateral resolution of around 50 nm. We start out by going over the basic principles of STED microscopy, before describing the technical challenges and practical solutions concerning the construction and operation of a homebuilt upright STED microscope, which is based on two-photon excitation and pulsed fluorescence quenching. We close by presenting a couple of application examples of STED imaging of the morphology of dendrites and microglia cells deep inside (~50 µm) acute brain slices.

1.2 Basic Concept of STED

The spatial resolution of a scanning fluorescence microscope is defined by the size of the focal excitation volume, termed point spread function (PSF) of the microscope. The spatial extent of the PSF therefore defines the minimal distance at which two closely spaced objects can still be resolved. Because of the diffraction of light, its size is on the order of a few 100 nm in the lateral dimension, depending on the wavelength of light (λ) and the numerical aperture (NA) of the objective, according to the Abbe formula [1]:

$$d = \frac{\lambda}{2 * NA} \tag{1}$$

The basic idea of STED microscopy is to reduce the size of the PSF and hence improve the spatial resolution of the microscope, by spatially constricting the fluorescence signal. This is accomplished by a second, red-shifted laser (the STED laser), which quenches the fluorescence by the process of stimulated emission. Because the STED laser features a doughnut-shaped intensity distribution with a deep zero in its center, the fluorescence inhibition is restricted to the edge of the PSF allowing signal light to be collected from the center. By increasing the intensity of the STED laser, the size of the central region, from where fluorescence is permitted to occur, can be made in principle arbitrarily small. As a result, the Abbe formula takes on this new form:

$$d = \frac{\lambda}{2 * NA * \sqrt{1 + I_{STED} / I_S}} \tag{2}$$

where I_{STED} denotes the incident power of the STED laser and I_s the intensity at which half of the molecules are quenched [16].

According to Eq. 2, d tends to zero as I_{STED} increases. In this way, a resolution of 5.8 nm has been achieved for samples of diamond crystals, which is about two orders of magnitude smaller than the wavelength of the excitation light [17].

The STED laser is usually tuned to the long wavelength tail end of the emission spectrum, where it does not excite the molecules, and where it can be separated well from the fluorescence signal by standard dichroic mirrors and emission filters (Fig. 1a–c).

Because the time that the molecules spent in the excited state is short (the fluorescence lifetime of fluorescent proteins and green organic dyes like Alexa 488 is a few nanoseconds), it is better to use pulsed lasers, which achieve much more efficient fluorescence quenching for a given amount of STED laser intensity.

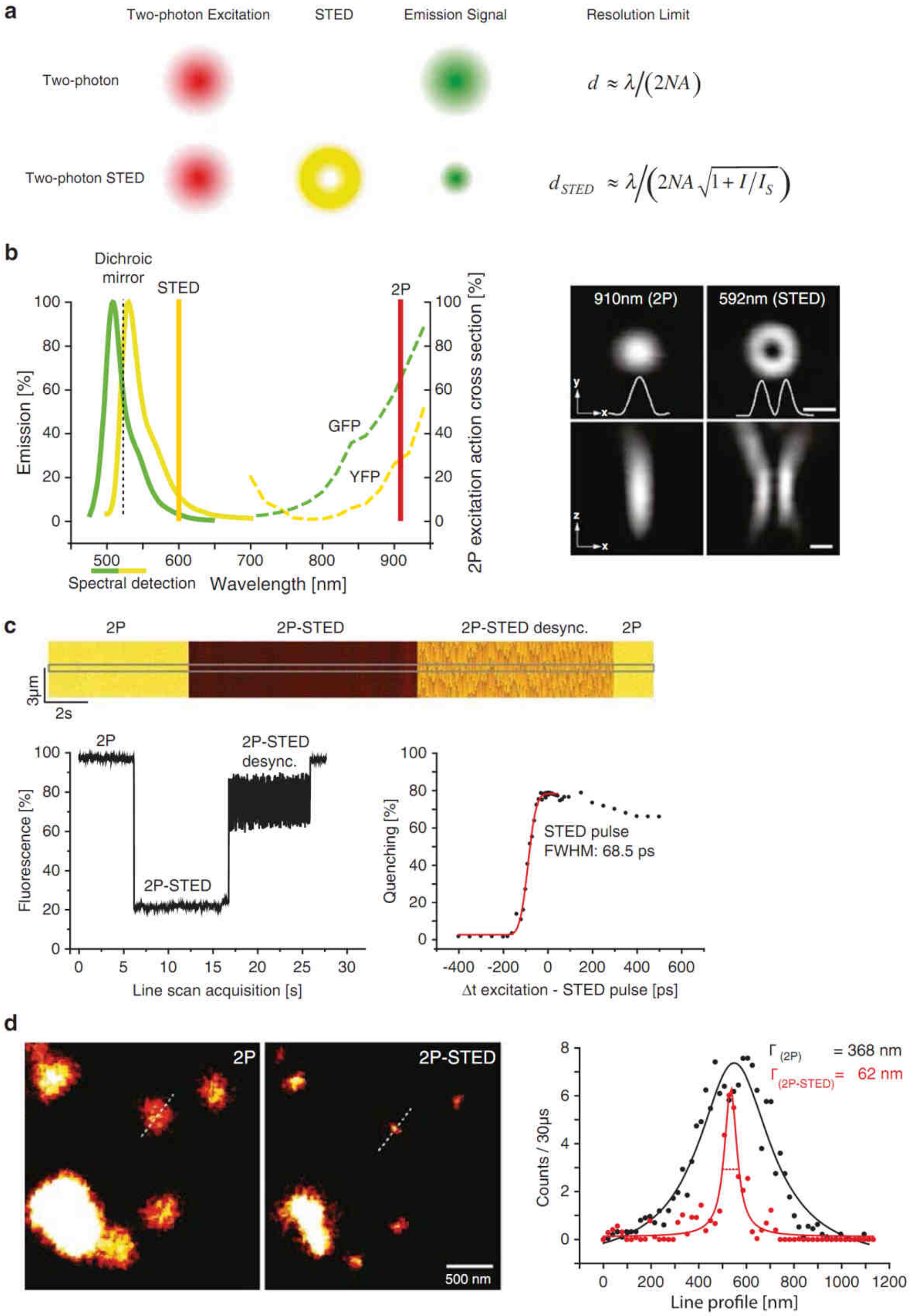

Fig. 1 Basic principle of STED microscopy. (**a**) Principle of STED microscopy. A diffraction-limited two-photon excitation spot is scanned across the sample, and its emission signal is detected. In STED microscopy,

2 Materials

2.1 Optical Components for Beam Steering

To begin with, great care must be taken to create a diffraction-limited PSF of the excitation and the STED light. To achieve this, the choice of optical components is critical, and only high-quality optical components with an optical flatness of $\lambda/10$ should be used. Because of the dependence of two-photon excitation on pulse width, care has to be taken not to stretch the pulses in time excessively while propagating through the optical components. For beam steering, dedicated two-photon mirrors (for excitation) and dielectric visible mirror (for STED light and fluorescence) are available. High-grade silver mirrors can be used when all wavelengths (two-photon, STED, and emission signal) are combined as they reflect (>98 %) over a broad range of wavelengths (375–1,000 nm) while keeping pulse dispersion to a minimum. It is helpful to use a motorized 45° flip mirror as the final mirror before the objective so that it can be flipped out of the way to allow for wide-field imaging.

In addition, various components such as lens telescopes, half-wave plates ($\lambda/2$), quarter-wave plates ($\lambda/4$), and polarizing beam splitters as well as instruments and tools for beam diagnostics and alignment such as beam profiler, power meter, spectrometer, shear plate, and oscilloscopes are essential.

2.2 Microscope Base and Objective

To minimize temperature drift and mechanical vibrations, it is important to mount all components as close as possible to the table (1 " posts). For an upright microscope, it is therefore recommended to raise the essential components via a breadboard to the height of the scan-tube lens axis (Fig. 2). The use of a modular research-grade upright microscope has the advantage that essential optical

Fig. 1 (continued) a doughnut-like quenching beam is superimposed on the excitation beam. The quenched molecules in the periphery of the STED beam do not fluoresce anymore, and, hence, the detected emission signal originates only from the center of the STED doughnut. The resolution of the STED microscope is then, in addition to Abbe's law (λ wavelength, *NA* numerical aperture), also defined by the power of the STED beam (I) and a property of the dye (I_s). (**b**) Spectral schema and reflection from gold beads for spatial alignment. As the two-photon beam is in the near-IR spectrum (910 nm), the emission signal can be detected over a broad range (<600 nm). The STED beam at 600 nm allows simultaneous quenching of GFP and YFP. The reflections form gold beads are detect with a PMT and used for spatial alignment of the excitation and the STED beam. Excitation action cross section from Warren Zipfel, Cornell University, USA (Scale bars, 500 nm). (**c**) Synchronization of two-photon and STED pulses. A line scan of a calcein solution demonstrates the quenching effect of the STED laser if excitation, and STED pulses are synchronized and optimally delayed in time. A quenching efficiency of 80 % can be achieved. Varying the relative delay between the pulses allows for direct measurement of the STED pulse width and the lifetime of the molecule. (**d**) A resolution of 62 nm can be observed on 40-nm-large fluorescent beads. This is strongly contrasted to the 368 nm measured in two-photon mode alone and illustrates a sixfold improvement in lateral resolution

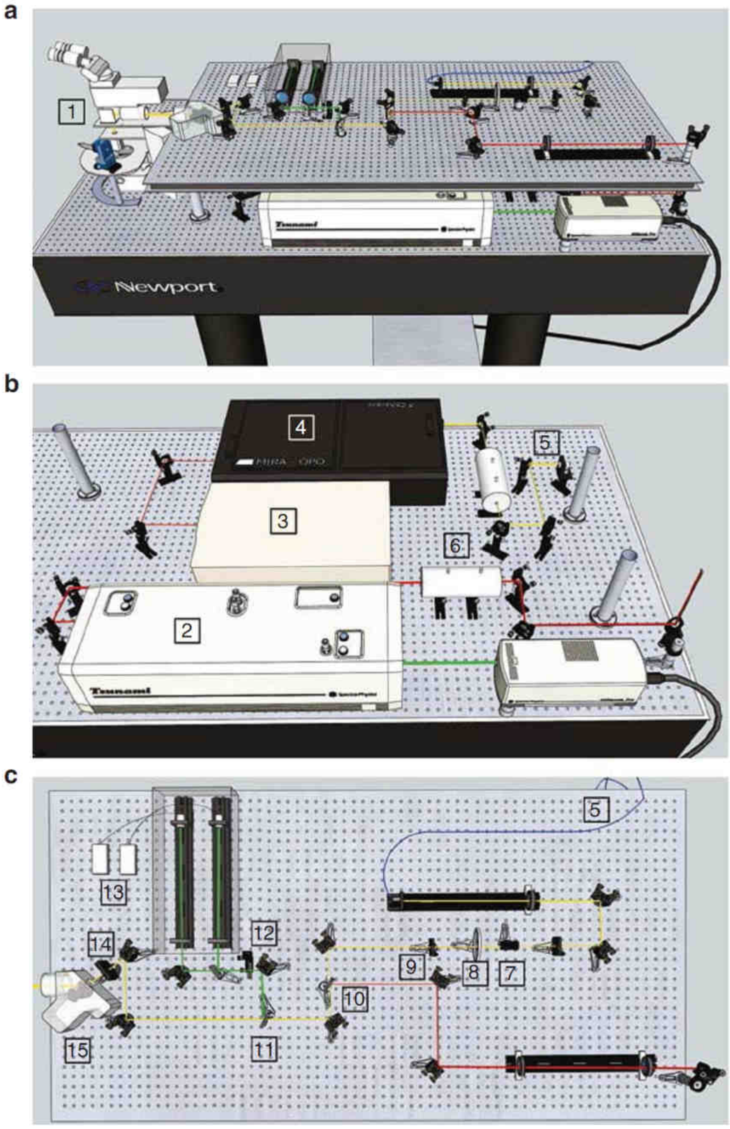

Fig. 2 Design of homebuilt two-photon excitation STED microscope. (**a**) Overview of the custom build two-photon STED microscope. (**b**) Its light sources. (**c**) The optical beam path. An upright Olympus BX51-WI is modified so that dedicated scan-tube lenses can be incorporated. The beam is deflected via a motorized flip mirror toward the piezo-actuator-controlled objective. Electrophysiological recording equipment is mounted on the motorized stage (1). The excitation laser (910 nm) originates from a Ti–Sapphire laser (Millenia/Tsunami) (2). This laser is synchronized to the STED laser, consisting of the Ti–Sapphire laser Mai Tai (3), pumping an OPO (4). The STED light is then coupled into a 20-m-long single-mode fiber (5). All laser attenuation is realized via electro-optical modulators (6). The STED laser passes a polarizing beam splitter (7), the vortex phase mask (8), and a λ/2 wave plate (9). STED and 2P lasers are combined using a dichroic mirror (10).

components are included, such as condenser, light illuminator, and phase contrast, facilitating the combination with an electrophysiology setup. Our system is developed around an Olympus BX-51WI in conjunction with a motorized sample stage (380FM, Luigs & Neumann, Reutlingen, Germany).

As opposed to conventional light microscopy, where the numerical aperture of the objective and the excitation wavelength define the spatial resolution, in STED microscopy the optical resolution also depends on the power of the STED light. Nevertheless, when combining STED microscopy with two-photon excitation, high-NA objectives have the advantage of minimizing the excitation PSF, allowing for efficient two-photon excitation. A water-dipping objective of NA 1.1, long-working distance (1.5 mm) equipped with a correction collar and high visible and near-IR transmission (Olympus LUMFI 60x, NA 1.1) can be used to this end [15].

2.3 Two-Photon Excitation Laser Source, Synchronization with the STED Laser

In principle, the light source used for STED quenching can be either continuous wave (CW) or pulsed lasers. CW lasers are easier to implement while pulsed lasers have the advantage of restricting the optical power to the time the fluorophores is excited. This greatly reduces the photon load and hence photodamage of the sample. To ensure that the STED pulses have the right timing in respect to the excitation pulses, the excitation two-photon laser needs to have the option of electronically varying the cavity length so that it can be synchronized to the STED laser. This can be achieved by phase-locked loop electronics, which are commercially available from the two-photon laser companies Spectra-Physics and Coherent (Lok-to-Clock or Synchrolock). This solution can be implemented on a Spectra-Physics Tsunami HP fs 15 W with Model 3930 Lok-to-Clock for excitation but is not compatible with the modern generation of Ti–Sapphire lasers (i.e., Mai Tai or Chameleon). A Pockels cell (Conoptics, Danbury, CT) can be used to control the laser beam power for the imaging beam path.

2.4 STED Laser and Optical Parametric Oscillator

The STED laser is an essential component of the system and should be chosen according to the emission spectrum of the desired fluorophores. For green/yellow fluorophores such as GFP and YFP, a combination of a Ti–Sapphire laser (e.g., Spectra-Physics Mai Tai HP, wavelength: 797 nm, repetition rate ~80 MHz, pulse duration

Fig. 2 (continued) Signal light is separated from the excitation and quenching lasers via a dichroic mirror (11) before passing suitable blocking and emission filters (12), focused on multimode fibers and detected via avalanche photo diodes (13). Two-photon and STED lasers are routed through a λ/4 (14) and into a beam scanner (15). 3D illustration performed with free version of Trimble SketchUp

~200 fs) pumping an optical parametric oscillator (such as OPO BASIC Ring fs RTP, APE, Berlin, Germany) is a powerful solution. This STED-OPO system provides the trigger signal for the synchronization with the two-photon laser. The incident STED laser power at the back focal plane is controlled via a dedicated Pockels cell.

2.5 STED Pulse Dispersion in Glass Rod and Polarization-Preserving Fiber

The OPO is tuned to 598 nm and delivers pulses of 200 fs duration with a repetition rate that is defined by the pump laser (~80 MHz). These pulses need to be stretched in time to allow for efficient fluorescence quenching and to avoid unintended multiphoton excitation. A 25-cm glass rod (SF6) stretches the pulses to around ~2 ps before being coupled into a 20-m-long polarization-maintaining single-mode fiber (Schäfter + Kirchhoff, Hamburg, Germany). The pre-broadening of the pulses in the glass rod protects the fiber from being damaged by the high-energy pulses and reduces spectral broadening within the fiber. A band-pass filter (593/40, AHF Analysentechnik, Tübingen, Germany) is used to spectrally clean up the light after the fiber.

2.6 Pulse Delay Generator

The synchronization of the laser pulses is realized via dedicated phase-locked loop electronics from the manufacturer of the excitation two-photon laser (Spectra-Physics, Model 3930 Lok-to-Clock). The exact pulse frequency of the lasers can be read out from fast photodiodes via a reflection of the laser beam or from the internal photodiodes. The ability to adjust the relative temporal delay between the pulses is essential for the optimization of STED quenching. The system in use allows for a temporal delay of 2 ns. Alternatively, the relative temporal delay can be optimized by changing the optical path length. As this involves the movement of optical components, beam misalignment during the delay adjustments can occur. A fast photodiode (such as 3932-LX, Spectra-Physics) under the objective can serve as a readout for the initial temporal coarse alignment.

2.7 Helical Vortex Phase Mask

The shape and the quality of the central null of the STED doughnut are essential to the performance of the microscope. A helical vortex phase plate (RPC Photonics, Rochester, NY), mounted on a *xy*-translation stage, is used for the generation of the STED doughnut. A polarizing beam splitter before the phase mask "cleans" the polarization state of the incident light so that the phase plate can create a destructive interference pattern in the center of the beam resulting in the doughnut-like intensity distribution in the focal plane. To shape the doughnut, $\lambda/2$ and $\lambda/4$ wave plates before the scanner are used to optimize both the symmetry and the central null intensity of the doughnut.

2.8 Dichroic Filters for Merging the Two Beams and Filtering Out the Emission Signal

The dichroic mirrors in use have to fulfill the $\lambda/10$ criterion and are typically dielectrically coated and 5 mm thick. We use a short-pass dichroic (F73-700UV, AHF) to combine both the STED and the two-photon beam before they pass a long-pass dichroic (580 DCXRUV, AHF) to separate the emission signal and direct it to the photo detectors (see Sect. 2.10).

2.9 Beam Scanner and Fast Nano-positioner of Microscope Objective

For live-cell applications and the combination of imaging and electrophysiology, beam scanning is preferred over stage scanning, even though the implementation is more challenging. Creating a stationary beam at the back focal plane is critical and realized via a scan and tube lens combination (FV300/U-TLUIR, Olympus, Hamburg, Germany) in conjunction with a telecentric galvo scanner (Yanus IV, TILL Photonics, Gräfelfing, Germany). On upright systems, it is helpful to define an objective height position and adjusting the stage so that a stable beam position can be achieved. Fast scanning in the *z*-dimension can be realized via a piezo-driven objective positioner (P-725, Physik Instrumente, Germany). Note that electronic noise and ground loops can interfere with the beam scanning, creating unwanted artifacts in the image.

2.10 Photodetectors

Due to the low signal count of STED images, high-quality detectors are very important. Both avalanche photo diodes (APDs) and photomultiplier tubes (PMTs) have been used on STED microscopes. APDs have the clear advantage of higher quantum efficiency and very low dark counts while the PMTs offer a higher dynamic range and larger detection area. New-generation hybrid detectors might fill this gap in the foreseeable future. Our system is equipped with two APDs (SPCM-AQR-13; PerkinElmer, Fremont, CA) to allow for two-channel spectral detection of the emission signal. A dichroic mirror (514RS, Semrock) separates the emission light in two channels. Both channels are focused via long focal length ($f=300$ mm) lenses onto multimode fibers with a 100-μm core diameter, corresponding to about 120 % of the back-projected Airy disk.

Because of the use of high-power STED and two-photon lasers, care has to be taken to efficiently shield the detectors from the excitation/STED light by suitable optical filters, such as a STED blocking filter (594S-25), a two-photon blocking filter (680SP-25), and an emission band-pass filter (520-70, all Semrock, Rochester, NY, USA). Due to the small detection area of APDs, detection has to occur in descanned mode. For imaging deeper inside the tissue, i.e., beyond the scattering length of photons (~100 μm), proximity PMT detectors (in a non-descanned arrangement) can be used, which collect scattered photons more efficiently [14].

2.11 Perfusion Recording Chamber

The recording chamber is equipped with temperature control (via the stage) and a perfusion system, designed for coverslips with a diameter of 18 mm. Due to the upright design of the system, standard electrophysiological chambers can be used.

3 Methods

3.1 General Alignment of Beams

As STED microscopy relies on the modulation of the excitation PSF by the STED beam, a precise alignment of the two beams is critical. Coarse beam path alignment is realized by sending either a green test diode laser or by using the STED laser backward, starting at the objective position. The scan mirrors need to be parked in their central position during this process. Because of the upright design, it can be difficult getting the test laser diode at the correct position. One solution is to couple the diode laser into a single-mode optical fiber and mounting the collimated output instead of the objective. Additional problems arise from the poor performance of Ti–Sapphire laser mirrors in the visible spectrum and the dichroic mirrors that transmit/reflect the laser diode light to only one beam path. Either a red diode laser can be used or the backward alignment is terminated at two pinholes that serve as reference to the forward beam alignment. The STED beam path is well aligned when the test laser can be coupled through the single-mode fiber that usually carries the STED light. The detectors are coarsely aligned via the test diode laser (taking care not to send the test laser directly onto the detectors) or by exciting a dye solution (i.e., calcein) and aligning the resulting fluorescence that can be seen on a white card in darkness. Two-photon lasers are class 4 lasers and require the use of eye safety equipment.

3.2 Making Doughnuts

The shape and quality of the STED doughnut is essential to the performance of the microscope. Using gold nanospheres (diameter = 150 nm; BB International, Cardiff, UK) and a pellicle beam splitter (Thorlabs, Maisons-Laffitte, France), the reflection of the gold beads can be directed toward a detector, such as a PMT. Here, one should consider the detection range of the PMT since both the ~600-nm STED light and the near-infrared two-photon light have to be detected. The reflection from the gold bead is a good indicator for the alignment of the beams, verifying that both beams are superimposed and the reflections do not show a tilt in one or the other direction. When the helical phase plate is correctly placed, it produces a clearly visible dark spot in the profile of the laser beam at some distance from the phase plate. This dark spot has to be centered in the beam but can be slightly adjusted with the *xy*-translation stage. By adjusting both the $\lambda/2$ and $\lambda/4$ wave plates before the scanner, the symmetry of the doughnut and the quality of the central null can be optimized while observing the gold bead reflections. Rotating the $\lambda/2$ will allow the user to optimize the symmetry while rotation of the $\lambda/4$ has a strong effect on the central minimum. A slight tilt of the $\lambda/4$ might yield a slightly better central minimum. The STED beam is optimally modulated when the doughnut is symmetric and the central null approaches 1 % of the intensity of the rim. Alignment of the beams in the *z*-direction can be achieved by slightly de-collimating one or both beams.

3.3 Evaluating Microscope Performance

As STED microcopy crucially relies on the ability of the STED laser to quench the fluorescence of the excited molecules, testing the quenching efficiency is one of the first steps in determining the performance of the microscope. Only when the beams are aligned in space and time, can a quenching efficiency of ~80 % be expected. The resolution of the STED system is most commonly assessed by imaging sub-diffraction-sized fluorescent beads that emit in the desired wavelength. Note that 40-nm-sized beads are hard to image with a two-photon microscope because they bleach very rapidly so that for the daily routine, 170-nm beads will provide enough information to evaluate the correct alignment.

3.4 Acute Brain Slices

All acute brain preparations can be used on this system, among them the widely used acute hippocampal slice preparation. Protocols on the preparation of acute brain slices can be found elsewhere [18]. We use a standard NaCl-based artificial cerebrospinal fluid (ACSF) solution consisting of (in mM) 124 NaCl, 3 KCl, 26 $NaHCO_3$, 1.25 NaH_2PO_4, 10 glucose, 2 $CaCl_2$, 1 $MgCl_2$, and 0.6 Trolox (pH 7.4, osmolarity ~305 mOsm/L). Trolox is an antioxidant that protects cells from free radicals produced by fluorescence excitation. Because of the relatively low signal of STED images, we selected strongly fluorescent mice lines, such as the Thy1-YFP and the CX3CR1-GFP.

3.5 Imaging Living Brain Slices

The quality of the slices is essential for obtaining high standard images. Lower-quality slices have a thick layer of damaged cells on the surface, which typically introduces high background fluorescence. To obtain images from healthy cells, the objective height should be adjusted to at least ~20 μm below the surface. Strong background fluorescence induced by the STED beam alone can be observed in non-healthy slices, indicating the need to terminate the experiment. Laser intensities, image size, pixel size, and dwell time have to be adapted for the desired resolution, fluorophore, and depth. Two-photon laser intensities are typically in the range of 10–25 mW and slightly higher for STED (20–40 mW), measured at the back focal plane of the objective. Pixel size should adhere to the Nyquist sampling theory and is usually between 20 and 40 nm for STED microscopes.

3.6 Two-Color STED Imaging by Linear Unmixing of GFP and YFP

Our dual-color schema relies on the fact that the emission of two highly overlapping spectra can be separated by their relative contributions on the two installed detectors [19]. Post-hoc analysis of a known cell population allows the calculation of the so-called mixing matrix, which in turn can be used for the identification of the fluorescence contributions for each pixel. The same STED wavelength can be used for quenching GFP and YFP, with the advantage that both colors are acquired simultaneously and are inherently co-aligned [19].

3.7 Image Analysis

As STED imaging employs raster scanning, no post-hoc analysis is necessary to produce a superresolved image as in other superresolution techniques (such as SIM, PALM, STORM). Measurement of fine structures, such as spine necks, should be performed on raw data of single frames instead of z-projections. This decreases the risk of including pixel from structures above and below the structure of interest. Using averaged intensity profiles from 2 to 3 pixel wide lines reduces the contribution of outlier values. Quantification of the line profiles should report the full width at half maximum (FWHM) done either on plotted observed values or by using nonlinear fit functions (such as Lorentzian or Gaussian functions). Two-photon STED image profiles seem to be fitted better with Lorentzian than with Gaussian functions. For presentation purposes only, images can be de-noised by using median or Gaussian filters.

4 Notes

1. Using a “hands-off” Ti–Sapphire laser (such as the Mai Tai or the Chameleon series) as the pump laser for the OPO has the advantage of minimizing alignment procedures during start-up of the system.
2. Since the resolution of STED microscopy depends on the intensity of the STED light, lower NA objectives can be used as well. We have acquired superresolved images using a water-dipping objective of NA 1.0 (data not shown).
3. It is critical not to introduce any translation of the beam while operating a laser power attenuation device such as a motorized, rotating $\lambda/2$ wave plate, placed in front of a polarizing beam splitter as this results in small, nevertheless detrimental horizontal translation of the STED beam. An electro-optical modulator, placed in front of the STED fiber, works very well. In addition, it is recommended to send only the necessary STED power through the fiber to minimize damage on the fiber core. Therefore, the power should be adjusted before the fiber input coupling.

5 Application Examples

5.1 Alignment and Performance

Figure 1b shows an image created by the reflection of gold beads on a PMT. The correct alignment of the two beams in xy- and z-direction and the quality of the STED doughnut can be verified with this test. In Fig. 1c, the fluorescence intensity of a calcein solution is strongly reduced by an optimally aligned and synchronized STED beam. If synchronization is disabled, despite the same optical power reaching the sample, quenching of the STED beam is strongly diminished. By varying the relative delay of the synchronized pulses, an estimate of both the width of the STED as well as the lifetime of the molecule can be obtained as proposed previously [20]. Using 40-nm-sized fluorescent beads, the optical resolution of the microscope can be assessed (Fig. 1d).

5.2 Life Cell Imaging

All presented images originate from acute brain slices. Figure 3 shows several examples of two-photon STED images recorded in either CA1 of the hippocampus or in the cortex. In Fig. 1a, the line profile across a spine neck illustrates that with conventional two-photon microscopy, this spine would be described as having a very large spine neck. Using STED microscopy, it becomes apparent that the structure consists of two, closely spaced, spines necks. The individual spine heads are located along above the plane presented and hardly visible because of the diffraction-limited z-resolution. In Fig. 3b, we have acquired several z-stacks along the primary dendrite of a cortical neuron, starting at the soma and spanning a total length of 540 μm. The higher magnification images B1 and B2 illustrate the sub-diffraction sized spine necks along the dendrite. In Fig. 3c, two examples of microglial processes (green) in close proximity to superresolved spines are presented. The left image (maximum intensity projection) was created by assigning each channel a color (green and red) and simply merging the two colors. The right image (single frame) was linearly unmixed, using an ImageJ Plugin ("Spectral Unmixing" by Walter J). For Fig. 4, we acquired the same z-stack every 2 min and present maximum intensity projections of the same structure. A modest change over time is detectable on most structures while obvious photodamage is not observed. Again, spine neck diameters, well below the diffraction limit of two-photon microscopy can be measured.

Acknowledgments

This work was supported by a Ph.D. fellowship from the 7th Framework Program (FP7) Marie Curie ITN "SyMBaD" to P. Bethge and grants from the Regional Council of Aquitaine (CRA), Inserm, ANR, and HFSP to U. V. Nägerl. We thank the members of the lab for comments on the manuscript.

218 Philipp Bethge and U. Valentin Nägerl

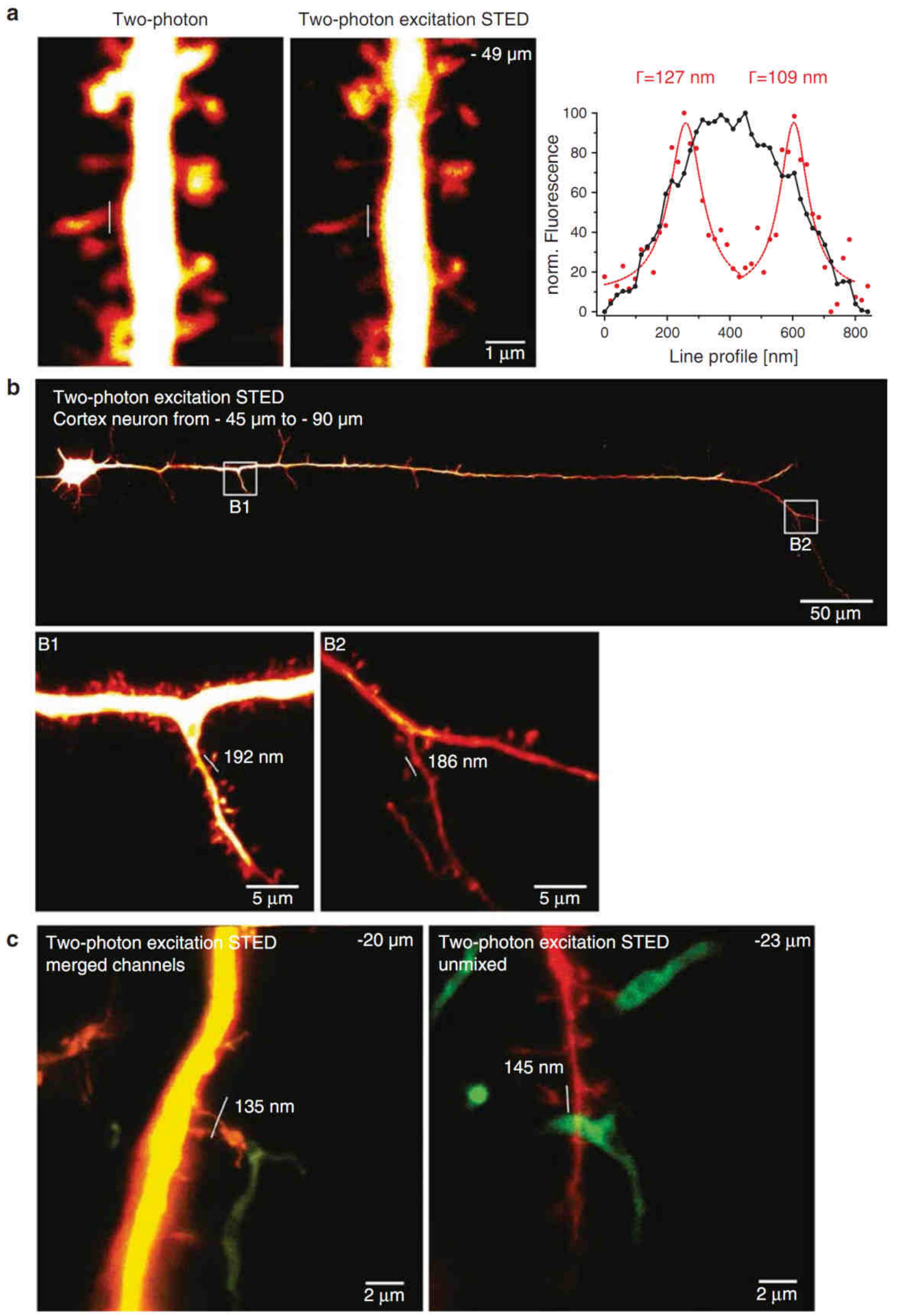

Fig. 3 Nanoscale imaging of neural morphology in acute brain slices. (**a**) Comparison of a hippocampal CA1 dendritic segment recorded from an acute brain slice in two-photon versus two-photon STED mode.

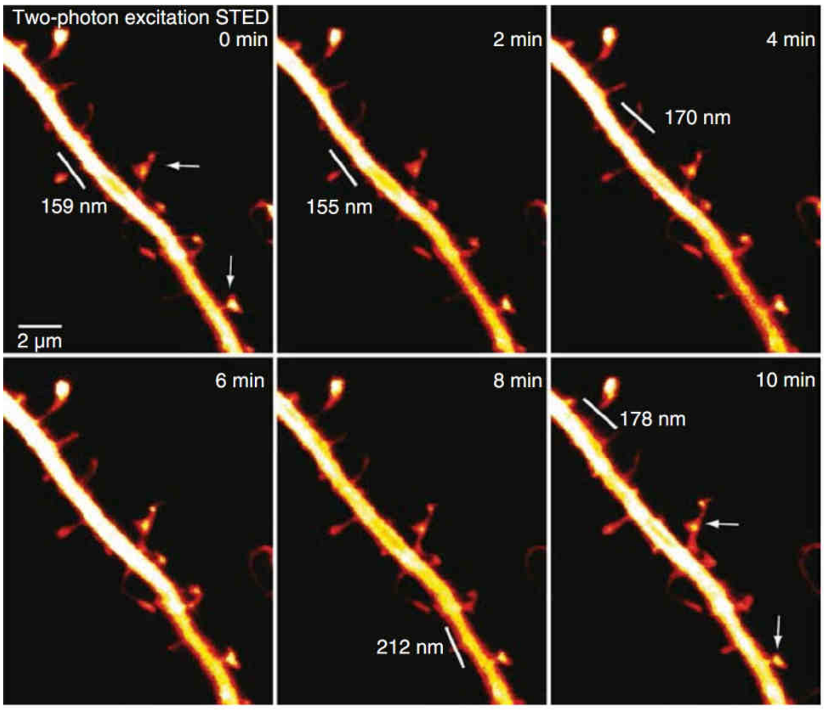

Fig. 4 Time-lapse two-photon excitation STED imaging of neuronal morphology. Crop of median filtered maximum intensity projections of 6 stacks, recorded every 2 min at a depth of – 23 µm in cortex (6 frames per stack, $\Delta z = 500$ nm, every frame is 20 µm × 20 µm, 512 × 512 pixel, pixel size 40 nm, 30 µs pixel dwell time). Several spine necks with diameters well below the diffraction limit of classic two-photon microscopy are visible. The *arrows* point at structures, which are morphologically dynamic under physiological conditions, in the absence of signs of photodamage (such as blebbing)

Fig. 3 (continued) The line profile of the spine neck (indicated by *white line*) clearly resolves two structures when imaged in STED mode. The FWHM of the individual spine neck indicates diameters of 115 nm and 132 nm, respectively. The images were recorded 49 µm below the surface of the slice. Presented is a crop of a median filtered image from a *z*-stack, each 512 × 512 pixel, 20-nm pixel size, 30-µs pixel dwell time. (**b**) Reconstruction of a cortical Layer 4/5 neuron from an acute brain slice. The main dendrite of a single neuron was reconstructed by recording 17 stacks, each 1,024 × 1,024 pixel, 40-nm pixel size, 15 frames per stack ($\Delta z = 500$ nm), 30-µs pixel dwell time. The dendrite was located 45–90 µm below the surface of the slice. Maximum intensity projections were arranged using an ImageJ Plugin ("2D stitching" by Preibisch, S). *White boxes* B1 and B2 indicate position of the higher magnification images below. Spine neck widths of 192 and 186 nm can be observed. Using this approach, neuronal morphology and fine structures can be studied in a high-throughput manner. (**c**) Microglial processes in close proximity to neuronal spines of cortical neurons. Both merging of channels (*left*) and linear unmixing (*right*) allow sufficient contrast to distinguish cell types. Spine neck widths of 135 and 145 nm can be measured in single planes

References

1. Abbe E (1873) Beiträge zur Theorie des Mikroskops und der mikroskopischen Wahrnehmung. Archiv für Mikroskopische Anatomie 9(1):413–418
2. Hell SW, Wichmann J (1994) Breaking the diffraction resolution limit by stimulated emission: stimulated-emission-depletion fluorescence microscopy. Opt Lett 19(11):780–782. doi:12352 [pii]
3. Hell SW (2007) Far-field optical nanoscopy. Science 316(5828):1153–1158
4. Rust MJ, Bates M, Zhuang X (2006) Sub-diffraction-limit imaging by stochastic optical reconstruction microscopy (STORM). Nat Methods 3(10):793–795
5. Hess ST, Girirajan TP, Mason MD (2006) Ultra-high resolution imaging by fluorescence photoactivation localization microscopy. Biophys J 91(11):4258–4272
6. Betzig E, Patterson GH, Sougrat R, Lindwasser OW, Olenych S, Bonifacino JS, Davidson MW, Lippincott-Schwartz J, Hess HF (2006) Imaging intracellular fluorescent proteins at nanometer resolution. Science 313(5793): 1642–1645. doi:1127344 [pii] 10.1126/science.1127344
7. Willig KI, Rizzoli SO, Westphal V, Jahn R, Hell SW (2006) STED microscopy reveals that synaptotagmin remains clustered after synaptic vesicle exocytosis. Nature 440(7086): 935–939. doi:nature04592 [pii] 10.1038/nature04592
8. Sieber JJ, Willig KI, Kutzner C, Gerding-Reimers C, Harke B, Donnert G, Rammner B, Eggeling C, Hell SW, Grubmuller H, Lang T (2007) Anatomy and dynamics of a supramolecular membrane protein cluster. Science 317(5841):1072–1076. doi:317/5841/1072 [pii] 10.1126/science.1141727
9. Kittel RJ, Wichmann C, Rasse TM, Fouquet W, Schmidt M, Schmid A, Wagh DA, Pawlu C, Kellner RR, Willig KI, Hell SW, Buchner E, Heckmann M, Sigrist SJ (2006) Bruchpilot promotes active zone assembly, Ca^{2+} channel clustering, and vesicle release. Science 312(5776): 1051–1054. doi:1126308 [pii] 10.1126/science.1126308
10. Westphal V, Rizzoli SO, Lauterbach MA, Kamin D, Jahn R, Hell SW (2008) Video-rate far-field optical nanoscopy dissects synaptic vesicle movement. Science 320(5873):246–249. doi:1154228 [pii] 10.1126/science.1154228
11. Nägerl UV, Willig KI, Hein B, Hell SW, Bonhoeffer T (2008) Live-cell imaging of dendritic spines by STED microscopy. Proc Natl Acad Sci U S A 105(48):18982–18987. doi:0810028105 [pii] 10.1073/pnas.0810028105
12. Urban NT, Willig KI, Hell SW, Nägerl UV (2011) STED nanoscopy of actin dynamics in synapses deep inside living brain slices. Biophys J 101(5):1277–1284. doi:S0006-3495(11)00885-X [pii] 10.1016/j.bpj.2011.07.027
13. Berning S, Willig KI, Steffens H, Dibaj P, Hell SW (2012) Nanoscopy in a living mouse brain. Science 335(6068):551. doi:335/6068/551 [pii] 10.1126/science.1215369
14. Takasaki KT, Ding JB, Sabatini BL (2013) Live-cell superresolution imaging by pulsed STED two-photon excitation microscopy. Biophys J 104(4):770–777. doi:S0006-3495(13)00073-8 [pii] 10.1016/j.bpj.2012.12.053
15. Bethge P, Chereau R, Avignone E, Marsicano G, Nägerl UV (2013) Two-Photon excitation STED microscopy in two Colors in acute brain slices. Biophys J 104(4):778–785. doi:S0006-3495(13)00074-X [pii] 10.1016/j.bpj.2012.12.054
16. Harke B, Keller J, Ullal CK, Westphal V, Schonle A, Hell SW (2008) Resolution scaling in STED microscopy. Opt Express 16(6):4154–4162. doi:154873 [pii]
17. Rittweger E, Han KY, Irvine SE, Eggeling C, Hell SW (2009) STED microscopy reveals crystal colour centres with nanometric resolution. Nat Photonics 3:144–147 (2009) Published online: 22 February 2009, doi:10.1038/nphoton.2009.2
18. Madison DV, Edson EB (2001) Preparation of hippocampal brain slices. Curr Protoc Neurosci/editorial board, Jacqueline N Crawley et al. Chapter 6:Unit 6 4. doi:10.1002/0471142301.ns0604s00
19. Tønnesen J, Nadrigny F, Willig KI, Wedlich-Soldner R, Nägerl UV (2011) Two-color STED microscopy of living synapses using a single laser-beam pair. Biophys J 101(10):2545–2552. doi:S0006-3495(11)01200-8 [pii] 10.1016/j.bpj.2011.10.011
20. Schrader M, Meinecke F, Bahlmann K, Kroug M, Cremer C, Soini E, Hell SW (1995) Monitoring the excited state of a fluorophore in a microscope by stimulated emission. Bioimaging 3:147–153

2.2 Biophysical Journal Article: Two-Photon Excitation STED Microscopy in Two Colors in Acute Brain Slices

Biophysical Journal 2013
104(4):778-85, 2013

778 Biophysical Journal Volume 104 February 2013 778–785

Two-Photon Excitation STED Microscopy in Two Colors in Acute Brain Slices

Philipp Bethge,[†‡] Ronan Chéreau,[†‡] Elena Avignone,[†‡] Giovanni Marsicano,[§] and U. Valentin Nägerl[†‡*]
[†]Interdisciplinary Institute for Neuroscience, Université de Bordeaux, Bordeaux, France; [‡]UMR 5297, Centre National de la Recherche Scientifique, Bordeaux, France; and [§]Université de Bordeaux, INSERM U862 NeuroCentre Magendie, Bordeaux, France

ABSTRACT Many cellular structures and organelles are too small to be properly resolved by conventional light microscopy. This is particularly true for dendritic spines and glial processes, which are very small, dynamic, and embedded in dense tissue, making it difficult to image them under realistic experimental conditions. Two-photon microscopy is currently the method of choice for imaging in thick living tissue preparations, both in acute brain slices and in vivo. However, the spatial resolution of a two-photon microscope, which is limited to ~350 nm by the diffraction of light, is not sufficient for resolving many important details of neural morphology, such as the width of spine necks or thin glial processes. Recently developed superresolution approaches, such as stimulated emission depletion microscopy, have set new standards of optical resolution in imaging living tissue. However, the important goal of superresolution imaging with significant subdiffraction resolution has not yet been accomplished in acute brain slices. To overcome this limitation, we have developed a new microscope based on two-photon excitation and pulsed stimulated emission depletion microscopy, which provides unprecedented spatial resolution and excellent experimental access in acute brain slices using a long-working distance objective. The new microscope improves on the spatial resolution of a regular two-photon microscope by a factor of four to six, and it is compatible with time-lapse and simultaneous two-color superresolution imaging in living cells. We demonstrate the potential of this nanoscopy approach for brain slice physiology by imaging the morphology of dendritic spines and microglial cells well below the surface of acute brain slices.

INTRODUCTION

Most neurons in the mammalian brain are studded with hundreds to thousands of dendritic spines (1). Spines are tiny specializations of the postsynaptic membrane that are packed with receptors, ion channels, and other signaling complexes and mediate fast excitatory synaptic transmission in the brain. Their structural dynamics are thought to be critical for brain development and experience-dependent synaptic plasticity throughout life (2).

Thus, quantitative measurements of the structure and function of spines have been a primary endeavor in neuroscience research for a long time. Getting reasonable optical access is a huge challenge, because they are embedded in dense brain tissue and are oftentimes smaller than what can be resolved by diffraction-limited light microscopy, including two-photon (2P) microscopy.

Moreover, recent studies indicate that spines also interact directly with surrounding glial cells, like astrocytes and microglia (3,4), which extend extremely thin processes. Hence, to study how spines operate and interact with their partners in a complex and dynamic environment, it is essential to image several cell types at the same time with sufficient spatial resolution below the diffraction limit. In recent years, several big steps have been made in developing methods to make this possible.

Starting a new era in optical microscopy, stimulated emission depletion (STED) microscopy (5–7) has allowed for nanoscale imaging of dynamic events in living tissue, imaging synaptic vesicles (8) and spine morphology (9). Furthermore, several strategies were recently developed for multicolor STED imaging (10–13).

Most STED studies to date have been done in culture systems using oil objectives (e.g., Westphal et al. (8), Nägerl et al. (9), and Willig et al. (14)), but the experimental preparation of choice for synaptic physiologists is acute brain slices. To record healthy cells in acute brain slices, it is necessary to image a few tens of microns deep in the tissue, which cannot be done with oil objectives. Although glycerol objectives can substantially extend optical penetration without compromising spatial resolution (15), they are not compatible with acute brain slices, which call for an upright microscope design and water-immersion objectives with long working distances to accommodate electrophysiological recording electrodes.

The combination of 2P excitation and STED (2P-STED) microscopy (16,17) opened new perspectives for superresolution imaging in deep tissue. However, the use of continuous wave (CW) STED lasers limited the spatial resolution to 250 nm in living tissue (16).

Submitted August 27, 2012, and accepted for publication December 11, 2012.

*Correspondence: valentin.nagerl@u-bordeaux2.fr

Editor: Paul Wiseman.

0006-3495/13/02/0778/8 $2.00

http://dx.doi.org/10.1016/j.bpj.2012.12.054

In this study, our goal was to overcome these limitations and to achieve true subdiffraction imaging in acute brain slices a few cell layers below the tissue surface, which corresponds to a depth usually targeted in patch-clamp electrophysiology experiments. To this end, we developed a new 2P-STED microscope incorporating a pulsed STED laser, a long-working distance water objective and spectral detection for two-color imaging.

We characterize the 2P-STED microscope and illustrate its potential by imaging dendritic spines in acute brain slices. The spatial resolution in the focal plane of the new microscope is four to six times better than that of a regular, diffraction-limited 2P microscope. Furthermore, we show that the microscope is compatible with time-lapse and two-color superresolution imaging, using transgenic mice in which neurons and microglia are labeled with yellow (YFP) and green fluorescent protein (GFP), respectively.

MATERIALS AND METHODS

Lasers

A femtosecond mode-locked Ti:Sapphire laser (Mai Tai, Spectra-Physics, Darmstadt, Germany) operating at ~80 MHz and a wavelength of 797 nm was used in combination with an optical parametric oscillator (OPO BASIC Ring fs, APE, Berlin, Germany) to produce pulses at a wavelength of 592 nm (STED laser). The pulses of originally ~200-fs duration were stretched to >68 ps by passing them through a 25-cm dispersive glass rod (high-refractive-index flint glass) and a 20-m-long polarization-preserving fiber (Schäfter & Kirchhoff, Hamburg, Germany). A reflection from the STED laser was used to synchronize a second mode-locked ultrafast Ti:Sapphire laser (Tsunami, Spectra-Physics) operating at 910 nm for 2P excitation (2P laser).

Synchronization and fine pulse delay (<2 ns) was performed via phase-locked loop electronics (3930, Lok-to-Clock, Spectra-Physics), while the coarse delay was set by varying the length of the BNC cable, using a fast photodiode (3932-LX, Spectra-Physics) placed below the microscope objective for readout.

Laser intensities were controlled via dedicated electro-optical modulators (Conoptics, Danbury, CT) for the 2P and STED laser beams. The time-averaged power at the back focal plane (BFP) of the objective was between 15 and 25 mW for the 2P light and between 20 and 40 mW for the STED light, depending on imaging depth and sample brightness.

Microscope setup

The microscope was built around a standard commercial research microscope (BX51WI, Olympus, Hamburg, Germany) using scan and tube lenses from the microscope manufacturer. The telecentric scanner (Yanus IV, TILL Photonics, Gräfelfing, Germany) was placed so that both scan axes are projected into the BFP of the objective, ensuring that the 2P and STED laser beams stay stationary at the BFP during scanning.

A water-immersion objective with a long working distance (1.5 mm) and equipped with a correction collar was used for all experiments (60X LUMFI, 1.1 NA, Olympus). The correction collar was adjusted to optimize the STED doughnut using gold nanospheres (diameter = 150 nm; BBInternational, Cardiff, United Kingdom) and slightly readjusted for particular imaging depths, using the 2P fluorescence signal as readout. The *z*-position of the objective was controlled via a piezo actuator (P-721 PIFOC, PI Physik Instrumente, Karlsruhe, Germany). Signal detection and peripheral hardware were controlled by the Imspector scanning software (18) via data acquisition cards (6259 M, 2090A, National Instruments, Austin, TX).

A polymeric phase plate (RPC Photonics, Rochester, NY) was used to create the STED doughnut and a bandpass filter (593/40, AHF Analysentechnik, Tübingen, Germany) was used to spectrally clean up the STED laser beam. The 2P and STED laser beams were combined using a dichroic mirror (F73-700UV, AHF) before the scanner.

The fluorescence signal was detected in descanned mode and separated from the excitation and STED light by a longpass dichroic (580 DCXRUV, AHF). The detectors were protected from the 2P and STED light by suitable blocking and emission filters (680SP-25, 594S-25, 520-70, Semrock, Rochester, NY). The signal was spectrally divided into two channels by a dichroic mirror (514RS, Semrock) before being focused onto multimode fibers (100-μm core diameter, which corresponds to 120% of the back-projected Airy disk), terminating on avalanche photodiodes (SPCM-AQR-13-FC, PerkinElmer, Waltham, MA).

Microscope alignment

For spatial alignment of the 2P and STED lasers and quality control of the doughnut (Fig. 1 *D*), a pellicle beam splitter (Thorlabs, Maisons-Laffitte, France) was flipped into the beam path so that the reflection from gold nanospheres could be detected by a photomultiplier tube (MD963, PerkinElmer). A piezo-controlled motorized mirror (AG-M100N, Newport, Beaune la Rolande, France) and a telescope were used to align the doughnut on the excitation spot in all three dimensions. Doughnut quality (shape and null) was optimized via achromatic $\lambda/2$ and $\lambda/4$ wave plates (Qioptiq, Paris, France). Optical resolution (Fig. 2 *D*) was assessed using fluorescent nanospheres (Fluo Spheres, yellow-green, diameter = 0.04 μm, Invitrogen).

Animals and labeling

Two transgenic mouse lines (C57BL/6 background) were used: Thy1$^{eYFP/eYFP}$ mice that express YFP in a subpopulation of principal neurons in the hippocampus as well as in layer 4/5 of cortex, and CX3CR1$^{eGFP/eGFP}$ mice that express GFP in microglial cells (Jackson Labs, Bar Harbor, ME). In experiments where only neurons were imaged, heterozygous Thy1$^{+/eYFP}$ mice were used. In experiments where neurons and microglia were imaged, mice obtained from the crossbreeding of the two mouse lines were used (CX3CR1$^{+/eGFP}$; Thy1$^{+/eYFP}$). All experiments were carried out in accordance with the National Code of Ethics on Animal Experimentation (Carte Nationale d'éthique sur l'expérimentation animale; Ministère de l'enseignement et de la recherche, Ministère de l'agriculture et de la pêche) and approved by the Committee of Ethics of Bordeaux (No. 3306001).

Acute brain slices

Animals 21–40 days old were killed by cervical dislocation, and their brains were quickly removed and placed in ice-cold sucrose-based artificial cerebrospinal fluid (ACSF) containing (in mM) 210 sucrose, 10 glucose, 2 KCl, 26 NaHCO$_3$, 1.25 NaH$_2$PO$_4$, 0.1 CaCl$_2$, and 6 MgCl (pH 7.4, osmolarity ~320 mOsm/L), which was bubbled with carbogen (95% O$_2$/5% CO$_2$). Sagittal 350-μm-thick slices were cut using a vibratome (VT1200, Leica, Mannheim, Germany) and transferred to a heated (32°C) holding chamber with NaCl-based ACSF bubbled with carbogen, which consisted of (in mM) 124 NaCl, 3 KCl, 26 NaHCO$_3$, 1.25 NaH$_2$PO$_4$, 10 glucose, 2 CaCl$_2$, 1 MgCl, and 0.6 Trolox (pH 7.4, osmolarity ~305 mOsm/L) for 1 h. These slices were subsequently maintained at room temperature for a maximum of 4 h. For the imaging experiments, the slices were transferred to a submerged recording chamber, where they were continuously perfused (2.1 mL/min) with ACSF at room temperature.

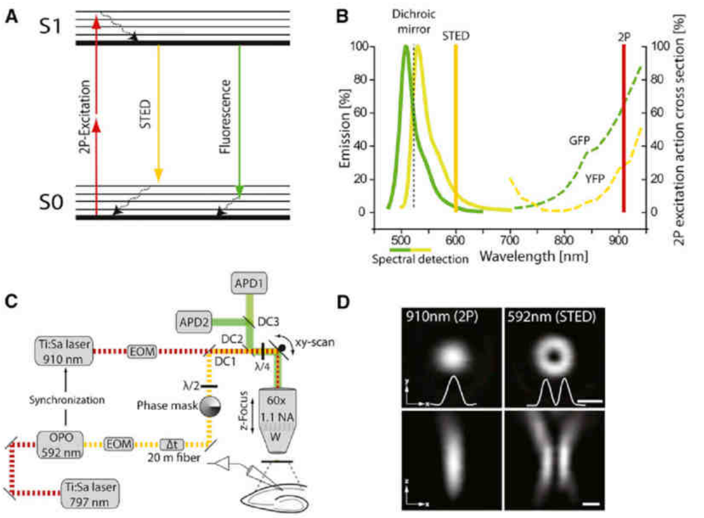

FIGURE 1 Principle and design of a pulsed 2P-STED microscope. (*A*) Simplified Jablonski diagram of the molecular excitation states in 2P-STED microscopy. The molecule is excited to the excited state (S1) by two-photon absorption and returns from there to the ground state (S0) by the emission of fluorescence. The incidence of STED light quenches the fluorescence and returns the molecule to S0 before fluorescence can occur (*curved dashed arrows* show internal conversion). (*B*) Two-photon excitation action cross section and emission spectra for GFP and YFP (Warren Zipfel, Cornell University, Ithaca, NY). Simultaneous quenching of GFP and YFP by a single laser beam of 592 nm is possible because of the highly overlapping tails of the emission spectra. Two-photon excitation is performed at 910 nm. The emission signal is spectrally separated and detected in two channels. (*C*) Schematic of beam path. The femtosecond pulsed Ti:Sa laser used for 2P excitation is routed through a beam scanner into an upright microscope and synchronized with the STED laser (Ti:Sa/optical parametric oscillator (OPO)). Femtosecond pulses emitted from the Ti:Sa/OPO are broadened by a 20-m-long polarization-preserving single-mode fiber. The doughnut is formed by a helical phase mask. A long-working distance, water-immersion objective is used. It is equipped with a correction ring to correct spherical aberrations due to mismatches in refractive index at the lens-sample interface. λ/2, half-wave plate; λ/4, quarter-wave plate; DC, dichroic mirrors, NA, numerical aperture; Δt, pulse broadening fiber; xy-scan, scanner for *x* and *y* dimension; APD, avalanche photodiode; EOM = electro-optical modulator. (*D*) Reflections of the laser beams from gold particles used for visualization and spatial alignment of the excitation and STED beams. The laser beams are routed through a pellicle beam splitter so that the reflections can be detected by a photomultiplier tube. This allows for the characterization of the excitation and STED beams and illustrates the doughnut-like intensity distribution of the STED laser. Scale bar, 500 nm.

Image acquisition and analysis

All images were acquired with a pixel size of 19.5 nm (512 × 512 pixels, 10 μm × 10 μm, except see Fig. 4 *B3*, which is 1024 × 1024 pixels, 40 μm × 40 μm, with a pixel size of 39 nm) and a pixel dwell time of 30 μs, which corresponds to about 8 s acquisition time for a 10 μm × 10 μm field of view. Imaging depth into the slice was determined by the piezo z-focus, the fluorescence signal on top of the slice defining the zero z-position. Image analysis was done on raw data using ImageJ. Images presented in the figures were filtered by a 1-pixel Gaussian filter to reduce noise. To quantify and compare the line profiles from 2P and 2P-STED images, we used the Lorentzian function:

$$y = y_0 + \frac{2A}{\pi}\frac{\Gamma}{4(x-x_c)^2+\Gamma^2},$$

where y_0 and A are constants, x_c is the center, and Γ is the width of the curve.

Two-color images are shown merged with and without linear unmixing using a plugin for ImageJ as described before (12). Unless stated otherwise, single frames from a z-stack (Δz typically 400 nm) are shown.

Statistics

Data are expressed as the mean ± SE. A two-tailed unpaired t-test was used to compare spine neck widths (Γ) measured for 2P and 2P-STED in the CA1, cortex, and for the two groups pooled. Multiple comparisons were post-hoc Bonferroni-corrected. A nonparametric Kolmogorov-Smirnov test was additionally used for groups containing <17 data points, confirming the results of the parametric t-test. Data from 12 mice were included in this study. Tests marked with (***) in Fig. 3 *C* are significant, with $p < 10^{-12}$.

RESULTS

Construction of the microscope

We built a 2P-STED microscope for two-color subdiffraction imaging in brain slices using a long-working distance, water-immersion objective as outlined in Fig. 1, *A–C*. For coupling the lasers into the microscope, we first checked the reflection of the 2P and STED light using gold beads (Fig. 1 *D*). We optimized the symmetry and central minimum of the STED doughnut by adjusting a λ/4 wave plate placed in front of the scanner. The intensity of the STED beam at the doughnut center was <1% of the intensity measured at the rim of the doughnut (Fig. 1 *D*), which was indistinguishable from background noise.

Performance of the microscope

Because we used pulsed lasers for 2P excitation and the STED effect, the lasers had to be synchronized and their pulses had to arrive at the sample with an optimal delay to achieve efficient quenching of the 2P fluorescence by the STED laser. Indeed, quenching depended on how much of the STED pulse overlaps with the time that the molecules spent in the excited state after 2P excitation. Fig. 2, *A* and *B*, illustrates that 80% quenching efficiency in a sea of dye fluorescence (~1 mM calcein) can be achieved.

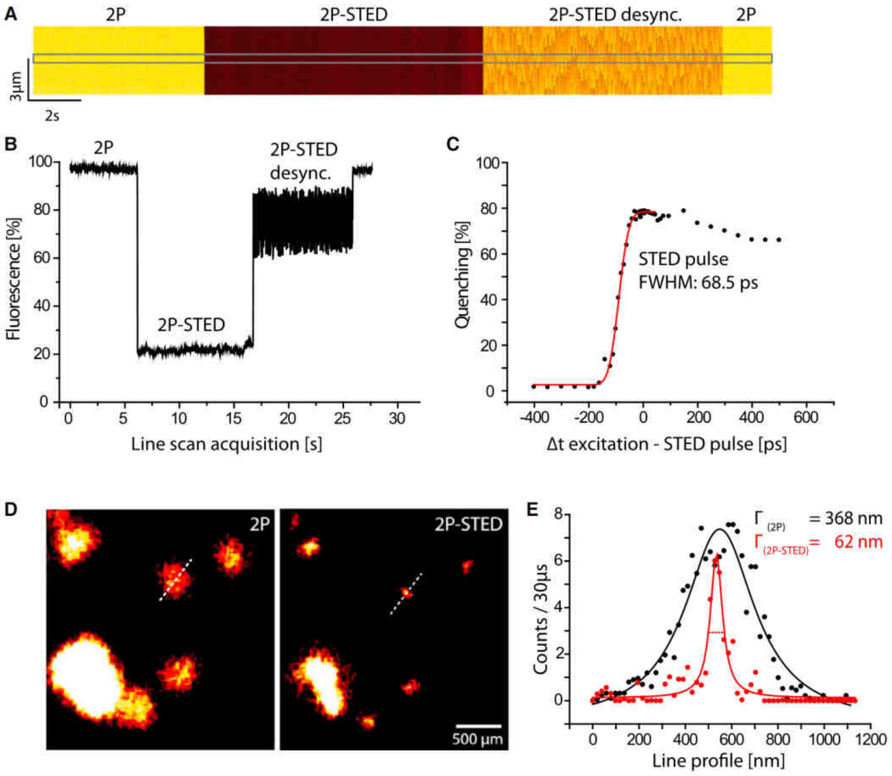

FIGURE 2 Fluorescence quenching and spatial resolution in 2P-STED microscopy. (*A*) Line scans in a fluorescent solution excited by the 2P laser. The signal is quenched by a pulsed STED laser. Desynchronization strongly attenuates this effect. (*B*) Quantification of the signal intensity along the rectangle indicated in *A*. Desynchronization greatly reduces quenching efficiency and increases variability. Fluorescence quenching is 80% when the 2P and STED pulses are synchronized and aligned in space and time. (*C*) 2P-STED requires a precise relative temporal delay of the synchronized laser pulses, which can be used to probe the duration of the STED laser pulse. Quenching efficiency is plotted as a function of the relative delay between the excitation and the STED beam. Fitting the data with a Gaussian error function (*red*) indicates a STED pulse duration (FWHM) of at least 68.5 ps. (*D*) 2P and 2P-STED images of fluorescent beads (diameter = 40 nm). A clear resolution enhancement can be observed in 2P-STED relative to 2P excitation. (*E*) Quantification of the line indicated in *D* and fitting with a Lorentzian function returns a width of 62 nm for 2P-STED (*red*) as compared with 368 nm for 2P (*black*).

Conversely, when the synchronization is turned off, the quenching effect is strongly diminished (Fig. 2 *B*).

Fig. 2 *C* illustrates the fluorescence quenching efficiency by the STED laser as a function of the relative delay between the laser pulses, where zero refers to the optimal delay. Changing the relative delay between pulses results in a rapid increase of quenching to a maximum of 80% before it decreases again gradually. Whereas the rising phase of the curve should be mostly defined by the duration of the STED pulse, the decay should be defined by the lifetime of the fluorophore (19).

Based on the rising phase (fitting a Gaussian error function), we estimated the duration of the STED pulse to be at least 68.5 ps (full width at half maximum (FWHM)) using a 20-m-long polarization-preserving optical fiber, which is consistent with pulse durations of 200–300 ps reported for 120-m-long optical fibers (20).

To check the performance of the 2P-STED microscope, we imaged subdiffraction-sized fluorescent beads (diameter = 40 nm) and determined the point-spread functions (PSFs) for the 2P and 2P-STED case (Fig. 2 *D*). The width of the PSF is an important indicator of the spatial resolution of the microscope. Using a Lorentzian function to fit line profiles drawn through the centers of individual beads, we measured a PSF width of 368 nm for the 2P case, which corresponds well to the expected spatial resolution of a diffraction-limited 2P microscope given the wavelength of the 2P light (910 nm) and the NA of the objective (1.1) (21). Imaging the same bead in STED mode, the PSF width was 62 nm, which corresponds to about a sixfold

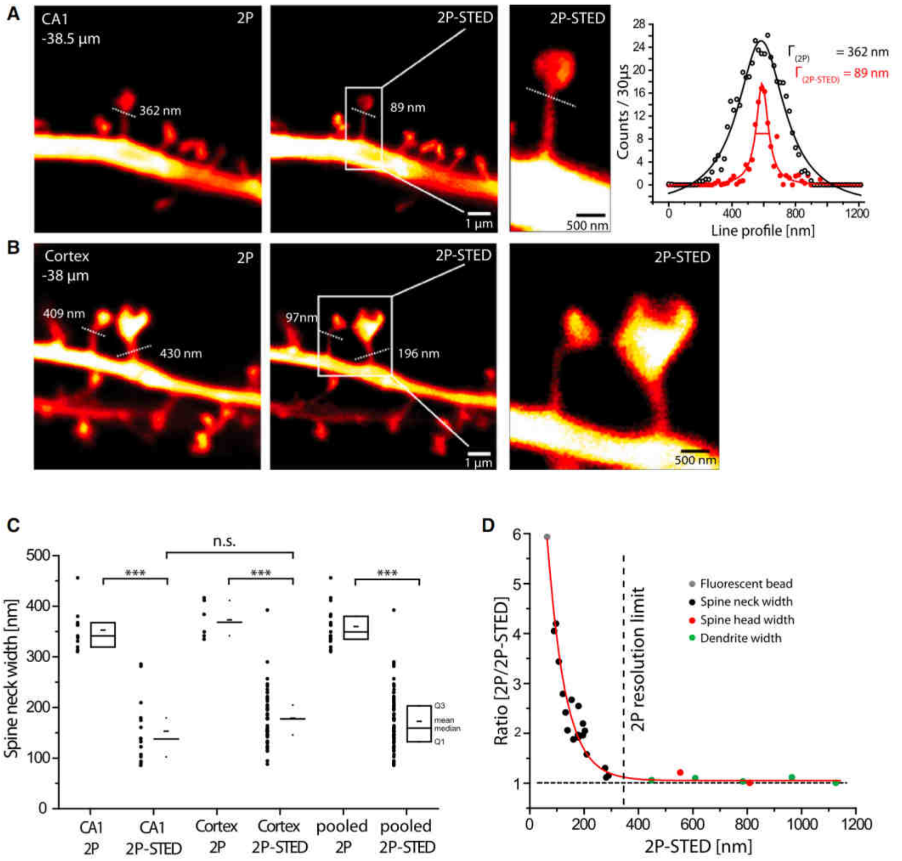

FIGURE 3 2P-STED microscopy in acute brain slices. (*A* and *B*) 2P and 2P-STED images of dendritic spines of YFP-labeled CA1 (*A*) and cortical (*B*) pyramidal neurons in acute slices from Thy1-YFP transgenic mice. Spine necks appear much thinner in 2P-STED compared to 2P images. Dotted lines indicate spine neck widths (Lorentzian fit of the line profile of the line indicated). The difference in width between 2P imaging ($\Gamma = 362$ nm) and 2P-STED imaging ($\Gamma = 89$ nm) demonstrates the resolution enhancement by 2P-STED. (*C*) Quantification of spine neck widths of CA1 and cortex imaged in 2P and 2P-STED modes. No difference between CA1 and cortex was detected. 2P imaging clearly overestimates spine neck widths when compared to the 2P-STED mode. Boxplot indicate Q1 and Q3 (first and third quartile), median and mean (large and small lines, respectively). (*D*) Plot of 2P-STED measurements versus the ratio between 2P and 2P-STED of the same object. As expected, the ratio is 1 when the structures are larger than the resolution limit of 2P microscopy (~350 nm), but it increases steeply when the structures are <350 nm in size.

improvement in spatial resolution over the 2P case. The peak photon count at the center of the bead was only slightly (~10%) reduced (Fig. 2 *E*), confirming that the STED light intensity in the center of the doughnut is very low.

Subdiffraction imaging of dendritic spines in acute slices

To check whether we could achieve subdiffraction spatial resolution in acute brain slices, we imaged dendritic spines from transgenic mice expressing YFP as a volume label in a subset of hippocampal and cortical neurons. We compared the performance of the 2P-STED with the 2P microscope by imaging spines with or without the STED light. In general, the spine necks appeared substantially wider without the STED light, whereas the appearance of the 2P-STED images was much crisper (Fig. 3 and Fig. S1).

To confirm this impression quantitatively, we measured line profiles across the spine necks and fitted them with a Lorentzian function as above. In the example illustrated in Fig. 3 *A* (a spine of a hippocampal CA1 pyramidal neuron imaged at a depth of 38.5 μm), the neck appeared to be 362 nm wide in the 2P image but only 89 nm in the 2P-STED image. This fourfold difference demonstrates that

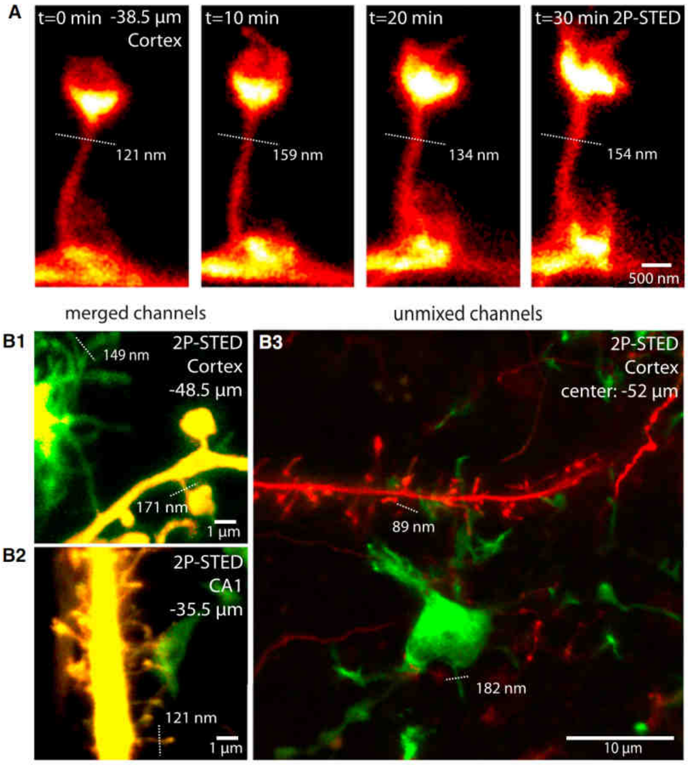

FIGURE 4 Time-lapse and dual-color 2P-STED imaging. (*A*) Time-lapse images of a cortical spine acquired at 38.5 μm below the tissue surface. Individual time points are average projections of two frames based on multiple sections (5 frames/stack, four stacks, $\Delta z = 400$ nm). (*B*) Two-color 2P-STED imaging of neurons and microglia. Transgenic mice (CX3CR1$^{+/eGFP}$; Thy1$^{+/eYFP}$) express YFP in neurons and GFP in microglia. Superresolved microglial processes ($\Gamma = 149$ nm) can be observed (*B1*), as can a microglial process contacting dendritic spines (*B2*) and a maximum-intensity projection of a z-stack of images (19 frames, 40 × 40 μm, from -49.5 to -56.5 μm, $\Delta z = 368$ nm) in the cortex (*B3*). The high magnification images (*B1* and *B2*) are merges of both color channels (*green* (GFP) and *yellow* (YFP)); the overview image (*B3*) is linearly unmixed, effectively separating both channels (*green* (GFP) and *red* (YFP)). Dotted lines indicate spine neck widths (Γ, Lorentzian fit of raw data).

the STED approach can be used to achieve a substantial gain in spatial resolution, well below the surface of living brain tissue, using a long-working distance water-immersion objective. It is important to note that the peak signal intensity in 2P-STED mode was only reduced by ~30% compared with the 2P signal (Fig. 3 *A*), suggesting that the minimum of the STED doughnut was fairly intact at this imaging depth.

We also imaged spines from layer 4/5 of cortical pyramidal neurons, imaged in the molecular layer of visual and parietal cortices at about the same depth (Fig. 3 *B*). Similar to spines of hippocampal neurons, the spine necks of cortical neurons appear much thinner in 2P-STED than in 2P images ($\Gamma = 97$ nm for 2P-STED vs. $\Gamma = 409$ nm for 2P). The differences between 2P and 2P-STED imaging were clear-cut and highly significant ($p < 0.0001$, Fig. 3 *C*). We did not detect any significant differences in width between spine necks in hippocampus and cortex, irrespective of whether 2P or 2P-STED was used ($\Gamma_{2P\ CA1} = 352 \pm 12$ nm, $n = 11$; $\Gamma_{2P\text{-}STED\ CA1} = 153 \pm 17$ nm, $n = 15$; $\Gamma_{2P\ Cortex} = 372 \pm 15$, $n = 6$; $\Gamma_{2P\text{-}STED\ Cortex} = 178 \pm 8$ nm, $n = 49$) (Fig. 3 *C*).

Taken together, 2P-STED yields substantially better resolved images of dendritic spines compared to 2P microscopy, well below the surface of acute brain slices. To illustrate the gain in resolution quantitatively, we plotted the ratio of 2P to 2P-STED measurements as a function of the widths of assorted structures measured by 2P-STED (Fig. 3 *D*). This ratio equals 1 for structures larger than the 2P diffraction limit, but increases sharply for structures below it.

Time-lapse imaging

Next, we addressed the potential issue of phototoxicity and bleaching during 2P-STED imaging. To this end, we repeatedly (20 times) imaged the same stretch of dendrite for 30 min ($\Delta t = 10$ min) and looked for signs of photodamage such as blebbing. Our experiments demonstrate that it is possible to repeatedly acquire superresolved images with our 2P-STED microscope without obvious photodamage (Fig. 4 *A*). However, to avoid or reduce deleterious effects, which are a general concern in fluorescence microscopy, it was important to optimize the imaging parameters (e.g., laser powers, pixel dwell times, image sizes, etc.), which are linked to several factors, including slice quality, sample brightness, and imaging depth.

Two-color imaging

Finally, we performed two-color 2P-STED imaging using an approach we recently developed for STED microscopy, which is based on a single laser pair for fluorescence excitation and STED quenching (12). To this end, we modified the microscope by adding a dichroic mirror and a second detection channel for spectral detection. To illustrate the potential of using these techniques in combination, we imaged brain slices from transgenic mice in which neurons and microglia are fluorescently labeled with YFP and GFP, respectively. The images in Fig. 4 *B* demonstrate the ability of the new approach to acquire superresolved images of volume-labeled dendritic spines and microglial processes well below the surface of acute brain slices. Although spectral detection already provides for reasonable color contrast (Fig. 4, *B1* and *B2*), linear unmixing of the fluorescence channels can improve color separation substantially (Fig. 4 *B3*).

DISCUSSION

We present a novel kind of microscope for two-color superresolution imaging of neural morphology well below the surface of acute brain slices using YFP and GFP as volume labels. It is based on 2P excitation and pulsed STED microscopy and hence reconciles many powerful features, such as subdiffraction spatial resolution, two-color imaging, optical sectioning, depth penetration, the use of living samples, and the possibility of combining it with electrophysiological approaches.

We employed a long-working distance water-immersion objective with an NA of 1.1, which is relatively low compared to the glycerol- and oil-immersion objectives (1.3 and 1.4, respectively) generally used in STED microscopy (9,14,15,22). Using spine necks to estimate our resolution, the spatial resolution at an imaging depth of ~40–50 μm is likely to be around 60-70 nm, considering that spine necks are finite in size (>50 nm, as indicated by electron microscopy (23)) and thus do not mimic point sources of light.

STED microscopy, which was initially used in neurobiology to acquire superresolved images of protein distributions inside cells by immunohistochemistry (14,24), has recently been extended to live-cell imaging of dendritic spine morphology (9,16), greatly facilitating investigation of the structure and function of synapses, which is a major research topic in neuroscience.

Most previous studies have used high-NA oil or glycerol objectives with short working distances, which is incompatible with acute brain slices, because this preparation requires water-immersion objectives with long working distances and an upright microscope design. Acute brain slices are the preparation of choice for most synaptic physiologists because of the experimental access they provide for pharmacological and electrophysiological experiments.

Initially, STED microscopy was based on a confocal design and single-photon excitation, but recently the use of 2P excitation has been reported. The first two studies demonstrated the principle of 2P-STED using CW lasers for the STED beam (16,17), which are easier to implement than pulsed lasers. However, as the CW laser is much less efficient at quenching fluorescence than the pulsed laser, much more laser power (>10-fold) is needed to achieve a comparable gain in spatial resolution, which is usually prohibitive for living tissue. As a consequence, 2P-STED microscopy in living tissue has been limited to >250 nm in spatial resolution. Subsequent studies have used pulsed STED lasers in conjunction with 2P excitation (25,26), but those studies used inverted microscopes with oil objectives on fixed samples.

Here, we demonstrate 2P-STED time-lapse imaging in two colors in acute brain slices with a four- to sixfold improvement in spatial resolution over the 2P case. The STED laser intensities required to achieve the gain in resolution were substantially less than those reported previously (16,26), which is important for reducing phototoxicity and bleaching.

We speculate that the quality of the doughnut, which featured a very low minimum at its center, and the efficiency of quenching GFP and YFP with short laser pulses afforded the use of relatively modest STED laser powers.

Illustrating the potential of the new 2P-STED approach, we imaged dendritic spines in acute brain slices and measured superresolved spine necks at a few tens of microns below the tissue surface. The spine-neck widths of pyramidal neurons in the CA1 region of the hippocampus and cortex correspond well to those reported by electron microscopy (23,27), in our previous work (9), and by other recent superresolution approaches (28,29), and they are much thinner than is indicated by confocal measurements. For this reason, spine necks are thought to represent a diffusion barrier for signaling molecules, allowing for biophysical compartmentalization of synapses (15,30–33). Moreover, the sizes of the microglial processes we have observed are comparable with those of STED images in perfusion-fixed brain-tissue sections (data not shown).

Interestingly, the ability to measure the level of STED quenching as a function of the delay between the laser pulses provides a straightforward way to estimate the duration of the STED laser pulse, which otherwise requires special equipment. Likewise, fluorescence quenching by the STED laser can also be used to estimate the fluorescence lifetime of the fluorophores, as suggested previously (19), which is normally done using time-correlated single-photon counting instrumentation (34).

In summary, we have developed a new 2P-STED microscope that can be assembled using all commercial components and demonstrated its potential for investigating synapses and glial cells with unprecedented spatial resolution in acute brain slices using genetically encoded fluorophores.

SUPPORTING MATERIAL

Fig. S1 is available at http://www.biophysj.org/biophysj/supplemental/S0006-3495(13)00074-X.

This work was supported by a Ph.D. fellowship from the 7th Framework Program (FP7) Marie Curie ITN SyMBaD to P.B. (cosupervised by G.M. and U.V.N.), and grants from the Regional Council of Aquitaine (CRA), Inserm, the French National Research Agency (ANR), and the Human Frontier Science Program, to U.V.N.

We thank S. Berning for discussions on the design of the microscope and S. W. Hell for providing optomechanical components (both affiliated with the Max Planck Institute for Biophysical Chemistry, Göttingen, Germany). We thank members of the lab (M.O. Lenz, A. Panatier, and J. Tonnesen) and L. S. Wijetunge (University of Edinburgh, Edinburgh, Scotland) for discussions and comments on the manuscript and J. Angibaud for technical support.

REFERENCES

1. Ramón y Cajal, S. 1995. Histology of the nervous system of man and vertebrates. Oxford University Press, New York.
2. Holtmaat, A., and K. Svoboda. 2009. Experience-dependent structural synaptic plasticity in the mammalian brain. *Nat. Rev. Neurosci.* 10:647–658.
3. Araque, A., G. Carmignoto, and P. G. Haydon. 2001. Dynamic signaling between astrocytes and neurons. *Annu. Rev. Physiol.* 63:795–813.
4. Tremblay, M. E., B. Stevens, …, A. Nimmerjahn. 2011. The role of microglia in the healthy brain. *J. Neurosci.* 31:16064–16069.
5. Hell, S. W. 2007. Far-field optical nanoscopy. *Science.* 316:1153–1158.
6. Hell, S. W., and J. Wichmann. 1994. Breaking the diffraction resolution limit by stimulated emission: stimulated-emission-depletion fluorescence microscopy. *Opt. Lett.* 19:780–782.
7. Klar, T. A., S. Jakobs, …, S. W. Hell. 2000. Fluorescence microscopy with diffraction resolution barrier broken by stimulated emission. *Proc. Natl. Acad. Sci. USA.* 97:8206–8210.
8. Westphal, V., S. O. Rizzoli, …, S. W. Hell. 2008. Video-rate far-field optical nanoscopy dissects synaptic vesicle movement. *Science.* 320:246–249.
9. Nägerl, U. V., K. I. Willig, …, T. Bonhoeffer. 2008. Live-cell imaging of dendritic spines by STED microscopy. *Proc. Natl. Acad. Sci. USA.* 105:18982–18987.
10. Bückers, J., D. Wildanger, …, S. W. Hell. 2011. Simultaneous multi-lifetime multi-color STED imaging for colocalization analyses. *Opt. Express.* 19:3130–3143.
11. Pellett, P. A., X. Sun, …, J. Bewersdorf. 2011. Two-color STED microscopy in living cells. *Biomed. Opt. Express.* 2:2364–2371.
12. Tønnesen, J., F. Nadrigny, …, U. V. Nägerl. 2011. Two-color STED microscopy of living synapses using a single laser-beam pair. *Biophys. J.* 101:2545–2552.
13. Willig, K. I., A. C. Stiel, …, S. W. Hell. 2011. Dual-label STED nanoscopy of living cells using photochromism. *Nano Lett.* 11:3970–3973.
14. Willig, K. I., S. O. Rizzoli, …, S. W. Hell. 2006. STED microscopy reveals that synaptotagmin remains clustered after synaptic vesicle exocytosis. *Nature.* 440:935–939.
15. Urban, N. T., K. I. Willig, …, U. V. Nägerl. 2011. STED nanoscopy of actin dynamics in synapses deep inside living brain slices. *Biophys. J.* 101:1277–1284.
16. Ding, J. B., K. T. Takasaki, and B. L. Sabatini. 2009. Supraresolution imaging in brain slices using stimulated-emission depletion two-photon laser scanning microscopy. *Neuron.* 63:429–437.
17. Moneron, G., and S. W. Hell. 2009. Two-photon excitation STED microscopy. *Opt. Express.* 17:14567–14573.
18. Imspector. www.max-planck-innovation.de/de/industrie/technologieangebote/software/.
19. Schrader, M., F. Meinecke, …, S. W. Hell. 1995. Monitoring the excited state of a fluorophore in a microscope by stimulated emission. *Bioimaging.* 3:147–153.
20. Eggeling, C., C. Ringemann, …, S. W. Hell. 2009. Direct observation of the nanoscale dynamics of membrane lipids in a living cell. *Nature.* 457:1159–1162.
21. Zipfel, W. R., R. M. Williams, and W. W. Webb. 2003. Nonlinear magic: multiphoton microscopy in the biosciences. *Nat. Biotechnol.* 21:1369–1377.
22. Berning, S., K. I. Willig, …, S. W. Hell. 2012. Nanoscopy in a living mouse brain. *Science.* 335:551.
23. Harris, K. M., F. E. Jensen, and B. Tsao. 1992. Three-dimensional structure of dendritic spines and synapses in rat hippocampus (CA1) at postnatal day 15 and adult ages: implications for the maturation of synaptic physiology and long-term potentiation. *J. Neurosci.* 12:2685–2705.
24. Sieber, J. J., K. I. Willig, …, T. Lang. 2007. Anatomy and dynamics of a supramolecular membrane protein cluster. *Science.* 317:1072–1076.
25. Li, Q., S. S. Wu, and K. C. Chou. 2009. Subdiffraction-limit two-photon fluorescence microscopy for GFP-tagged cell imaging. *Biophys. J.* 97:3224–3228.
26. Bianchini, P., B. Harke, …, A. Diaspro. 2012. Single-wavelength two-photon excitation-stimulated emission depletion (SW2PE-STED) superresolution imaging. *Proc. Natl. Acad. Sci. USA.* 109:6390–6393.
27. Arellano, J. I., R. Benavides-Piccione, …, R. Yuste. 2007. Ultrastructure of dendritic spines: correlation between synaptic and spine morphologies. *Front Neurosci.* 1:131–143.
28. Testa, I., N. T. Urban, …, S. W. Hell. 2012. Nanoscopy of living brain slices with low light levels. *Neuron.* 75:992–1000.
29. Izeddin, I., C. G. Specht, …, M. Dahan. 2011. Super-resolution dynamic imaging of dendritic spines using a low-affinity photoconvertible actin probe. *PLoS ONE.* 6:e15611.
30. Svoboda, K., D. W. Tank, and W. Denk. 1996. Direct measurement of coupling between dendritic spines and shafts. *Science.* 272:716–719.
31. Grunditz, A., N. Holbro, …, T. G. Oertner. 2008. Spine neck plasticity controls postsynaptic calcium signals through electrical compartmentalization. *J. Neurosci.* 28:13457–13466.
32. Bloodgood, B. L., and B. L. Sabatini. 2005. Neuronal activity regulates diffusion across the neck of dendritic spines. *Science.* 310:866–869.
33. Araya, R., J. Jiang, …, R. Yuste. 2006. The spine neck filters membrane potentials. *Proc. Natl. Acad. Sci. USA.* 103:17961–17966.
34. Lakowicz, J. R. 2006. Principles of Fluorescence Spectroscopy. Springer, New York.

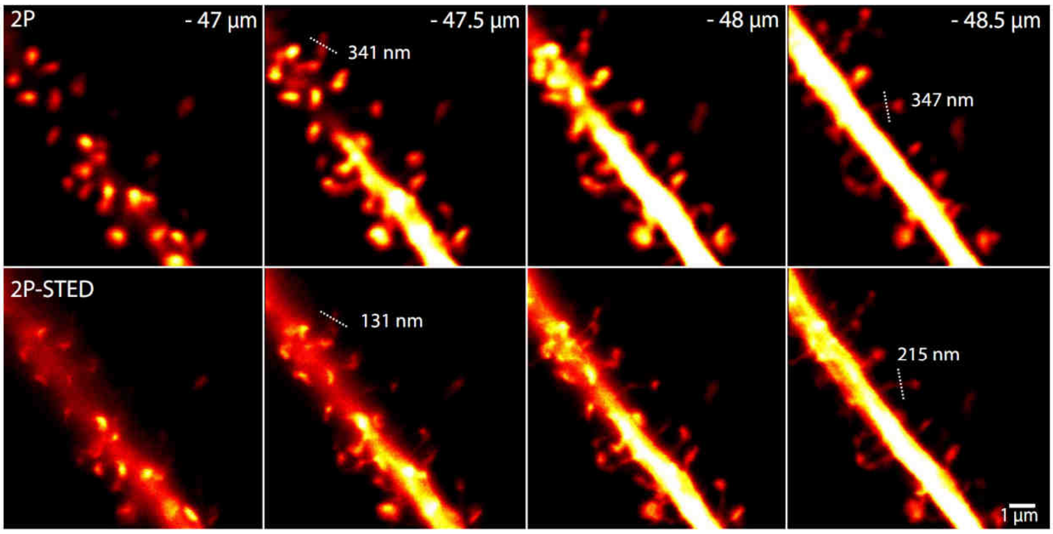

Supplementary 1: 2P-STED imaging of dendrites and spines deep inside acute hippocampal slices

Comparison of 2P and 2P-STED imaging of dendrites in CA1 region of acute hippocampal slice up to 48.5µm below the surface. Small inserts denote measured spine neck widths (Γ, Lorentzian fit of raw data).

2.3 Further applications of 2PE-STED microscopy for neuroscience

The previous two chapters illustrate the potential of the microscope for superresolution imaging deep inside acute brain slices with a resolution of around 70 nm at penetration depths of up to 90 µm. While these examples illustrate the achievement of the goals defined in the introduction, the versatile nature of the instrument allows many different biological specimens to be studied. In the present chapter I therefore will give examples of other biological preparations and applications.

2.3.1 Dissociated hippocampal cell culture

The most popular preparation of neurons for molecular and biochemical neuroscience are dispersed hippocampal or cortical cultures. They are routinely used in laboratories around the world because they can readily be transfected with plasmids carrying a gene of interest. Since they are flat and grow directly on coverslips, they are optically very accessible. These cultured neurons can also be accessed with patch pipettes for electrophysiological recordings and grown in large numbers for biochemical assays. Once cultured, these cells make extensive connections with their neighbours, which facilitate the recording from pairs of neurons but holds the danger of the network becoming overexcited and hence epileptic. Also, they are notoriously vulnerable.

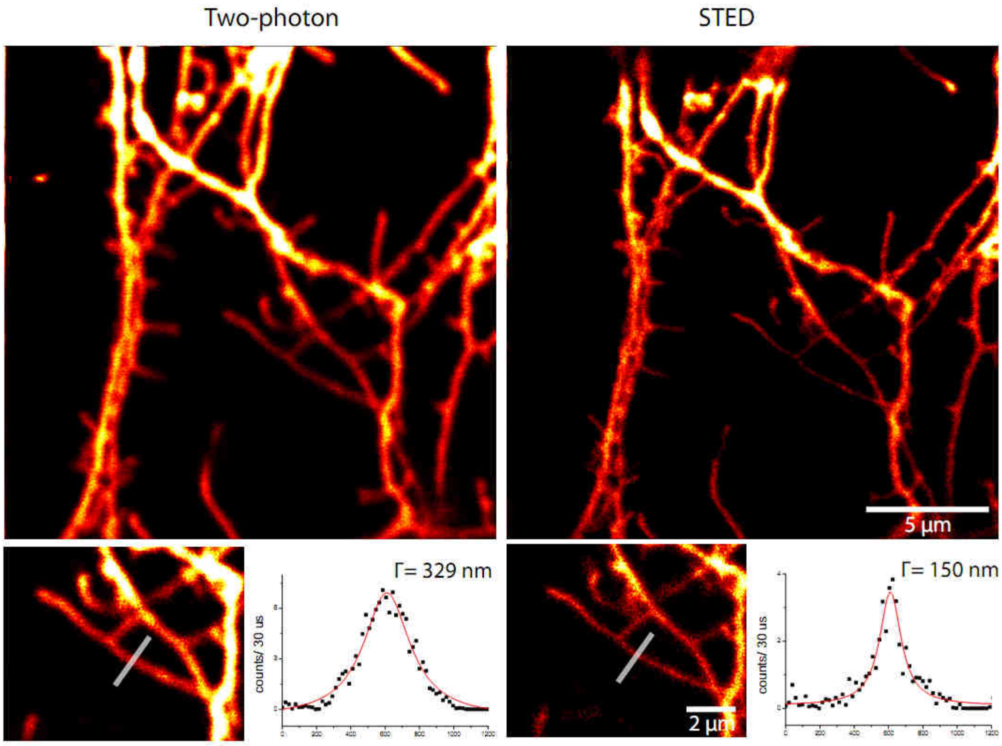

Figure 7: Neuroligin-1 GFP transfected dispersed hippocampal culture

Co-overexpression of Neuroligin-1 and GFP in dispersed hippocampal cultures. Lorentzian fits of a line profile indicate a clear resolution increase. The sample was kindly provided by Letellier,M. IINS Bordeaux.

To verify that our system is capable of recording from Banker-type cultures (sandwich cultures that grow on a layer of astrocytes)[65], two-photon STED recordings were carried out on cells that expressed GFP as a volume label (together with neurexin-1). A clear resolution enhancement is observable in fine neurite structures from these cells (Figure 7). It is noteworthy that no reflections of the coverslip degraded the image quality, although the cells grow and were imaged directly above the glass surface.

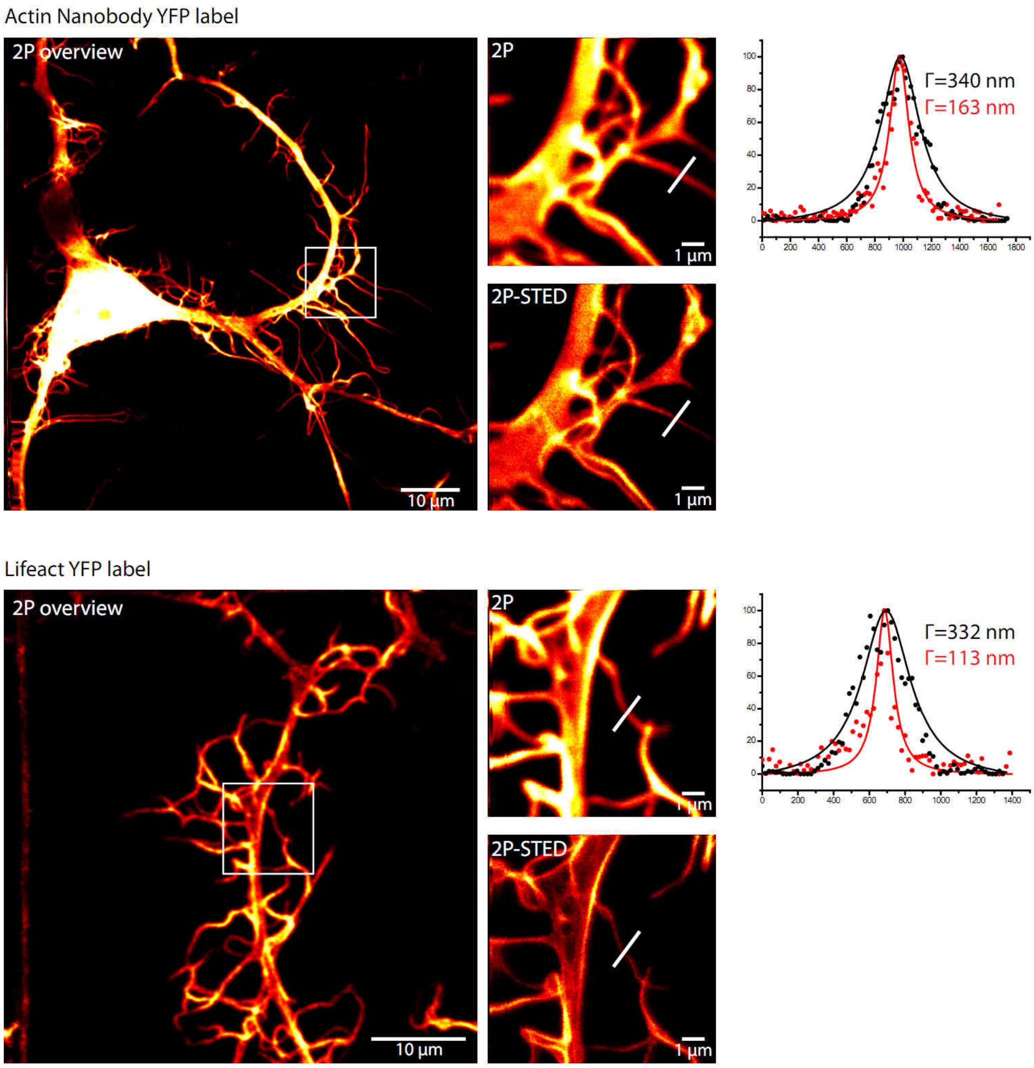

Figure 8: Actin nanobody-YFP and *lifeact*-YFP transfected dispersed hippocampal culture
Overexpression of Actin nanobody YFP and Lifeact YFP in dispersed hippocampal cultures. Lorentzian fits of a line profile indicate a clear resolution increase.

In contrast to overexpression of monomeric Actin-GFP which is likely to interfere with normal cytoskeleton function[53, 66], new probes such as Lifeact-GFP[66] and recently developed intracellular antibodies (auto- or nanobodies)[67], promise interference-free, specific and dynamic investigation of the cytoskeleton. To verify that the expression levels of these fusion proteins are high enough to allow STED imaging, dissociated hippocampal neurons were transfected with either Lifeact-YFP or Actin nanobody-YFP under the synapsin promotor (gift from M. Mikhaylova, Utrecht University). Both labelling strategies provide a strong enough signal for high resolution STED imaging (Figure 8). With both labelling strategies, a filamentous cytoskeleton network could be observed, which was much better resolved when the STED laser was turned on (Line profiles indicate a 2-3 fold smaller diameter in the STED case).

As nanobodies are smaller than antibodies (13 kDa vs. ~150 kDa), the fluorophore is closer to the epitope (especially when compared to primary-secondary antibody labelling) which minimizes the ‘linkage error’ between the fluorophore and the structure of interest (for antibodies typically on the order of 10 nm)[68].

While nanobodies (targeted against an overexpressed GFP fusion protein) have been used for single-molecule nanoscopy[68] and STED microscopy has been performed on single stranded DNA or RNA oligonucleotides(Aptamers)[69], the combination of STED microscopy with nanobodies directed against an endogenous epitope has (to our knowledge) not been performed to date.

Due to the micromolar binding affinity, the Lifeact molecule binds reversibly to the actin cytoskeleton. This simplifies repetitive imaging of the same structure as the high turnover rate of the fluorophore to the actin binding site allows novel fluorophores to replace bleached molecules[53]. This is not the case for the high affinity binding of the nanobody to the actin cytoskeleton for which repeated imaging has to be carried out to evaluate the use of this labelling strategy for time-lapse superresolution imaging.

2.3.2 Organotypic hippocampal slice culture

To bridge the gap between acutely prepared brain slices and dissociated neuronal cultures, the Gähwiler organotypic hippocampal culture system was developed[70]. The advantage of this culturing system over dissociated cultures is that the cellular architecture of the hippocampus stays intact, i.e. that the CA1 region can be discriminated from the CA3 region and field recording/ stimulation is still possible. In addition, the optical accessibility is higher than in acute brain slices and single-cell electroporation and viral infections can be performed on the cultured cells.

Cultures from Thy1-YFP mice are a standard in the laboratory and served as an initial performance test of the two-photon STED microscope. They strongly express the fluorophore YFP as a volume label in the CA1 region of the hippocampus (Figure 9).

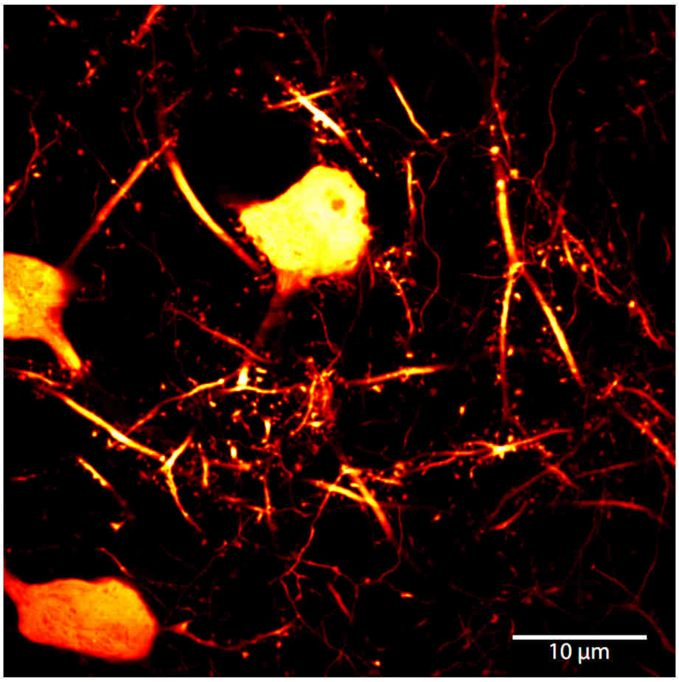

Figure 9: Organotypic cultures as an experimental preparation to study synaptic plasticity

Maximum-intensity projection of Thy1-YFP expressing cells in the CA1 region of the hippocampus in roller-tube cultures. This image was taken by using two-photon excitation only.

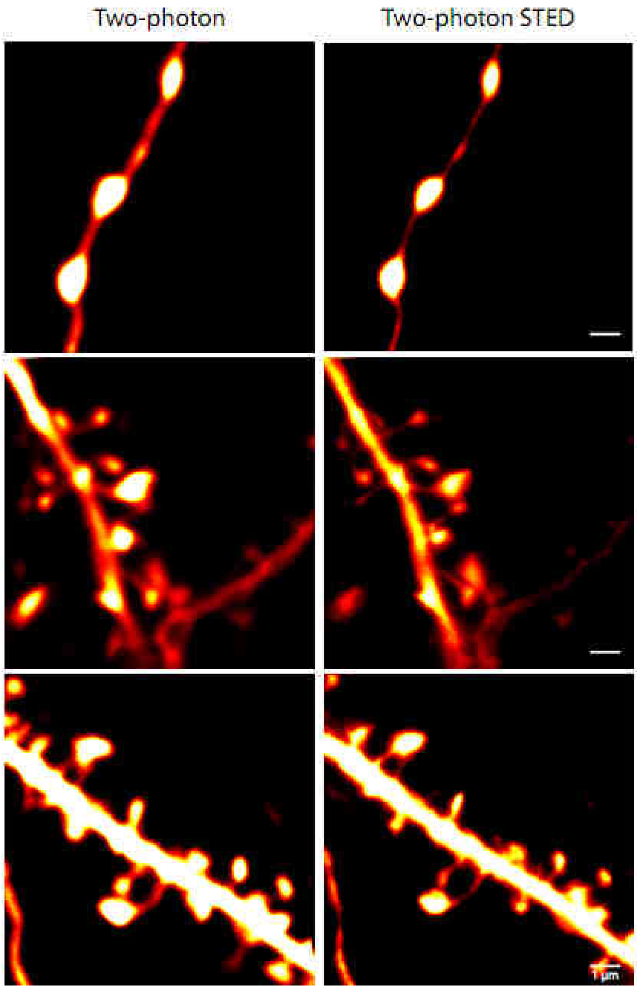

Figure 10: Two-photon STED in organotypic slice cultures

Average intensity projections of Thy1-YFP expressing organotypic hippocampal cultures DIV 18-24. In the two-photon STED case, the axon and dendritic spines appear much thinner and more detail is observable, compared to regular two-photon images. Bright structures are oversaturated to aid the visualization of thin axons or dendritic spine necks.

During culturing, cells that are dead or damaged are gradually removed due to the rotational movement of the cultures in culturing medium. Therefore, image acquisition is not influenced by cell debris on the surface (although the plasma clot might introduce an index mismatching problem). I was able to record both axonal and dendritic structures in the CA1 region of the hippocampus with a clear resolution enhancement over two-photon excitation alone (Figure 10). The image of axons (top row) was recorded on the bottom of the coverslip, imaging through approx. three cell layers.

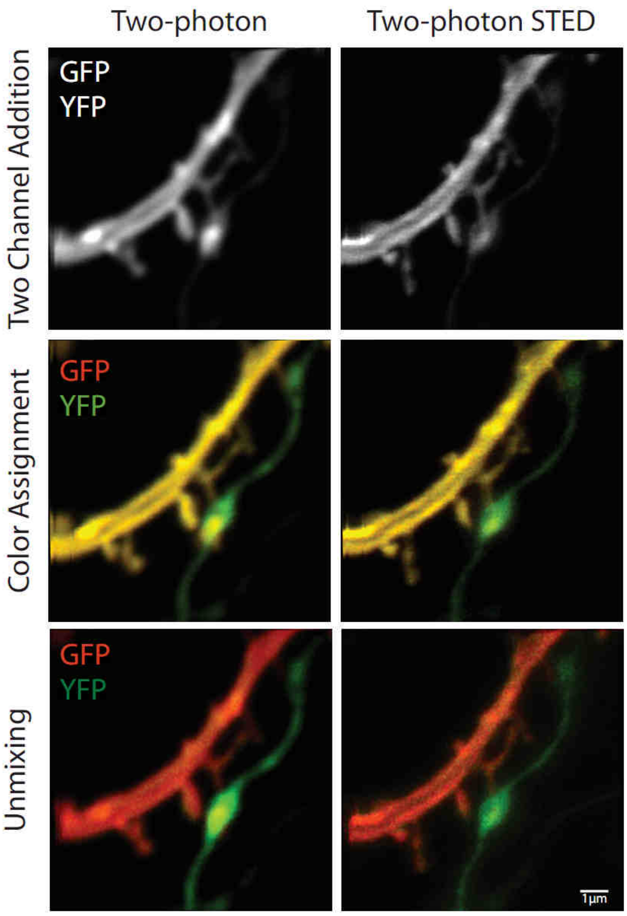

Figure 11: Linear unmixing of STED images from organotypic cultures

A Thy1-YFP cell forms a synapse with a Sindbis-GFP infected axonal bouton. Using two detectors, efficient two color linear unmixing can be performed to enhance the color contrast between cells expressing different green fluorophores.

As described in the published articles, the emission signal is directed to two independent detectors via a dichroic mirror. This allows the post-hoc separation of two-different green fluorophores by the process of linear unmixing. The ability to perform this task was tested in Thy1-YFP positive organotypic cultures which were infected 24 hours earlier with a Sindbis-GFP virus in the CA3 region (Figure 11). Here an axonal bouton could be localized that contacts a postsynaptic spine and presumably forms a synapse. Using STED, both the dendrite and the axon clearly illustrate the increase in resolution. The lower panels compare the color contrast obtainable by simply assigning green and red pseudo colors to the different channels (color assignment) or by performing post-hoc linear unmixing using the ImageJ “Spectral Unmixing Plugin", Walter, J.).

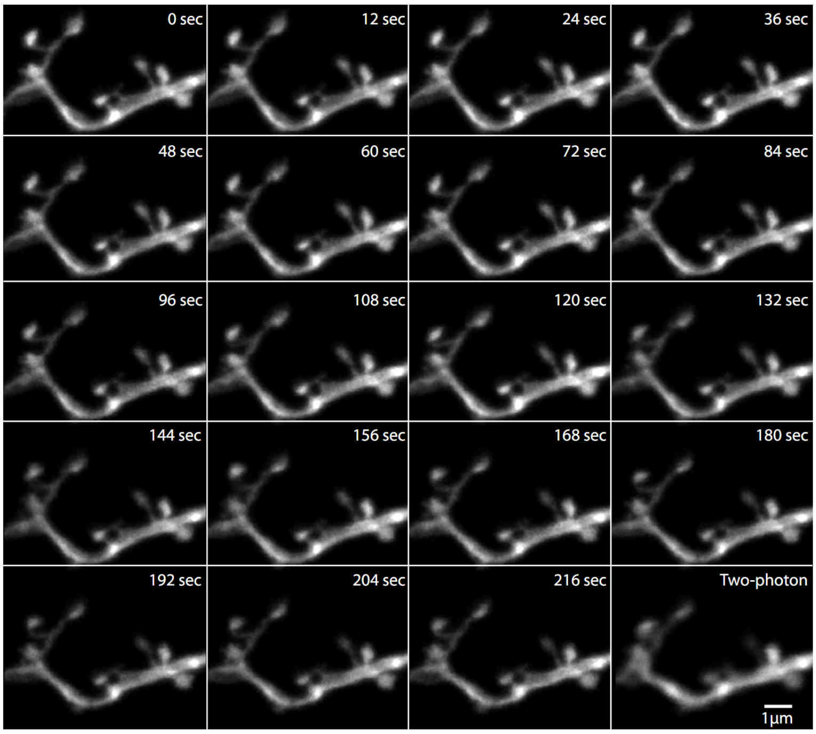

Figure 12: Timelapse imaging in organotypic cultures

Two-photon STED images of the same stretch of dendrite imaged continuously. Last frame was taking without the STED light on, illustrating the gain in resolution of the two-photon STED microscope.

For live-cell time lapse imaging, a small segment of a dendritic stretch was imaged repeatedly with $\Delta t = 12$ seconds. Because Figure 12 illustrates crops of larger frames, the time resolution could be increased if the field-of-view is reduced to the structure of interest alone. The last image was recorded in two-photon mode alone to give an estimate of the resolution enhancement by two-photon STED. Small movements of dendritic spine elements can be observed when this time-series is viewed as a movie. Importantly, no obvious blebbing of structure are visible in this example, illustrating that the microscope is capable to non-invasively record superresolved dendritic segments.

2.3.3 Dentate gyrus granule cell dendritic diameters

The dentate gyrus is the first structure within the hippocampal formation to receive direct input from the entorhinal cortex and does not project outside of the hippocampus. Its major input, the perforant path, originates in the entorhinal cortex and terminates via excitatory synapses on granule cell dendrites of the outer 2/3 of the molecular layer. The inner 1/3 of the dentate gyrus molecular layer receives almost exclusively inputs from ipsi- and contralateral projections from mossy cells of the polymorphic layer of the dentate gyrus and is called the associational/commissural projection[71]. These two pathways appear to exhibit different dendritic integration properties. Simulations show that constrictions of the dendritic diameter might explain the strong sublinear summation observed in distal dendrites by the group of Prof. Heinz Beck from Bonn University.

Therefore, I set out to record dendrites of the molecular layer in acute brain slices of Thy1-YFP mice.

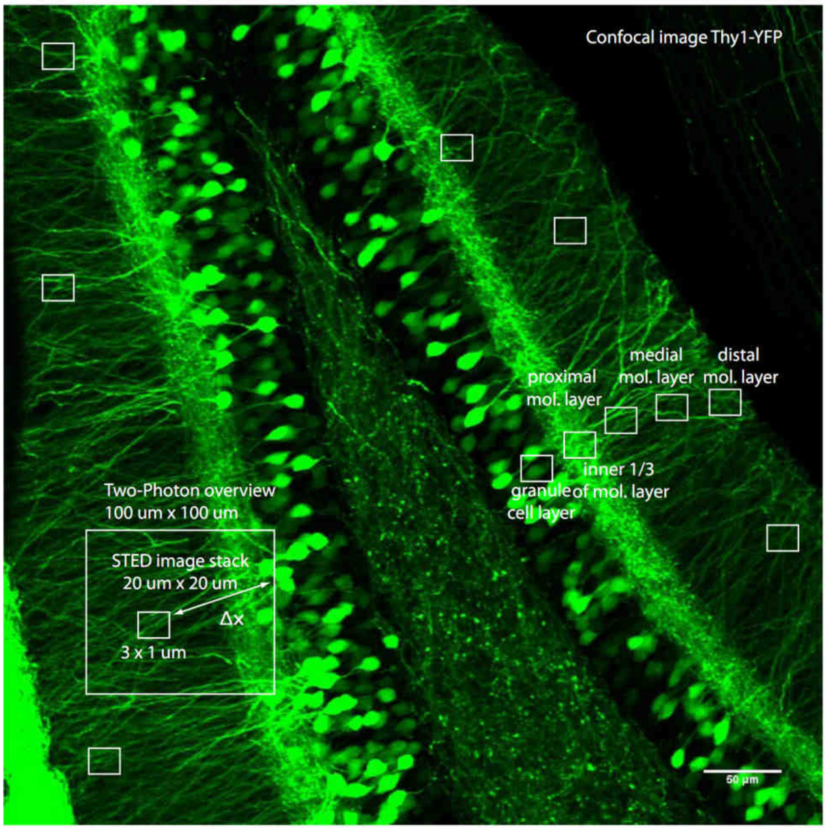

Figure 13: Imaging strategy dentate gyrus

Several high-resolution two-photon STED images were taken at different regions of the dentate gyrus. A low-resolution two-photon overview image facilitates the localization of the two-photon STED image. The vertical organization of the dentate gyrus was devinedas: granule cell layer, inner 1/3 of molecular layer (dense labeling of presynaptic elements) and 3 regions in the molecular layer (proximal-, medial-, and distal molecular layer.

Figure 13 illustrates the imaging strategy. From an overview image, several small (20µm x 20µm, 512x512 pixel, 3 z-planes with $\Delta z = 1\mu m$) at different regions of the molecular layer were recorded in two-photon STED mode. Image analysis was biased towards small diameters and revealed that dendrites of granule cells can be as thin as 150 nm in diameter. In EM reconstructions, dendrite diameters were found to be a thin as 200 nm in cerebellar granule cells and starbust amacrine cells[72]. The average of the line profiles measured across dendrites is with 350 nm close to the spatial resolution limit of most two-photon microscopes (Figure 14 D). This might indicate that the small dendritic diameters of these cells were simply overlooked because of insufficient resolution.

Furthermore, the smallest diameters were found in the distal regions of the molecular layer (Figure 15 A) which could indicate a dendrite tapering. It has to be noted, however, that the data was obtained via a population approach, and to be able to conclude a dendrite tapering, single-cell reconstructions should be performed. Patch-filling a granule cell of wild-type mice with a green fluorescent dye (such as Alexa 488 or ATTO 488) would allow the reconstruction of the complete dendritic tree of a single cell.

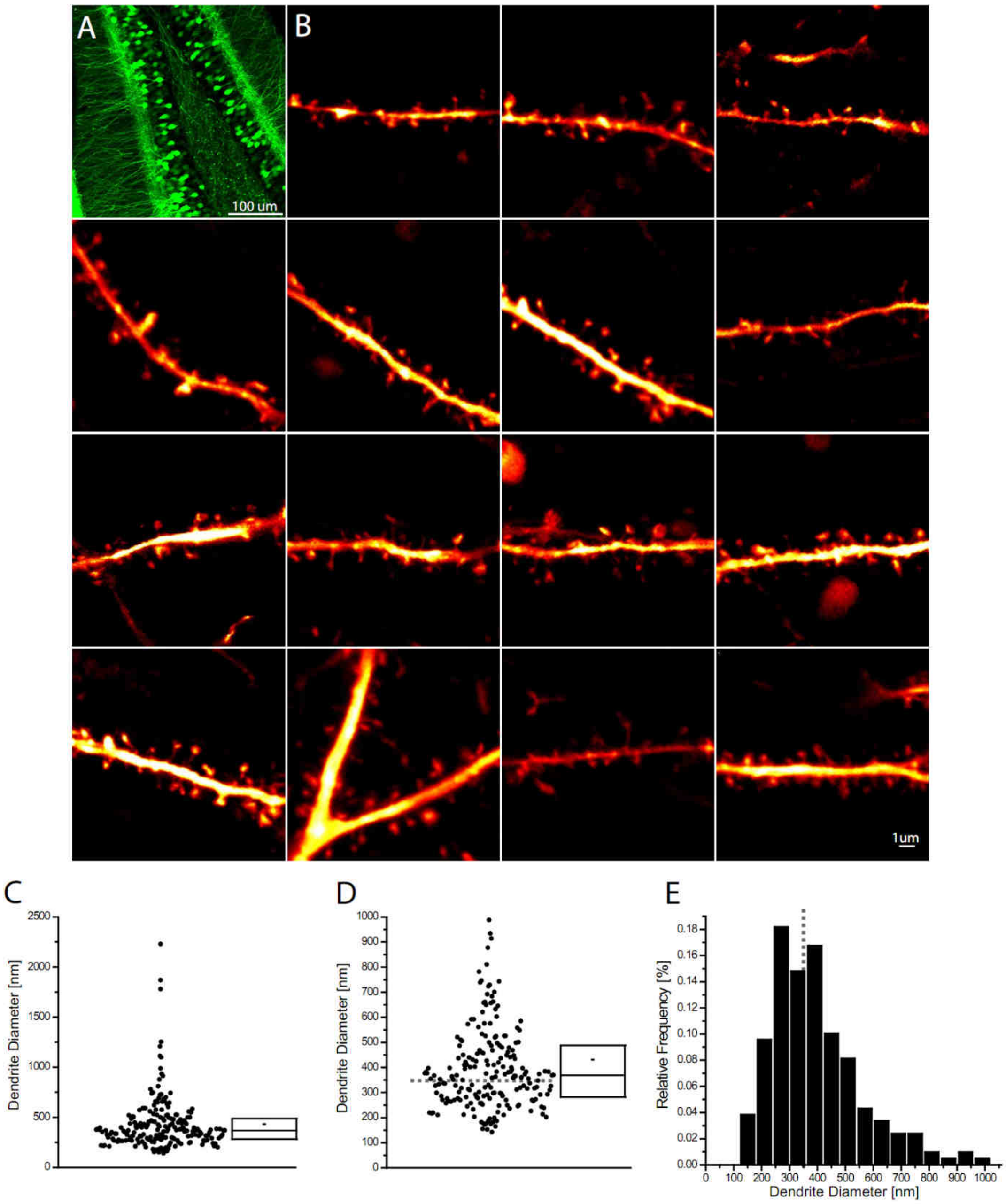

Figure 14: Dentate gyrus dendrite diameters

A) Confocal overview of dentate gyrus in Thy1-YFP mice. B) Examples of 2PE-STED microscopy in various regions of the dentate gyrus. C) Quantification of all dendritic diameters measured. Full range (C) and range limited to 1000 nm (D) are presented (scatterplot and histogram). Box is Q1, Q3, median and mean (large and small line, respectively). (E) Roughly 50% of diameter values are below the resolution limit of classic two-photon microscopy (~350 nm, dashed line)

Interestingly, the variability between line profiles on single dendrites (Figure 15 B) is high. This indicates (and can be observed in the sample images of Figure 14) that small stretches of thin diameters exist closely spaced to larger diameters. The data in Figure 15 C was obtained from a subset of dendrites where the somatic region was present in the overview image. Here a clear reduction in diameters is observable but also indicates that small diameters can exist close to the soma. These could be third- or fourth- order dendrites that extend away from the primary dendritic branch. No relationship between the dendritic diameters and the imaging depth could be observed, arguing against a thinning of the dendritic diameters due to cell damage as cells deeper in the slice should be healthier (Figure 15 D).

All data was obtained from 4 Thy1-YFP mice, aged between 3 and 9 weeks. The line profiles were 3 pixel wide and the diameters were obtained from fitting a Lorentzian function to the line profiles and reported as FWHM.

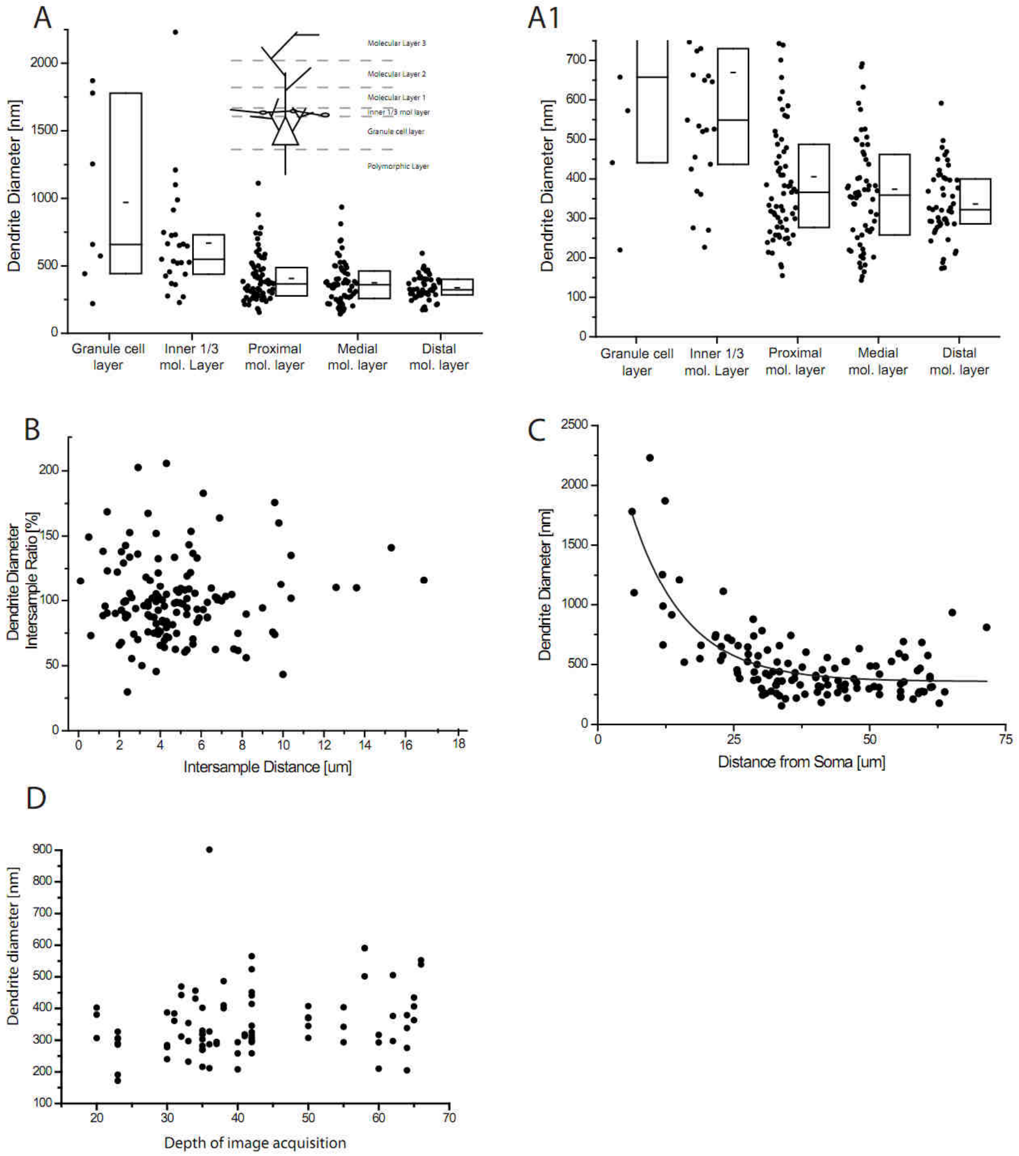

Figure 15: Dentate gyrus dendritic diameters are highly variable

A) Dentate gyrus granule cell dendrite diameters decrease with increase in distance from soma. Small insert illustrates regions chosen for acquisition (see Fig1 A for confocal overview). Box is Q1, Q3, median and mean (large and small line, respectively). Full range (A) and range limited to 750 nm (A1) is shown. B) Dendrite diameters substantially vary over distance. Relative difference in diameters between measurements on the same stretch of dendrite plotted against the distance between the measurements. C) For dendrites where the granular cell layer was visible in the overview image, the dendritic diameters decrease exponentially with distance from soma. D) The dendrite diameters do not differ at different image acquisition depths. The data used for this graph represents a subset of the whole dataset where the depth of image acquisition was recorded.

2.3.4 Spine neck micro-varicosities

While recording images from acute brain slices of Thy1-YFP mice, it became increasingly clear that a subset of dendritic spine necks show varicosities. Examples of this phenomenon are given in Figure 16.

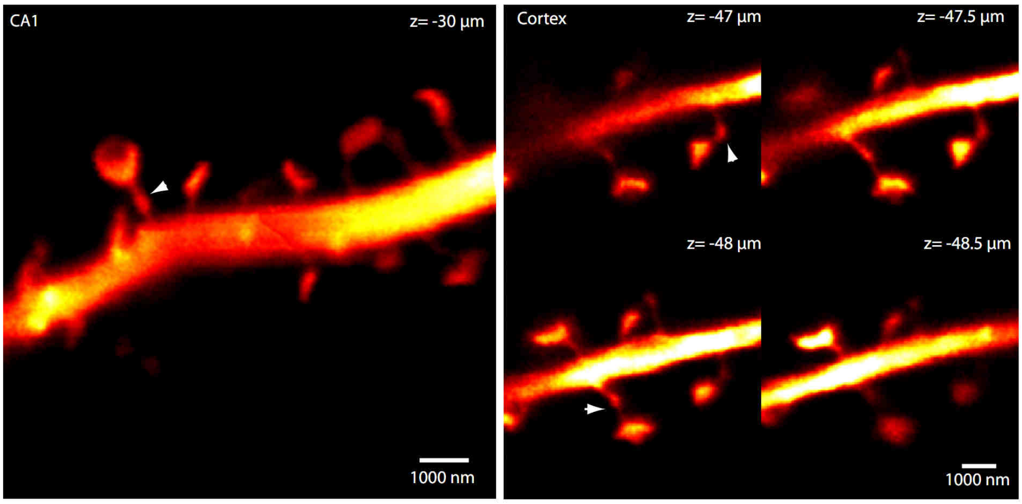

Figure 16: Micro-varicosities in the dendritic spine neck

A subset of dendritic spine necks of CA1 and cortex neurons in acute brain slices show small varicosities. The depth of acquisition is defined as the distance from the surface of the slice (z).

The origin or function of these varicosities remains speculation (such as mitochondria moving in our out of the spine head), it shall be stated, however, that similar varicosities were observed by group member Jan Tønnesen in organotypic cultures imaged with a single-photon excitation STED microscope (personal communication).

2.3.5 VGLUT-1-Venus

Glutamatergic synaptic vesicles of excitatory synapses in the brain are loaded by the vesicular glutamate transporter 1 (vGLUT1), which is the main glutamate transporter protein in synaptic vesicle. It is considered one of the most specific markers for glutamatergic synaptic vesicles and a knock-in mouse has recently been developed that expresses the fluorescent protein Venus tagged to the C-terminus of vGLUT1[73]. Venus is a bright green, yet not very photostable variant of EYFP[74] that is rarely used for STED imaging.

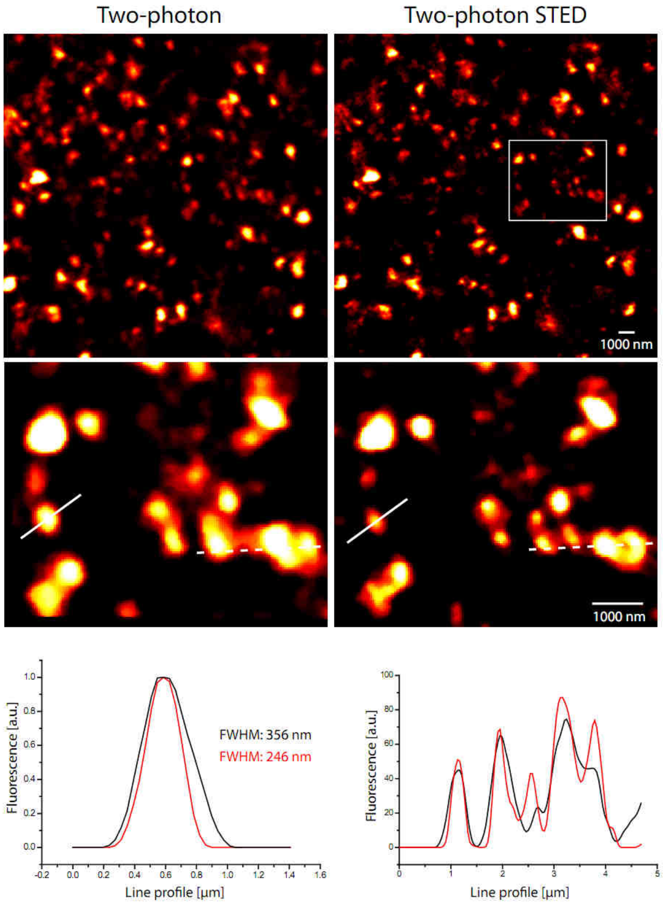

Two-photon

Two-photon STED

Figure 17: STED imaging of a vGLUT1-Venus mouse

As a proof-of-principle study we performed two-photon STED images of acutely prepared amygdala tissue slices of vGLUT1-Venus mice. Individual Venus labeled presynaptic structures are better resolved by the two-photon STED microscope. The sample was kindly provided by Xiaomin Zhang, IINS, Bordeaux.

A general concern with overexpressing fluorescently-tagged proteins is that the imbalance of protein copy numbers might interfere with the biological function of the overexpressed protein or the system it is overexpressed in. This is different for the VGLUT1-Venus mouse where the endogenous VGLUT1 gene was replaced by the fluorescently tagged VGLUT1-Venus gene under the same promoter. It was shown that this tag does not interfere with the function of the protein *in vivo*[73]. As a consequence of the endogenous copy numbers of proteins in the knock-in approach, the levels of the fluorescent proteins are usually low. This presents a problem for STED microscopy as the signal intensity of STED images are already much lower than regular confocal or two-photon excitation microscopy.

As a proof-of-principle experiment that also endogenous protein levels are suitable for STED microscopy, I recorded images of VGLUT1-Venus positive synaptic vesicle clusters in acute brain slices of the amygdala (Figure 17). The quantification of line profiles illustrates a moderate increase in spatial resolution of the STED microscope as compared to regular two-photon microscopy. Indeed, the signal bleached relatively quickly, which made low excitation power and lower STED power necessary to be able to record the image. Nevertheless, more photostable fluorophores and/or technological development of the microscope should allow superresolved time-lapse imaging of endogenous protein levels.

2.3.6 Nanoscale imaging *in vivo*

The most intact preparation for neuroscience is the intact brain. In contrast to acute brain slices, long range projections are not severed and the cells stay intact in their naïve environment. For imaging purposes this comes with a cost in optical accessibility and further challenges, such as whole animal handling and anaesthesia, movement artefacts from breathing and heart beat and the surgery for the craniotomy. The use of two-photon microscopy has made *in vivo* imaging possible because it allows up to 1 mm of penetration depth in the brain of a living mouse. This is due to the reduced scattering of the longer excitation wavelength and the option to install proximity, non-descanned detectors for efficient detection of scattered signal photons.

In vivo two-photon microscopy is applied for both functional and structural imaging. In functional imaging, fluorescent calcium indicators can be used to report the activity of neurons, while in structural imaging the morphology of the cells of the brain are of interest.

As demonstrated in Chapter 1 and 2 of the results, the two-photon STED microscope is capable of imaging depth > 50 µm and should hence allow deep superresolution imaging of neuronal structures *in vivo*. Figures 18 and 19 illustrate first steps towards this goal. Interestingly, signal levels were much stronger *in vivo* for the same mouse line, same age and same cortical region than compared to acute brain slices.

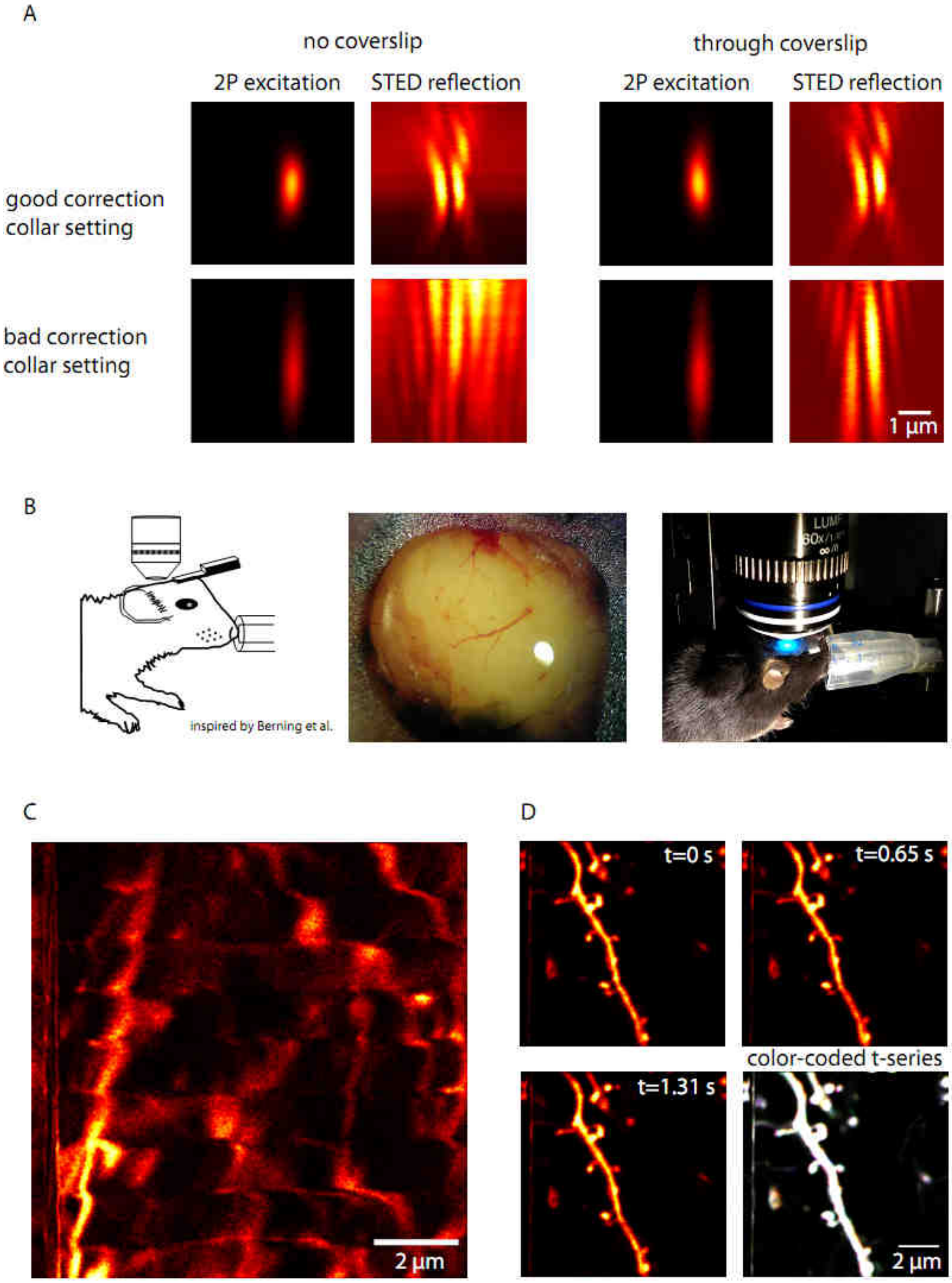

Figure 18: *In vivo* imaging preparation

A) The two-photon excitation PSF (2P excitation), probed by imaging 170 nm fluorescent beads, and the STED doughnut (probed by imaging gold bead reflection (STED reflection) can be optimized for imaging through a #1 coverslip. The objective's correction collar setting is critical for an optimized PSF. The 'bad correction collar setting' refers to the collar setting for the other condition (i.e. correction collar optimized for a coverslip but imaged without a coverslip).B) An illustration of the head holder and the anesthesia mask for *in vivo* imaging, the surface of the cortex under a glas coverslip, hold in place by dental acrylic, and a picture of the real-life setup. C) Strong motion artifacts can be observed when the surgery did not go well, i.e. the brain was not stabilized by the coverslip. Here, the heart beat of the mouse could be observed(see text). D) Motion artifacts can be minimized in optimal surgical conditions. The same stretch of dendrite was imaged in two-photon mode with 0.01 ms pixel dwell time for a 256x256 pixel frame. The last frame is a projection over time of 19 frames where each time point is color coded (color-coded t-series). White areas indicate areas where all timepoints (all colors) are on the same spatial coordinates i.e. no movement over time. In all experiments, a Thy1-YFP mouse (aged 10 weeks) was used.

The water-dipping objective Olympus LUMFL 60X NA1.1 is an objective that was designed to be used without a coverslip. It features a correction collar that allows aberration correction for deep imaging. As demonstrated in Figure 18 A, both the excitation PSF as well as the STED doughnut PSF are severely distorted when fluorescent beads or gold particles are imaged through a coverslip. Fortunately, the correction collar can be adjusted to compensate for the aberration mismatch between the immersion medium (water), the coverslip glas and the brain itself. This situation enables us to use a coverslip above the brain for *in vivo* imaging. The implantation of the coverslip stabilizes the brain and severely reduces motion artifacts (as compared to the open skull technique).

Figure 18 B illustrates our surgical approach (generally following [75]). A titanium headholder (Luigs&Neumann) is fixed on the skull with superglue and dental acrylic and allows the positioning of the mouse in a custom-made isofluoran anesthesia mask (Anestéo, Villetelle, France). A craniotomy is performed and 1.2% low melting agarose solution is used to stabilize the brain below a 3 mm, #1 coverslip (Warner Instruments, Hamden, USA). The coverslip is stabilized with superglue and dental acrylic before the mouse is transferred to a dedicated microscopy stage.

The image in Figure 18 C illustrates the motion artifacts that are induced by the heartbeat of the mouse. The 512x512 pixel frame was imaged with 0.005 ms pixel dwell time, which leads to an image acquisition time of 1310.72 ms. Roughly 9 distinct motion artifacts can be observed (1310.72ms / 9 motion artifacts = 145 ms / artifact) which corresponds to the heartbeat of a mouse (8 Hz = 1 beat / 125 ms) for a freely moving mouse[76]. Motion artifacts induced by breathing were never observed while the heart beat artifacts was stronger in cortical areas close to large blood vessels. In the case of a successful surgery, the motion artifacts can be dramatically reduced, as illustrated in Figure 18 D.

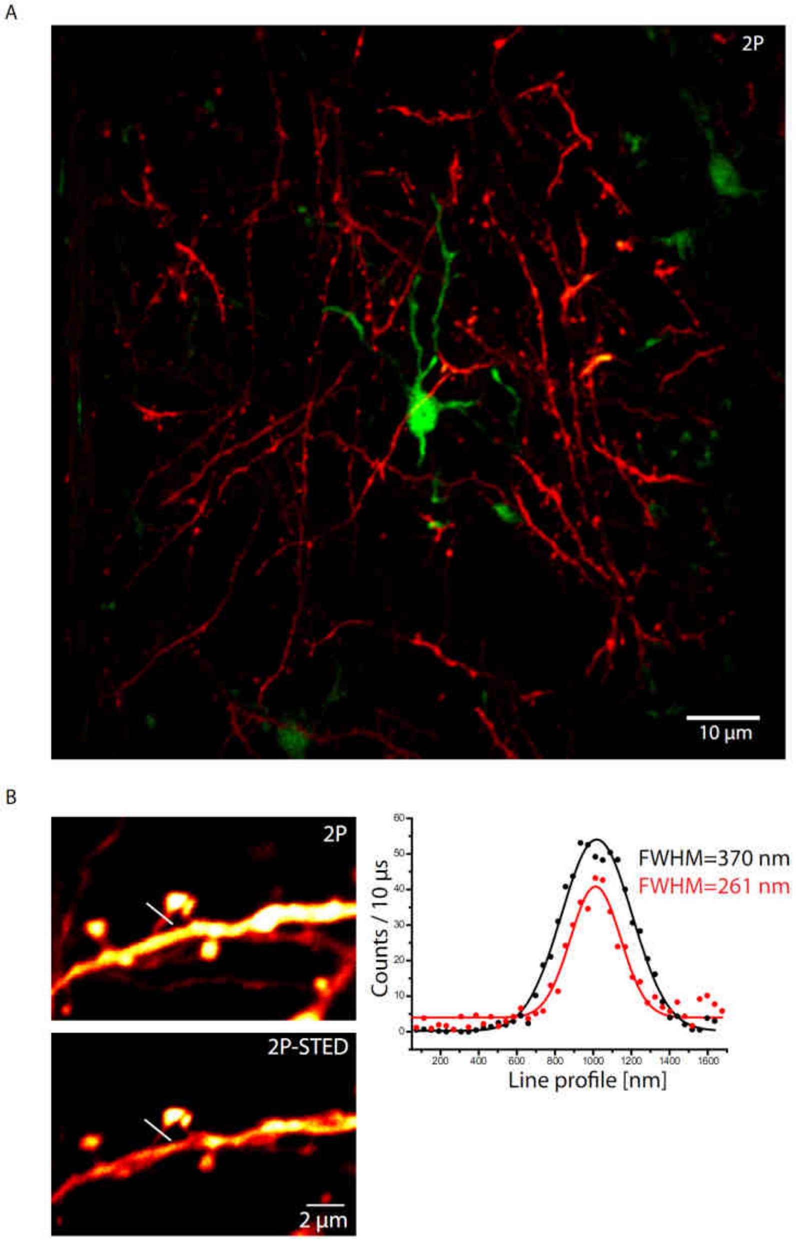

Figure 19: ***In vivo*** **STED Imaging**

A two-photon excitation maximum-intensity projection (2 frames) of a large field-of-view (150x150x85µm stack) of a Thy1-YFPxCX3-CR1-GFP mouse in the barrel cortex of a 10 week old mouse. Signals from neuronal structures and microglia were post-hoc processed (linear unmixing) and color merged. B) In the same preparation, STED illumination allows the quantification of much finer spine necks. Gaussian fits of the spine neck line profile illustrate the improved resolution.

Figure 19 presents a first example of two-photon excitation STED microscopy in the cortex of a living mouse. The Thy1-YFPxCX3-CR1-GFP mouse was operated as described above and a large two-photon excitation stack was recorded. Two-photon imaging could be performed 100 µm below the surface of the brain with no photobleaching observable over the course of 70 min (14 z-stacks). Microglia morphology is comparable to acute slice preparations and do not appear activated by the surgery (visual inspection, T. Pfeiffer, IINS Bordeaux). The illumination of a single dendritic segment with the STED laser (Figure 19 B) returns spine necks that appear ~ 100 nm thinner when compared to two-photon illumination alone.

3 Conclusions and Outlook

STED microscopy has come a long way from its first theoretical prediction in 1994 to *in vivo* imaging recently[30]. However, technological challenges and certain initial limitations like live-cell compatibility have certainly delayed its full application in neuroscience research. Part of this problem was that initial STED microscopes were designed around the demands for STED microscopy and not around the demands of neuroscientific research applications. These demands are often in conflict which each other, such as opto-mechanical stability is higher for inverted systems but upright microscopes are favourable for acute brain slices and absolutely necessary for *in vivo* applications. In addition, oil objectives are incompatible with upright systems while water-dipping objectives have a lower NA.

The goal of this work was hence the development of a STED microscope that is readily compatible with the most common brain preparations in neuroscience and allows nanoscale live-cell imaging of the popular green fluorescent dyes and proteins deep inside scattering tissue. This microscope should make special cell culture preparations redundant and hence foster the application of STED microscopy in neuroscience.

The results of this thesis provide evidence that these goals have been achieved by using a two-photon excitation scheme combined with a pulsed STED laser on an upright microscope with a water-dipping objective. Especially the use of the pulsed STED laser allows live-cell time-lapse imaging with superior resolution compared to regular two-photon microscopy and continuous-wave two-photon STED microscopes. The challenge associated with pulsed lasers is the necessity of having the pulsed two-photon excitation laser synchronised and optimally delayed in time, with respect to the pulsed STED laser. As tunable two-photon lasers feature a resonator cavity where the light emitted from the gain medium interferes to form standing waves (or modes), the synchronisation to an external pulse repetition frequency demands a precise stabilization of the cavity length. In contrast to earlier reports that used a custom-build optical parametric oscillator, the system described here utilizes a commercial option for researchers that do not have the background to build their own lasers. Because of the pulsed nature of the STED light, lower average power (~30 mW compared to ~200 mW for CW lasers in the BFP) can be used, which is important for time-lapse live-cell imaging. Precise delay of the STED pulse relative to the excitation pulse also allow for pulse duration probing on the picosecond range which would otherwise require sophisticated equipment such as autocorrelators. Additionally, this system is also capable of probing the fluorescence lifetime of molecules which should allow FLIM measurements inside thick biological specimens.

The use of a water-dipping objective over oil-immersion objectives has the advantage of a lower refractive index mismatch between the immersion medium and the aqueous cellular environment. The reduced refractive index mismatch minimizes spherical aberrations which can be detrimental to the quality of the STED doughnut. The 60x 1.1NA objective used for this microscope also features a correction collar for spherical aberration correction which is adjusted depending on the imaging depth. Recently, glycerol (n=1.46) objectives have also been used for STED imaging which feature a refractive index which is closer to that of brain tissue ($n \approx 1.37$) than oil immersion objectives (n=1.57). With these objectives, deeper penetration depths can be obtained, albeit only because a coverslip is between the sample and the immersion medium, and for upright systems, which allow access for electrophysiological recording equipment, glycerol objectives are not an option.

Previous two-photon STED reports have either used stage scanning or excitation and STED wavelengths that are in the near-IR. Microscopes that feature stage scanning have the clear advantage over beam-scanning schemas as such as they do not need relay optics before the objective to keep the beam stationary in the BFP. Therefore, only axial chromatic aberrations can be introduced by the relay lenses and the objective, but which can be compensated by de-collimating one of the two beams before the objective. In beam-scanning, where the two superimposed beams hit the relay lenses at varying angles, lateral chromatic aberrations can cause additional problems. This can be minimized by reducing the wavelength difference between the STED and the two-photon beam (i.e. by using the same wavelength but different pulse lengths)[62] or by choosing the excitation and STED beam wavelength so that they both fall within a wavelength range where the optics are well corrected for[58, 61]. Unfortunately, in the case of two-photon STED microscopy of green fluorophores, the two-photon beam needs to be in the near-IR for excitation and the STED beam has to be within the emission spectrum of the fluorophore and hence in the visible spectrum. Classic scan- and tube lens systems are chromatically corrected for either the VIS or the near-IR range and only feature anti-reflection coating in the other respective domain. As the presented microscope is unique and first-of-its-kind, the initial optics were suboptimal and lead to a reduced field-of-view as the excitation PSF and the STED doughnut get misaligned for larger scan angles (Figure 20).

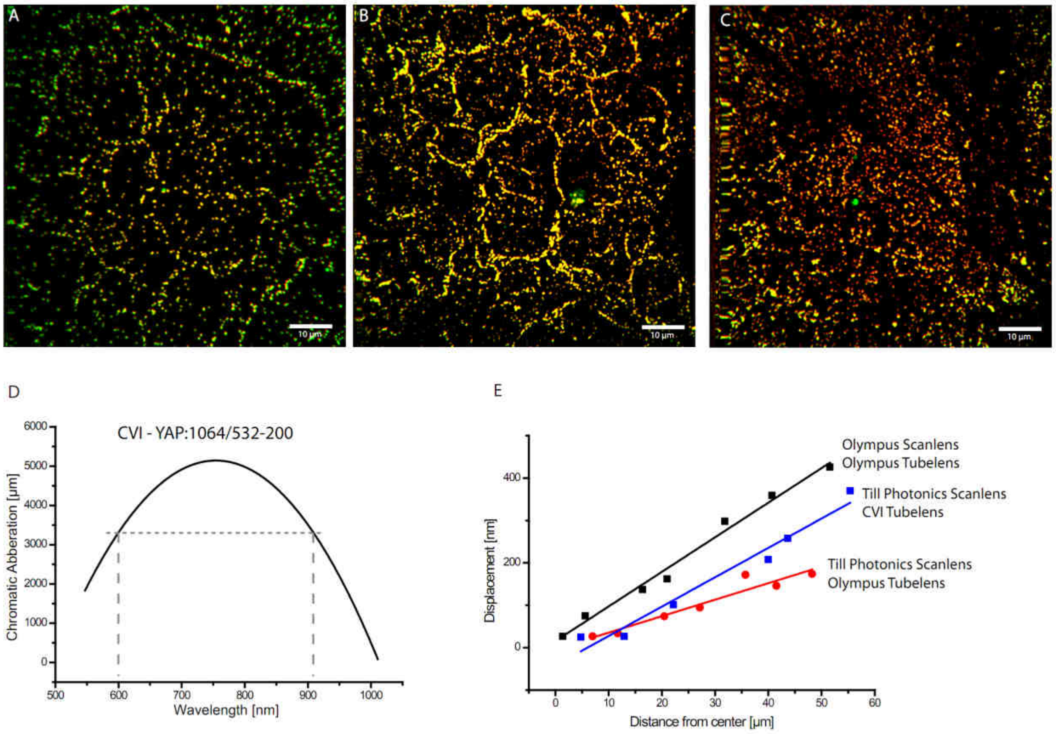

Figure 20: Chromatic aberration for different scan-tubelens combinations

A) The original Olympus Scanlens (FV3-PLWI) and Tubelens (U-TLUIR) from Olympus show considerable lateral chromatic aberration. For illustration, the two-photon beam (red) and the STED beam (green, without the vortex phase mask) show overlap in a central region but dissipate at larger scan angles. B) The dissipation between the two focal spots is reduced with a recently developed f=40 scanlens from Till Photonics. C) The replacement of the Olympus tubelens with the CVI YAP:1064/532-200 lens worsened the chromatic aberrations. D) Chromatic aberration of the CVI lens as a function of wavelength. E) The graph illustrates the displacement of the two-photon and the STED foci as a function of distance from the center. The Till Photonics scan lens together with the Olympus tube lens leads to a minimal chromatic aberration.

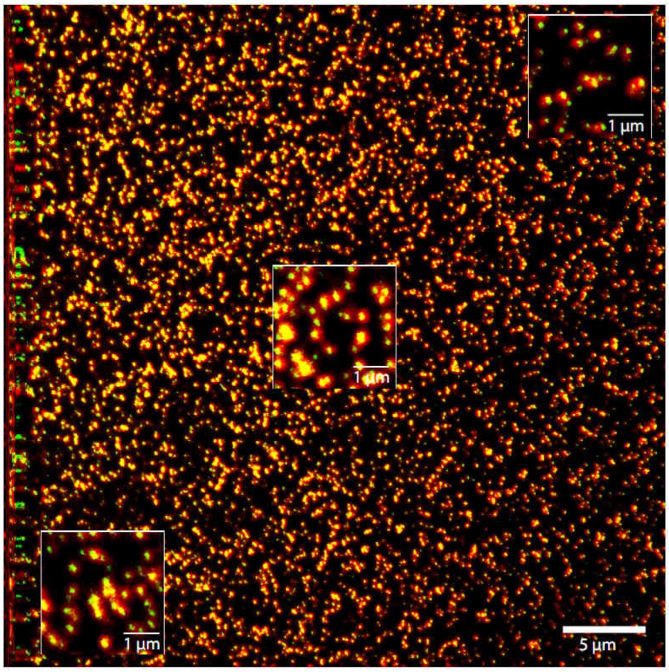

Figure 21: High-NA silicon oil immersion objective

Immobilized 40 nm fluorescent beads were imaged through a #1 coverslip with a 1.3 NA 60x silicon immersion objective (Olympus UPLSAPO60X). A clear resolution enhancement can be observed across the 40 µm x 40 µm field-of-view (red: two-photon, overlaid green: two-photon STED).

Recent efforts to improve the microscope were therefore directed towards implementing a special scan and tube lens combination (Till Photonics f40 scan lens and CVI Melles Griot YAP-200.0-40.0-1064/532 tube lens). The scan lens features a chromatic focal shift of only ~ 5 µm between the principle excitation and STED wavelength (600 nm and 910 nm) at its largest acceptance angle. This lens clearly improved the chromatic shift issues as demonstrated in Figure 20. ZEMAX simulations showed that the CVI tube lens (which is corrected for 532 nm and 1064 nm but features a constant chromatic aberration offset for 600 nm and 920 nm, Figure 20 D) should further improve the misalignment for larger scan angles, a prediction that did not hold true (Figure 20 E).

Precise estimates of lateral and axial chromatic shift are compromised by the commercial suppliers because the lens data underlies strict confidentiality regulations.

A new silicon immersion objective has been tested on the setup recently (Figure 21). This objective features a high NA and the refractive index of 1.40 is closer to brain (~

1.37) than any other immersion medium. On 40 nm fluorescent beads, the objective performs very well (lateral STED resolution ~ 50 nm) and should be very beneficial for *in vivo* STED imaging approach, if the surgery complies with the low working distance of 0.3 mm.

Although a spatial resolution enhancement from ~ 350 nm to ~ 60 nm in the lateral direction was achieved, future development of the microscope should also increase the resolution in the axial direction. Several 3D STED options have been described such as using an additional phase plate that introduces a π phase shift in a central disc, which quenches the excited molecules above and below the center of the excitation PSF[77, 78]. Recently, also programmable spatial light modulators (SLM) have been demonstrated that additionally allow aberration correction of the STED doughnut[79, 80]. Improving on the z-resolution in two-photon microscopy is likely to have a dramatic effect as the two-photon PSF in the axial direction is often several microns long.

Additional technological development of the system will include a proximity detection module to allow efficient detection of scattered photons deep inside brain tissue. The initial use of avalanche photodiodes for detection was motivated by the demonstrated quality of this detection method by previous STED microscopes. They allow an excellent signal-to-noise ratio due to high detection sensitivity paired with low dark noise. On the other hand, because of the small active area, the signal light has to be delivered via an optical fiber that can act as a confocal pinhole. As a confocal pinhole is dispensable in two-photon microscopy, high quality photo-multiplier tubes with a large active window and located close to the BFP of the objective will collect more scattered signal photons. The opto-mechanical implementation of these detectors should be rather simple as only a dichroic mirror and the detectors itself need to be installed. The analog output of the PMTs can readily be recorded by the NI-DAC cards and used for image formation. Along the same line of argument, high-NA but low magnification objectives with a large BFPs (i.e. 20x, NA 1.0) would also be of interest for an increased signal detection. A potential problem might arise as the large BFPs need to be sufficiently overfilled to achieve true diffraction limited PSF formation. A smaller focal length scan lens (such as the one that is being tested) together with a longer focal length tube lens could provide the necessary magnification of the excitation and STED beam.

This thesis work was mainly concerned with the design and construction the microscope. Examples of two-photon STED microscopy applications in neuroscience have been described in the reports as well as in chapter 3 of the results. Further work is intended to demonstrate the flexibility of the system for biological questions in the various biological preparations.

A good example are the measurements carried out on dendrites of the granule cells in the dentate gyrus. Once the expression of YFP in granule cells was confirmed, the recording on acute brain slices could be performed. As the expression levels of YFP were lower in the dentate gyrus as compared to the CA1 area, these measurements will be repeated on the Thy1-GFP M-line which expresses GFP mainly in the dentate gyrus. In addition, patch-filling of granule cells will allow the reconstruction of the full arborisation of the dendritic tree. Ideally, the nonlinear integration of EPSPs in the dendrites of these cells should be probed by simultaneous glutamate uncaging and STED imaging by incorporation of an uncaging laser in the beam path by a dichroic mirror.

The observed micro-varicosities in dendritic spine necks are an example of novel morphological findings made possible by superresolution imaging. With conventional two-photon microscopy these varicosities are too small to be discriminated from spine neck while electron microscopy would only detected these structures after extensive reconstruction of a large amount of dendritic spines. Time-lapse imaging would be a first step towards the identification of the origin of this observation.

As mentioned before, these structures were also observed on a different STED system in organotypic slice cultures in the laboratory. The two-photon STED microscope could rule out the possibility that these structures are due to a culturing artefact.

Initial experiments on acute brain slices of VGLUT-1 Venus mice demonstrated the principle feasibility of two-photon STED microscopy on endogenous expression levels of fluorescent proteins.

The development of novel fluorescent markers and creative labelling strategies is of great importance to the field of superresolution. The demonstration that nanobodies are suitable markers for STED microscopy will benefit the field as this strategy allows virtually any intracellular protein to be labelled by high-specificity nanobodies and subsequent time-lapse imaging of their dynamics in living cells.

The last example in the results section illustrates our efforts to take *in vivo* STED imaging into deeper layers of the cortex. The principle feasibility was reported recently[30] demonstrating time-lapse imaging of dendritic spines in the most superficial layer of layer I of the somatosensory cortex. Because of some of the reasons mentioned earlier in the discussion (refractive index matching of the water immersion objective to brain tissue, two-photon excitation, short STED pulses, etc.), there is reason to assume that the microscope presented here will allow superresolution imaging in deeper inside the molecular layer of the cortex, given the challenges associated with *in vivo* imaging, such as motion artefacts, are solved. A first demonstration of two-photon STED microscopy in molecular layer I of the mouse cortex was presented in this thesis work.

The connection between structural and functional synaptic plasticity has been demonstrated for many different synapses in different areas of the brain and is considered to be a mechanism for long-lasting memory traces. With the tools on our hand, we can now investigate the nanometric structural changes that accompany or underlie functional changes in synaptic transmission, e.g. after the induction of synaptic plasticity like LTP. The LTP paradigm is one of the most popular functional plasticity paradigms used in neuroscience for eluding the cellular mechanism of learning and memory.

A pressing question concerns also the morphological synchronisation between pre- and postsynaptic structural plasticity. Postsynaptic spine head enlargement can be readily induced by two-photon uncaging of caged glutamate. It was shown that the structural changes on the spine head coincide with a strengthening of the synapse via an increase in AMPA-receptor mediated currents[81]. At present it is unclear if this spine head enlargement also leads to a remodelling of the associated spine neck. On the other hand, long-term depression in hippocampal organotypic slice cultures leads to a reduction in presynaptic boutons and a loss of contact to postsynaptic spines[82]. In both cases a two-photon microscope, was used for detection of the morphological changes.

Combining the two experiments with the two-photon STED microscope would allow insights in the fine changes that might lead to pre- and postsynaptic structural plasticity coupling. For example, fine protrusions of the spine head have been reported and their development was suggested to be associated with the growth of new postsynaptic processes that connect to a presynaptic partner[83].

Similarly, inhibitory presynaptic terminals undergo morphological changes over time[84]. Here, the postsynaptic synthesis and presynaptic site of action of the endocannabinoid system suggests a potential mechanism for pre- and postsynaptic morphological coupling.

The presented microscope allows nanoscale observation of the fine structures of the nervous system that are dynamic and believed to represent structural correlates of functional adaptability, one of the unique characteristics of the brain. Although STED microscopy is still in its infancy when compared to more traditional optical imaging techniques, there is reason to believe the STED (or other superresolution technology) will have a similar impact on neuroscience as two-photon microscopy.

For example, a quick search on the PubMed database reveals a strikingly similar development of publications concerning the key word ‘two-photon+microscopy’ and ‘STED+microscopy’ when normalised to the first publication of the respective keyword.

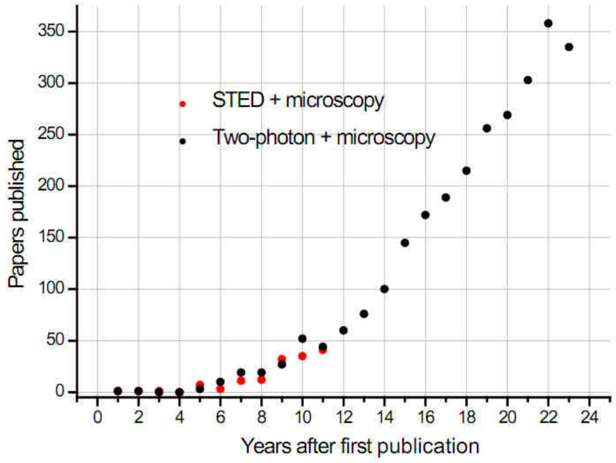

Figure 22: Publication development of two-photon microscopy versus STED microscopy

Key word search on PubMed (NIH) database for ‘two-photon+microscopy’ and ‘STED+microscopy’ per year, normalised to the year of first publication (as of 05/03/2013).

This development might be interpreted as a predictor for a similar successful development of STED microscopy as two-photon microscopy, which now produces an average of about 350 peer-reviewed reports per year.

In conclusion, I have presented the design, construction and application of a novel two-photon STED microscope for dual-color imaging in the most popular biological preparations in neuroscience. Further technological development and its application to current questions in brain science will demonstrate the importance of the presented concept for superresolution imaging.

4 Literature

1. Ralston, A.P., *Discoverer of the UnseenWorld: A Biography of Antoni van Leeuwenhoek.* World Pub. Co, 1966.
2. Singer, C., *Notes on the Early History of Microscopy.* Proc R Soc Med., 1914. **7**(Sect Hist Med): p. 247-279.
3. Golgi, C., *Sulla struttura della sostanza grigia del cervello.* Gazzetta Medica Italiana (Lombardia), 1873. **33**: p. 244-246.
4. Ramón y Cajal, S., *Textura del Sistema Nervioso del Hombre y de los Vertebrados.* Moya, Madrid, Spain, 1899.
5. Gerlach, J.V., *Von dem Rückenmark.* Handbuch der Lehre von den Gewegen des Menschen und der Tiere. S. Stricker (Ed.), 1872: p. 684.
6. Golgi, C., *Sulla fina anatomia degli organi centrali del sistema nervoso IV. Sulla fina anatomia delle circonvoluzioni cerebellari.* Riv. Sper. Freniatr. Med. Leg. Alien. Ment., 1883. **9**: p. 1-17.
7. Azevedo, F.A., L.R. Carvalho, L.T. Grinberg, J.M. Farfel, R.E. Ferretti, R.E. Leite, W. Jacob Filho, R. Lent, and S. Herculano-Houzel, *Equal numbers of neuronal and nonneuronal cells make the human brain an isometrically scaled-up primate brain.* The Journal of comparative neurology, 2009. **513**(5): p. 532-41.
8. Henneberger, C., T. Papouin, S.H. Oliet, and D.A. Rusakov, *Long-term potentiation depends on release of D-serine from astrocytes.* Nature, 2010. **463**(7278): p. 232-6.
9. Hebb, D.O., *The Organization of Behaviour: A neuropsychological theory*1949, New York: Wiley.
10. Bliss, T.V.P. and G.L. Collingridge, *A synaptic model of memory: long-term potentiation in the hippocampus.* Nature, 1993. **361**(6407): p. 31-39.
11. Shaner, N.C., P.A. Steinbach, and R.Y. Tsien, *A guide to choosing fluorescent proteins.* Nature Methods, 2005. **2**(12): p. 905-9.
12. Schiazza, O.L., *Fast Two-Photon Excited Fluorescence Imaging for the Human Retina.* Dissertation Ruprecht-Karls-Universität, Heidelberg, 2008.
13. Stehlik, D., *The Mechanism of Optical Nuclear Polarization in Molecular Crystals*, in *Excited States*, E. Lim, Editor, Academic Press. p. 204-300.
14. Minsky, M., *Microscopy apparatus. US patent 3013467.*
15. Minsky, M., *Memoir on inventing the confocal scanning microscope.* Scanning, 1988. **10**: p. 128-138.
16. Göppert-Mayer, M., *Über Elementarakte mit zwei Quantensprüngen.* Dissertation Universität Göttingen, 1930.
17. Göppert-Mayer, M., *Über Elementarakte mit Zwei Quantensprüngen. , :273–294.* Ann. Phys.(Leipz.), 1931. **401**(3): p. 273-294.
18. Göppert-Mayer, M., *Über die Wahrscheinlichkeit des Zusamenswirkens zweier Lichtquanten in einem Elementarakt.* Naturwissenschaften, 1929. **17**(932).
19. Dobrydnev, B. and M. Havey, *Theoretical investigation of two-color, two-photon, 6s 2S1/2-->5d 2Dj-->11p 2P3/2 excitation and depolarization spectra in atomic Cs.* Physical review. A, 1995. **52**(5): p. 4010-4016.

20. Lakowicz, J.R., I. Gryczynski, H. Malak, and Z. Gryczynski, *Two-color two-photon excitation of fluorescence.* Photochemistry and photobiology, 1996. **64**(4): p. 632-5.
21. Lim, M. and C. Saloma, *Primary spherical aberration in two-color (two-photon) excitation fluorescence microscopy with two confocal excitation beams.* Applied optics, 2003. **42**(17): p. 3398-406.
22. Quentmeier, S., C.C. Quentmeier, P.J. Walla, and K.H. Gericke, *Two-color two-photon excitation of intrinsic protein fluorescence: label-free observation of proteolytic digestion of bovine serum albumin.* Chemphyschem : a European journal of chemical physics and physical chemistry, 2009. **10**(9-10): p. 1607-13.
23. Maiman, T.H., *Stimulated optical radiation in ruby.* Nature, 1960. **187**: p. 493-494.
24. Singh, S. and L.T. Bradley, *Three-photon absorption in naphthalene crystals by laser excitation.* Phys. Rev. Lett., 1964. **12**: p. 612-614.
25. Denk, W., D.W. Piston, and W.W. Webb, *Multi-photon molecular excitation in laser-scanning microscopy*, in *Handbook of biological confocal microscopy.*, J.B. Pawley, Editor 2006, Springer Science+Business Media LLC: New York. p. 535-549.
26. Denk, W., J.H. Strickler, and W.W. Webb, *Two-Photon Laser Scanning Fluorescence Microscopy.* Science, 1990. **248**: p. 73-76.
27. Soeller, C. and M.B. Cannell, *Two-photon microscopy: imaging in scattering samples and three-dimensionally resolved flash photolysis.* Microscopy Research and Technique, 1999. **47**(3): p. 182-95.
28. Centonze, V.E. and J.G. White, *Multiphoton excitation provides optical sections from deeper within scattering specimens than confocal imaging.* Biophysical Journal, 1998. **75**: p. 2015-2024.
29. Hell, S.W., K.I. Willig, M. Dyba, S. Jakobs, L. Kastrup, V. Westphal, and *Nanoscale resolution with focused light: Stimulated emission depletion and other reversible saturable optical fluorescence transition microscopy concepts*, in *Handbook of biological confocal microscopy.*, J.B. Pawley, Editor 2006, Springer Science+Business Media LLC: New York. p. 571-579.
30. Berning, S., *STED Nanoscopy of the Living Brain.* Dissertation Georg-August-Universität Göttingen, 2011.
31. Rankin, B.R., *Stimulated Emission Depletion Microscopy with Stimulated Raman Scattering Light Sources.* Dissertation Ruprecht-Karls-Universität, Heidelberg, 2010.
32. Hell, S.W. and J. Wichmann, *Breaking the diffraction resolution limit by stimulated-emission - stimulated-emission-depletion fluorescence microscopy.* Opt. Lett., 1994. **19**: p. 780-782.
33. Betzig, E., G.H. Patterson, R. Sougrat, O.W. Lindwasser, S. Olenych, J.S. Bonifacino, M.W. Davidson, J. Lippincott-Schwartz, and H.F. Hess, *Imaging intracellular fluorescent proteins at nanometer resolution.* Science, 2006. **313**(5793): p. 1642-5.
34. Hess, S.T., T.P. Girirajan, and M.D. Mason, *Ultra-high resolution imaging by fluorescence photoactivation localization microscopy.* Biophysical Journal, 2006. **91**(11): p. 4258-72.

35. Rust, M.J., M. Bates, and X. Zhuang, *Sub-diffraction-limit imaging by stochastic optical reconstruction microscopy (STORM).* Nature Methods, 2006. **3**(10): p. 793-5.
36. Gustafsson, M.G., *Surpassing the lateral resolution limit by a factor of two using structured illumination microscopy.* Journal of Microscopy, 2000. **198**(Pt 2): p. 82-7.
37. Toomre, D. and J. Bewersdorf, *A New Wave of Cellular Imaging.* Annual Review of Cell and Developmental Biology, 2010. **26**(1): p. 285-314.
38. Leung, B.O. and K.C. Chou, *Review of super-resolution fluorescence microscopy for biology.* Applied spectroscopy, 2011. **65**(9): p. 967-80.
39. Heintzmann, R. and G. Ficz, *Breaking the resolution limit in light microscopy.* Methods in cell biology, 2013. **114**: p. 525-44.
40. Schermelleh, L., R. Heintzmann, and H. Leonhardt, *A guide to super-resolution fluorescence microscopy.* The Journal of Cell Biology, 2010. **190**(2): p. 165-75.
41. Hell, S.W., *Toward fluorescence nanoscopy.* Nature Biotechnology, 2003. **21**(11): p. 1347-55.
42. Hell, S.W. and M. Kroug, *Ground-state-depletion fluorescence microscopy: a concept for breaking the diffraction resolution limit.* Appl. Phys. B, 1995. **60**: p. 495-497.
43. Folling, J., M. Bossi, H. Bock, R. Medda, C.A. Wurm, B. Hein, S. Jakobs, C. Eggeling, and S.W. Hell, *Fluorescence nanoscopy by ground-state depletion and single-molecule return.* Nature Methods, 2008. **5**(11): p. 943-5.
44. Testa, I., N.T. Urban, S. Jakobs, C. Eggeling, K.I. Willig, and S.W. Hell, *Nanoscopy of living brain slices with low light levels.* Neuron, 2012. **75**(6): p. 992-1000.
45. Chmyrov, A., J. Keller, T. Grotjohann, M. Ratz, E. d'Este, S. Jakobs, C. Eggeling, and S.W. Hell, *Nanoscopy with more than 100,000 'doughnuts'.* Nature Methods, 2013. **10**(8): p. 737-40.
46. Heintzmann, R., T.M. Jovin, and C. Cremer, *Saturated patterned excitation microscopy--a concept for optical resolution improvement.* Journal of the Optical Society of America. A, Optics, image science, and vision, 2002. **19**(8): p. 1599-609.
47. Tonnesen, J. and U.V. Nagerl, *Superresolution imaging for neuroscience.* Experimental Neurology, 2013. **242**: p. 33-40.
48. Westphal, V., S.O. Rizzoli, M.A. Lauterbach, D. Kamin, R. Jahn, and S.W. Hell, *Video-rate far-field optical nanoscopy dissects synaptic vesicle movement.* Science, 2008. **320**(5873): p. 246-9.
49. Kittel, R.J., C. Wichmann, T.M. Rasse, W. Fouquet, M. Schmidt, A. Schmid, D.A. Wagh, C. Pawlu, R.R. Kellner, K.I. Willig, S.W. Hell, E. Buchner, M. Heckmann, and S.J. Sigrist, *Bruchpilot promotes active zone assembly, Ca2+ channel clustering, and vesicle release.* Science, 2006. **312**(5776): p. 1051-4.
50. Fouquet, W., D. Owald, C. Wichmann, S. Mertel, H. Depner, M. Dyba, S. Hallermann, R.J. Kittel, S. Eimer, and S.J. Sigrist, *Maturation of active zone assembly by Drosophila Bruchpilot.* The Journal of Cell Biology, 2009. **186**(1): p. 129-45.

51. Nagerl, U.V. and T. Bonhoeffer, *Imaging living synapses at the nanoscale by STED microscopy.* The Journal of neuroscience : the official journal of the Society for Neuroscience, 2010. **30**(28): p. 9341-6.
52. Nagerl, U.V., K.I. Willig, B. Hein, S.W. Hell, and T. Bonhoeffer, *Live-cell imaging of dendritic spines by STED microscopy.* Proceedings of the National Academy of Sciences of the United States of America, 2008. **105**(48): p. 18982-7.
53. Urban, N.T., K.I. Willig, S.W. Hell, and U.V. Nagerl, *STED nanoscopy of actin dynamics in synapses deep inside living brain slices.* Biophysical Journal, 2011. **101**(5): p. 1277-84.
54. Berning, S., K.I. Willig, H. Steffens, P. Dibaj, and S.W. Hell, *Nanoscopy in a living mouse brain.* Science, 2012. **335**(6068): p. 551.
55. Xu, K., G. Zhong, and X. Zhuang, *Actin, spectrin, and associated proteins form a periodic cytoskeletal structure in axons.* Science, 2013. **339**(6118): p. 452-6.
56. Dani, A., B. Huang, J. Bergan, C. Dulac, and X. Zhuang, *Superresolution Imaging of Chemical Synapses in the Brain.* Neuron, 2010. **68**(5): p. 843-856.
57. Moneron, G. and S.W. Hell, *Two-photon excitation STED microscopy* Optics Express, 2009. **17**(17): p. 14567-14573.
58. Ding, J.B., K.A. Takahashi, and B.L. Sabatini, *Supraresolution Imaging in Brain Slices using Stimulated-Emission Depletion Two-Photon Laser Scanning Microscopy.* Neuron, 2009. **63**: p. 429-437.
59. Li, Q., S.S.H. Wu, and K.C. Chou, *Subdiffraction-Limit Two-Photon Fluorescence Microscopy for GFP-Tagged Cell Imaging.* Biophysical Journal, 2009. **97**(12): p. 3224-3228.
60. Ding, J.B., K.T. Takasaki, and B.L. Sabatini, *Supraresolution imaging in brain slices using stimulated-emission depletion two-photon laser scanning microscopy.* Neuron, 2009. **63**(4): p. 429-37.
61. Takasaki, K.T., J.B. Ding, and B.L. Sabatini, *Live-cell superresolution imaging by pulsed STED two-photon excitation microscopy.* Biophys J, 2013. **104**(4): p. 770-7.
62. Bianchini, P., B. Harke, S. Galiani, G. Vicidomini, and A. Diaspro, *Single-wavelength two-photon excitation-stimulated emission depletion (SW2PE-STED) superresolution imaging.* Proceedings of the National Academy of Sciences of the United States of America, 2012. **109**(17): p. 6390-3.
63. Li, Q., Y. Wang, D. Chen, and S.S. Wu, *2PE-STED Microscopy with a Single Ti: Sapphire Laser for Reduced Illumination.* PLoS ONE, 2014. **9**(2): p. e88464.
64. Garcia-Parajo, M.F., G.M. Segers-Nolten, J.A. Veerman, J. Greve, and N.F. van Hulst, *Real-time light-driven dynamics of the fluorescence emission in single green fluorescent protein molecules.* Proceedings of the National Academy of Sciences of the United States of America, 2000. **97**(13): p. 7237-42.
65. Kaech, S. and G. Banker, *Culturing hippocampal neurons.* Nature Protocols, 2006. **1**(5): p. 2406-15.
66. Riedl, J., A.H. Crevenna, K. Kessenbrock, J.H. Yu, D. Neukirchen, M. Bista, F. Bradke, D. Jenne, T.A. Holak, Z. Werb, M. Sixt, and R. Wedlich-Soldner,

Lifeact: a versatile marker to visualize F-actin. Nature Methods, 2008. **5**(7): p. 605-7.

67. Rothbauer, U., K. Zolghadr, S. Tillib, D. Nowak, L. Schermelleh, A. Gahl, N. Backmann, K. Conrath, S. Muyldermans, M.C. Cardoso, and H. Leonhardt, *Targeting and tracing antigens in live cells with fluorescent nanobodies.* Nature Methods, 2006. **3**(11): p. 887-9.
68. Ries, J., C. Kaplan, E. Platonova, H. Eghlidi, and H. Ewers, *A simple, versatile method for GFP-based super-resolution microscopy via nanobodies.* Nature Methods, 2012. **9**(6): p. 582-4.
69. Opazo, F., M. Levy, M. Byrom, C. Schafer, C. Geisler, T.W. Groemer, A.D. Ellington, and S.O. Rizzoli, *Aptamers as potential tools for super-resolution microscopy.* Nature Methods, 2012. **9**(10): p. 938-9.
70. Gahwiler, B.H., *Organotypic monolayer cultures of nervous tissue.* Journal of Neuroscience Methods, 1981. **4**(4): p. 329-42.
71. Amaral, D. and P. Lavenex, *Hippocampal Neuroanatomy*, in *The Hippocampus Book*, P. Andersen, et al., Editors. 2007, Oxford University Press: Oxford, New York.
72. Fiala, J.C. and K.M. Harris, *Dendrite Structure*, in *Dendrites*, G. Stuart, M. Spruston, and M. Häusser, Editors. 1999, Oxford University Press.
73. Herzog, E., F. Nadrigny, K. Silm, C. Biesemann, I. Helling, T. Bersot, H. Steffens, R. Schwartzmann, U.V. Nagerl, S. El Mestikawy, J. Rhee, F. Kirchhoff, and N. Brose, *In vivo imaging of intersynaptic vesicle exchange using VGLUT1 Venus knock-in mice.* The Journal of neuroscience : the official journal of the Society for Neuroscience, 2011. **31**(43): p. 15544-59.
74. Shaner, N.C., P.A. Steinbach, and R.Y. Tsien, *A guide to choosing fluorescent proteins.* Nature Methods, 2005. **2**(12): p. 905-909.
75. Holtmaat, A., T. Bonhoeffer, D.K. Chow, J. Chuckowree, V. De Paola, S.B. Hofer, M. Hubener, T. Keck, G. Knott, W.C. Lee, R. Mostany, T.D. Mrsic-Flogel, E. Nedivi, C. Portera-Cailliau, K. Svoboda, J.T. Trachtenberg, and L. Wilbrecht, *Long-term, high-resolution imaging in the mouse neocortex through a chronic cranial window.* Nature Protocols, 2009. **4**(8): p. 1128-44.
76. Kramer, K., S.A. van Acker, H.P. Voss, J.A. Grimbergen, W.J. van der Vijgh, and A. Bast, *Use of telemetry to record electrocardiogram and heart rate in freely moving mice.* Journal of pharmacological and toxicological methods, 1993. **30**(4): p. 209-15.
77. Wildanger, D., R. Medda, L. Kastrup, and S.W. Hell, *A compact STED microscope providing 3D nanoscale resolution.* Journal of Microscopy, 2009. **236**(1): p. 35-43.
78. Klar, T.A., S. Jakobs, M. Dyba, A. Egner, and S.W. Hell, *Fluorescence microscopy with diffraction resolution barrier broken by stimulated emission.* Proceedings of the National Academy of Sciences of the United States of America, 2000. **97**(15): p. 8206-10.
79. Lenz, M.O., H.G. Sinclair, A. Savell, J.H. Clegg, A.C. Brown, D.M. Davis, C. Dunsby, M.A. Neil, and P.M. French, *3-D stimulated emission depletion microscopy with programmable aberration correction.* Journal of Biophotonics, 2013.

80. Gould, T.J., D. Burke, J. Bewersdorf, and M.J. Booth, *Adaptive optics enables 3D STED microscopy in aberrating specimens.* Optics Express, 2012. **20**(19): p. 20998-1009.
81. Matsuzaki, M., N. Honkura, G. Ellis-Davies, and H. Kasai, *Structural basis of long-term potentiation in single dendritic spines.* Nature, 2004. **429**(6993): p. 758-761.
82. Becker, N., C. Wierenga, R. Fonseca, T. Bonhoeffer, and U. Nagerl, *LTD Induction Causes Morphological Changes of Presynaptic Boutons and Reduces Their Contacts with Spines.* Neuron, 2008. **60**(4): p. 590-597.
83. Richards, D.A., J.M. Mateos, S. Hugel, V. de Paola, P. Caroni, B.H. Gahwiler, and R.A. McKinney, *Glutamate induces the rapid formation of spine head protrusions in hippocampal slice cultures.* Proceedings of the National Academy of Sciences of the United States of America, 2005. **102**(17): p. 6166-71.
84. Wierenga, C.J., N. Becker, and T. Bonhoeffer, *GABAergic synapses are formed without the involvement of dendritic protrusions.* Nature Neuroscience, 2008. **11**(9): p. 1044-1052.
85. Goslin, K., H. Asmussen, and G. Banker, *Rat hippocampal neurons in low-density culture*, in *Culturing nerve cells*, G. Banker and K. Goslin, Editors. 1991, MIT: Cambridge. p. 339-370.
86. Mondin, M., V. Labrousse, E. Hosy, M. Heine, B. Tessier, F. Levet, C. Poujol, C. Blanchet, D. Choquet, and O. Thoumine, *Neurexin-neuroligin adhesions capture surface-diffusing AMPA receptors through PSD-95 scaffolds.* The Journal of neuroscience : the official journal of the Society for Neuroscience, 2011. **31**(38): p. 13500-15.
87. Bethge, P., R. Chereau, E. Avignone, G. Marsicano, and U.V. Nagerl, *Two-photon excitation STED microscopy in two colors in acute brain slices.* Biophysical Journal, 2013. **104**(4): p. 778-85.
88. Zipfel, W.R., R.M. Williams, and W.W. Webb, *Nonlinear magic: multiphoton microscopy in the biosciences.* Nature Biotechnology, 2003. **21**(11): p. 1369-77.

5 Abbreviations

STED	Stimulated emission depletion
PSF	Point-spread function
near-IR	Near infra red (light)
CA1	Cornu ammonis 1
CA3	Cornu ammonis 3
GFP	Green fluorescent protein
FITC	Fluorescein isothiocyanate
BFP	Back focal plane
AU	Airy unit
NA	Numerical Aperture
FWHM	Full width at half maximum
PALM	Photoactivated localization microscopy
STORM	Stochastic optical reconstruction microscopy
SIM	Structured illumination microscopy
RESOLFT	Reversible saturable optical fluorescence transitions
W	Watt
GSD	Ground state depletion
Thy1	Thymocyte differentiation antigen 1
LTP	Long-term potentiation
Ti:sapphire	Titanium-sapphire
FRAP	Fluorescence recovery after photobleaching
OPO	Optical parametric oscillator
CW	Continuous-wave
APD	Avalanche photo diode
PMT	Photo multiplier tube
2PE	Two photon excitation
vGLUT1	Vesicular glutamate transporter 1
CX3CR1	CX3C chemokine reporter / fractalkine receptor
FLIM	Fluorescence-lifetime imaging microscopy

6 Appendix

6.1 Tissue preparation

Following are short protocols for the preparation of the experimental preparations used in this thesis.

6.1.1 Dissociated hippocampal cell culture

Dissociated hippocampal neurons from embryonic day 18 rat embryos of either sex were plated on 18 mm polylysine-coated glass coverslips at a density of 10′000 cells/cm^2 in MEM containing 10% horse serum (Invitrogen) for 3 h, then cultured in Neurobasal medium supplemented with B27 on a layer of glial cells[85]. Neurons were transfected at 4–7 DIV using Effectene (Qiagen) and processed 2–5 d later[86].

6.1.2 Organotypic hippocampal slice culture

Organotypic hippocampal slices were prepared from 5- to 7-day-old transgenic Thy1-YFP mice and cultured for 2–4 weeks using the Gähwiler technique as roller-drum cultures[70]. In brief, the isolated hippocampi were cut to 350 µm thickness on a tissue chopper before being embedded in plasma/thrombin clots on heat treated and poly-L-lysine coated glass coverslips. The dissection was carried out in cooled Grey’s Balanced Salt Solution containing in g/L: 0.220 CaCl2*2 H2O; 0.740 KCl; 0.030 KH_2PO_4; 0.210 $MgCl_2$*6 H_2O; 0.070 $MgSO_4$*7 H_2O; 8 NaCl; 0.227 $NaHCO_3$; 0.120 Na_2HPO_4; 1.100 D(+)-Glucose*H_2O, supplemented with 1ml of kynurenic acid (Sigma-Aldrich, 18,90% w/v diluted in 0.1M NaOH solution) and with a glucose solution (Sigma-Aldrich) to a final concentration of 11g/l: pH 7.2.

Roller-drum culturing was done at 35°C with a rotation speed of 10/h in a medium containing 50% of Basal Medium Eagle (BME, Gibco); 25% of Hanks’ Balanced Salt solution (HBSS, Gibco); 25% of heat inactivated horse serum (Gibco) supplemented with Glutamine to a final concentration of 1mM and Glucose to a final concentration of 11g/l.

6.1.3 Acute brain slices

Thy1-YFP mice aged 21–40 days old were killed by cervical dislocation, and their brains were quickly removed and placed in ice-cold sucrose-based artificial cerebrospinal fluid (ACSF) containing (in mM) 210 sucrose, 10 glucose, 2 KCl, 26 $NaHCO_3$, 1.25 NaH_2PO_4, 0.1 $CaCl_2$, and 6 MgCl (pH 7.4, osmolarity ~320 mOsm/L), which was bubbled with carbogen (95% O_2/5% CO_2). Sagittal 350-mm-thick slices were cut using a vibratome (VT1200, Leica, Mannheim, Germany) and transferred to a heated (32º C) holding chamber with NaCl-based ACSF bubbled with carbogen, which consisted of (in mM) 124 NaCl, 3 KCl, 26 $NaHCO_3$, 1.25 NaH_2PO_4, 10 glucose, 2 $CaCl_2$, 1 MgCl, and 0.6 Trolox (pH 7.4, osmolarity ~305 mOsm/L) for 1 h. These slices were subsequently maintained at room temperature for a maximum of 4 h. For the imaging experiments, the slices were transferred to a submerged recording chamber, where they were continuously perfused (2.1 mL/min) with ACSF at room temperature[87].

6.1.4 *In vivo* preparation

The craniotomy on 35 day old Thy1-YFP mice was performed following [75]. The animal was continuously kept under 2% isoflurane anesthesia during the surgery and imaging. The skin above the head was removed with sterilized scissors and a 3-4 mm round craniotomy was performed under cortex buffer (125 mM NaCl, 5 mM KCl, 10 mM glucose, 10mM HEPES, 2 mM $CaCl_2$, 2mM $MgSO_4$ in distilled H_2O, pH 7.4). The skull was carefully scratched and a thin layer of cyanoacrylate was applied. A #1 coverslip (1.15 mm thickness, 3 mm diameter) was carefully lowered on the brain surface and attached to the skull with cyanoacrylate. A titanium bar for the attachment to a head holder (Luigs&Neumann, Germany) was attached to the skull using dental acrylic.

6.2 Point-spread function (PSF)

The properties of a monochromatic image of a point source by a well-corrected circular lens are given by the three-dimensional diffraction limited light distribution near the focal plane that is derived from the Huygens-Fresnel principle to be

$$h_A(v,u) = 2C \int_0^1 \exp\left(-\frac{iu}{2}\rho^2\right) J_0(\rho v)\rho d\rho \tag{6.1}$$

with

$v = \frac{2\pi}{\lambda} r \sin(\alpha)$ and $u = \frac{2\pi}{\lambda} z\, sin^2\left(\frac{\alpha}{2}\right)$ as the optical coordinates in the image plane, with $r = \sqrt{x^2 + y^2}$, λ = wavelength of light, NA = sin(α). J_0denotes the zero-order Bessel function, ρ the normalised radius of the aperture, C a constant that gives the electromagnetic field a geometric focus ($u = v = 0$)[12].

This relationship is known as the amplitude PSF and represents the strength of the electromagnetic field in the image plane.

The intensity distribution of a single point object near the focal plane is the squared modulus of the electric field amplitude as a response to a point source of an optical system.

It defines the intensity point-spread-function (PSF) as

$$h(v,u) = |h_A(v,u)|^2 = h_A(v,u)h_A^*(v,u) \tag{6.2}$$

with

$v = \frac{2\pi}{\lambda} r \sin(\alpha)$ and $u = \frac{2\pi}{\lambda} z\, sin^2\left(\frac{\alpha}{2}\right)$ as the optical coordinates in the image plane, $r = \sqrt{x^2 + y^2}$, λ = wavelength of light, α = half angle of the angular aperture.

The extent of the intensity PSF is often described by the term Airy disc which is defined as including approx. 84% of total photon flux within the illumination intensity PSF and described by

$$h(v, 0) = h_0 \left[\frac{2J_1(v)}{v}\right]^2 \tag{6.3}$$

for the radial extend and

$$h(0, u) = h_0 \left[\frac{\sin\,(u/4)}{u/4}\right]^2 \tag{6.4}$$

for the axial extend with J_1 as the Bessel function of the first kind of order one[12].

6.3 Spatial resolution

The term Airy disc is helpful in describing the resolution or the minimal resolvable distance between two closely spaced objects by means of the Rayleigh criterion that states:

Two closely spaced objects can be resolved if the minimum of first object PSF coincides with the maximum of the second object's PSF

In optical microscopy, spatial resolution is often described as the minimal distance between two objects by the FWHM of the intensity PSF for a given optical system with

$$\Delta r = 0.51 \frac{\lambda}{NA} \tag{6.5}$$

for the lateral and

$$\Delta z = 1.77 \frac{n\lambda}{NA^2} \tag{6.6}$$

for the axial resolution with n = the refractive index of the immersion medium and the numerical aperture NA= n sin(α).

6.3.1 Spatial resolution in a confocal microscope

In confocal microscopy the effective PSF is a product of the probability of a given point to emit a photon times the probability that this photon passes the pinhole and can be detected. Hence the effective point-spread-function $h_{confocal}$ of a confocal microscope can be expressed by

$$h_{confocal}(v,u) = h_{ill}(v,u) * h_{det}\left(\frac{v}{\beta},\frac{u}{\beta}\right) \approx h_{ill}^2(v,u) \tag{6.7}$$

with $h_{ill}(v,u)$ as the illumination PSF, $h_{det}\left(\frac{v}{\beta},\frac{u}{\beta}\right)$ the detection PSF and $\beta = \frac{\lambda_{fl}}{\lambda_{ill}}$ which is approximated to 1 (λ_{fl} = wavelength of emission light and λ_{fl} = wavelength of excitation light).

The quadratic dependency of the confocal PSF leads to a smaller PSF and a resolution enhancement by the factor 1.4. The FWHM resolution of an idealised confocal pinhole is then described for the lateral dimension by

$$\Delta r = 0.37\frac{\lambda}{NA} \tag{6.8}$$

and the axial dimension

$$\Delta \mathrm{z} = 1.28\frac{\lambda}{NA^2} \tag{6.9}$$

6.3.2 Spatial resolution in a two-photon microscope

In two-photon microscopy, the fluorescence intensity depends on the square of the excitation intensity and therefore the square of the illumination PSF becomes relevant

$$h_{two-photon}(v,u) = h_{ill}^2\left(\frac{v}{2},\frac{u}{2}\right) \tag{6.10}$$

with $\frac{v}{2}$ and $\frac{u}{2}$ correcting for the approx. double wavelength used in two-photon excitation microscopy.

This results in a modified formula to describe the radial resolution limit

$$\begin{aligned} \Delta r &= \frac{0.320\sqrt{2ln2}\,\lambda}{\sqrt{2}\,NA}, NA \leq 0.7 \\ \Delta r &= \frac{0.325\sqrt{2ln2}\,\lambda}{\sqrt{2}\,NA^{0.91}}, NA > 0.7 \end{aligned} \tag{6.11}$$

and axial resolution limit

$$\Delta r = \frac{0.325\lambda}{\sqrt{2}}\left(\frac{1}{n-\sqrt{n^2-NA^2}}\right) \tag{6.12}$$

where λ = wavelength, $n =$ refractive index of medium, NA = numerical aperture of the objective lens[12, 88].